REPORT DOCUMENTATION PAGE

Form Approved
OMB No. 0704-0188

1. REPORT DATE (DD-MM-YYYY)	2. REPORT TYPE	3. DATES COVERED (From - To)
8/4/03	Final Report	5/1/99-3/30/03

4. TITLE AND SUBTITLE

Dynamics of Cavitation on Rotating Propulsors

5a. CONTRACT NUMBER

5b. GRANT NUMBER
N00014-99-1-0307

5c. PROGRAM ELEMENT NUMBER

6. AUTHOR(S)
Steven L. Ceccio

5d. PROJECT NUMBER

5e. TASK NUMBER

5f. WORK UNIT NUMBER

7. PERFORMING ORGANIZATION NAME(S) AND ADDRESS(ES)

Mechanical Engineering
2011 Automotive Lab
University of Michigan
Ann Arbor, MI
48109-2121

8. PERFORMING ORGANIZATION REPORT NUMBER

9. SPONSORING / MONITORING AGENCY NAME(S) AND ADDRESS(ES)
Office of Naval Research
800 N. Quincy St., BCT 1
Arlington, VA 22217-5660

10. SPONSOR/MONITOR'S ACRONYM(S)
ONR

11. SPONSOR/MONITOR'S REPORT NUMBER(S)

12. DISTRIBUTION / AVAILABILITY STATEMENT

distribution unlimited

DISTRIBUTION STATEMENT A
Approved for Public Release
Distribution Unlimited

13. SUPPLEMENTARY NOTES

14. ABSTRACT

In this program we are investigated the dynamics of cavitation as it occurs on or near rotating propulsors. While there are many different forms of cavitation on propulsors, we are concentrating our effort on understanding the flow processes resulting in "limited event rate" cavitation occurring in the vortical flows in the tip region of ducted propulsors. We completed the construction of a new recirculating water channel. We are examining the process of nuclie capture, cavitation, and noise production of vortex cavitation. We have been conducting experiments both at our laboratory at the University of Michigan and at the Naval Surface Warfare Center, Carderock Division. Our primary effort has been examining the tip leakage flow of a large ducted rotor in the 36inch water tunnel at NSWC-CD. This experiment is conducted in cooperation with Dr. Jessup of NSWC.

15. SUBJECT TERMS

16. SECURITY CLASSIFICATION OF: unclassified			17. LIMITATION OF ABSTRACT	18. NUMBER OF PAGES	19a. NAME OF RESPONSIBLE PERSON
a. REPORT	b. ABSTRACT	c. THIS PAGE			S. L. Ceccio
					19b. TELEPHONE NUMBER *(include area code)* 734-936-0433

Standard Form 298 (Rev. 8-98)
Prescribed by ANSI Std. Z39.18

A Final Report:

Dynamics of Cavitation on Rotating Propulsors

Steven L. Ceccio
Department of Mechanical Engineering
University of Michigan, Ann Arbor, MI 48109-2133
phone: (734) 936-0433 fax: (734) 764-4256 email: ceccio@umich.edu

Grant Number: N00014-99-1-0307

ABSTRACT

In this program we are investigated the dynamics of cavitation as it occurs on or near rotating propulsors. While there are many different forms of cavitation on propulsors, we are concentrating our effort on understanding the flow processes resulting in "limited event rate" cavitation occurring in the vortical flows in the tip region of ducted propulsors. We completed the construction of a new recirculating water channel. We are examining the process of nuclie capture, cavitation, and noise production of vortex cavitation. We have been conducting experiments both at our laboratory at the University of Michigan and at the Naval Surface Warfare Center, Carderock Division. Our primary effort has been examining the tip leakage flow of a large ducted rotor in the 36inch water tunnel at NSWC-CD. This experiment is conducted in cooperation with Dr. Jessup of NSWC.

RESULTS

The main findings of this project are contained in the four attached manuscripts. Three other manuscirpts are in preparation.

ATTACHMENTS

Goweis, G. and S. L. Ceccio, "Instantaneous and Time Averaged Flow Fields of Multiple Vortices in the Tip Region of a Ducted Propulsor," *J. Fluid Mech.* **(in preparation)** (2003)

Goweis, G., D. Fry, S. D. Jessup, and S. L. Ceccio, "Development of a Tip-Leakage Vortex with Varying Reynolds Number," *J. Fluid Eng.* **(in preparation)** (2003)

Goweis, G., D. Fry, S. D. Jessup, and S. L. Ceccio, "Comparison of the Tip and Leakage Vortex from a Ducted and Un-Ducted Rotor," *J. Fluid Eng.* **(in preparation)** (2003)

Oweis, G., I. E. van der Hout, C. Iyer, G. Tryggvason, and S. L. Ceccio, "Capture and Inception of Bubbles Near Line Vortices," *Physics of Fluids*, **(under review for publication)** (2003)

Oweis, G., J. Choi, S. L. Ceccio, "Measurement of the Dynamics and Acoustic Transients Generated by Laser Induced Cavitation Bubbles," *J. of the Acoustic Society of America*, **(accepted for publication)** (2003)

Iyer, C. and S. L. Ceccio, "The influence of Developed Cavitation on the Flow of a Turbulent Shear Layer," *Physics of Fluids*, Vol. 14, No. 10, pp 3414 - 3431 (2002)

Ceccio, S. L., C. Judge, D. Fry, C. Chesnakas, S. Jessup, G. F. Oweis, "Cavitation Inception in Tip Leakage Vortices," *Proc. CAV2001*, Pasadena, CA, (2001)

The influence of developed cavitation on the flow of a turbulent shear layer

Claudia O. Iyer and Steven L. Ceccio
Department of Mechanical Engineering, University of Michigan, Ann Arbor, Michigan 49109-2121

(Received 28 January 2002; accepted 27 June 2002; published 28 August 2002)

Developed cavitation in a shear layer was studied experimentally in order to determine the effect that the growth and collapse of cavitation have on the dynamics of shear flows. Planar particle imaging velocimetry (PIV) was used to measure the velocity field, the vorticity, strain rates, and Reynolds stresses of the flow downstream of the cavitating and noncavitating shear layer; the flow pressures and void fraction were also measured. The flow downstream of a cavitating shear flow was compared to the noncavitating shear flow. For cavitating shear layers with void fractions of up to 1.5%, the growth rate of the shear layer and the mean flow downstream of the shear layer were modified by the growth and collapse of cavitation bubbles. The cross-stream velocity fluctuations and the Reynolds stresses measured downstream of the cavitating shear layer were reduced compared to the entirely noncavitating flow. This result is inconsistent with a scaling of the shear stress within the shear flow based on the mean flow. The decrease in the cross-stream fluctuations and Reynolds stresses suggests that the cavitation within the cores of strong streamwise vortices has decreased the coupling between the streamwise and cross-stream velocity fluctuations. © *2002 American Institute of Physics.* [DOI: 10.1063/1.1501541]

I. INTRODUCTION

Cavitation has been observed to occur in turbulent shear flows when the local liquid pressure drops below the liquid vapor pressure and vapor bubbles form in the low-pressure cores of fluid vortices. Such "vortex cavitation" can occur within strong liquid jets, within regions of flow separation, and in the turbulent wakes of bluff objects (see Brennen[1] for a recent review). Cavitating shear flows occur in the closure region of attached cavities and are associated with the formation of strong vortices downstream of a partial cavity (Laberteaux and Ceccio,[2] Laberteaux *et al.*,[3] Gopalan and Katz,[4] and Laberteaux and Ceccio[5,6]). The cavitating turbulent shear flow associated with attached cavitation plays an important role in the formation of cloud cavitation and in the processes that cause cavitation erosion (Kawanami *et al.*,[7] Callenaere *et al.*[8]).

Developed cavitating shear layers are complex multiphase flows. The continuous flow field is turbulent and characterized by relatively high Reynolds numbers (typically greater than 10 000 based on integral length scales). The disperse (vapor) phase has a complex, nonspherical geometry and is often not in thermodynamic equilibrium with the continuous phase. Volume fractions can be relatively large (often much greater than 1%). The vapor phase is often preferentially concentrated within the low-pressure cores of the strongest vortices, the sites of cavitation inception, and the presence of vapor in the shear layer can alter both the large-scale and small-scale flow processes. But, to date, experimental observations have not revealed which interactions between the vapor and the liquid flow fields constitute the dominant mechanisms responsible for overall flow modification. This question will be addressed by the present study through the experimental examination of a cavitating shear layer.

Large-scale spanwise vortical structures are an important feature of turbulent shear layers (Brown and Roshko,[9] Winant and Brown[10]). Counter-rotating pairs of streamwise vortices can occur between the larger spanwise vortices (Bernal *et al.*,[11] Lasheras *et al.*,[12] and Lasheras and Choi[13]). With a reduction in free-stream pressure, the cores of the spanwise and streamwise vortices can fill with gas and vapor. Cavitating shear flows have been investigated by a number of researchers, and a review of the older literature is provided by Arndt.[14] Katz[15] studied the cavitation inception within shear layers formed on axisymmetric bodies whose boundary layers underwent a laminar separation and subsequent turbulent reattachment. Katz and O'Hern[16] and O'Hern[17] examined cavitation inception and development in a plane shear layer for Reynolds numbers up to 2×10^6. Katz and O'Hern[16] showed that cavitation inception occurs first within the streamwise vortices of the shear layer. The streamwise vortices are stretched between the spanwise vortices, resulting in a reduction in the vortex diameter and core pressure. A further reduction in the overall flow pressure will then lead to cavitation in the streamwise vortices. In a continuation of this study, O'Hern[17] did not observe significant changes in the shear layer growth rate of a vortex roll-up process as the cavitation developed.

Cavitation forming in the turbulent wake of bluff objects has been investigated by many researchers, including Kermeen and Parkin,[18] Young and Holl,[19] Arndt,[20] Arndt and George,[21] and Belahadji *et al.*[22] Shedding of wake vortices can be altered by the development of cavitation in the vortex cores, and developed wake cavitation will typically increase the shedding frequency of the Karman vortices observed in the wake by up to 25%. Belahadji *et al.*[22] employed high-speed photography to investigate cavitation in the rotational structures of the turbulent wake behind a two-dimensional obstacle. They concluded that incipient cavitation in the

wake acted as a passive agent of flow visualization, but developed cavitation actively altered the dynamics of the turbulent wake.

The presence of cavitation within a turbulent shear flow can potentially alter the dynamics of the flow through both local and global mechanisms. The presence of developed cavitation can lead to overall flow changes through decreases in mean flow density, increases in the overall flow volume, or modification of the mean pressure field. Cavitation can also modify the vortical flow locally. Belahadji *et al.*[22] have suggested that cavitation in the cores of vortices will affect the process of vortex stretching by the decoupling of the vortex strain and rotation rate. Gopalan and Katz[4] demonstrated that significant flow–vapor interactions exist in the cavitating shear flow downstream of a partial cavity. And, Laberteaux and Ceccio[5,6] showed how the growth and collapse of disperse cavitation bubbles led to the production of small-scale turbulence in the wake of partial cavities.

In the present study, we investigated how the development and collapse of cavitation within a plane shear layer alters the dynamics of the shear layer. The shear flow was examined from cavitation inception to full development. Planar particle imaging velocimetry (PIV) was used to examine the flow downstream of the cavitating shear layer, and flow pressures and void fractions were measured. We will show that the growth and collapse of cavitation within the shear layer altered the mean and fluctuating velocities of the flow downstream of the cavitating region.

II. EXPERIMENTAL SETUP AND METHODS

A. Flow facility and test model

Experiments were conducted in the Model Large Cavitation Channel (MLCC) in the Cavitation and Multiphase Flow Laboratory described by George and Ceccio.[23] The MLCC is a recirculating water tunnel with a capacity of approximately 2.8 m^3. Most of the lower leg has circular cross sections upstream and downstream of the impeller; the upper leg, including the contraction, test section, and diffuser, has a square cross section. The flat top of the MLCC allows low pressures in the test section without subvapor pressures and cavitation occurring in adjacent parts of the tunnel. As a result, the 6:1 contraction upstream of the test section is nonsymmetric, and internal flow straighteners are angled upward to make the velocity profile uniform within the test section. The rectangular test section has interior dimensions of 21.6 $\times 21.6 \times 118$ cm, with a flow area of 446 cm^2 due to fillets in the corners. The four sides of the test section hold removable windows made of acrylic or aluminum. Before experiments, water is deaerated by circulation between the MLCC and a 2.27 m^3 deaeration tank; the oxygen content of the water can be reduced to about 40% saturation in three hours. Flow in the MLCC is generated by an impeller in the bottom leg. The MLCC can operate at constant test section velocities of up to 15 m/s. The overall air content of the MLCC can be modified using a deaeration system. However, the nuclei content of the flow within the tunnel cannot be directly controlled. The oxygen content of the water was measured with a dissolved oxygen meter (Orion Model 810). Values of the oxygen content are reported at atmospheric pressure.

To create a shear layer, a sharp-edged plate spanning the full 21.6 cm width of the test section was placed vertically into the flow in a manner similar to that of Katz and O'Hern[16] and O'Hern.[17] The plate was 90 mm from the entrance to the test section, and mounted on a false floor to allow the boundary layer flow on the test section walls to pass beneath through a gap 12.5 mm tall. The false floor consists of a 58 mm tall and 710 mm long wedge. The height of the plate, h, is equal to 31 mm. The top of the plate consists of a chamfered edge with a broken apex. The shear layer produced at the apex of the wedge flows into a diffuser with an angle of 9°. The pressure recovery in this diffuser is sufficient to cause desinence of the cavitating shear layer. A schematic diagram of the plate within the test section is shown in Fig. 1.

A differential pressure transducer (Mid-West Instrument Model 120) was used to measure the pressure between the entrance to the contraction and the wall above the apex of the plate. This pressure difference was used to determine the free-stream velocity, U_∞, after calibration with a single-component laser Doppler anemometry (LDA) system (Dantec DISA Type 55L90a) with the probe volume located midway between the apex of the plate and the top window of the test section. This tap was also used to measure the static pressure at the inlet of the test section with a Test Gauge by Ashcroft. Pressure was measured at this tap to determine the cavitation number, $\sigma=(P_l-P_v)/\frac{1}{2}\rho U_\infty^2$. The temperature of the flow was measured with a thermocouple and used to determine the liquid density, ρ, liquid kinematic viscosity, ν, and vapor pressure, P_v. A second pressure tap was located downstream of the plate, and the differential pressure between the upstream and downstream taps was measured with a differential pressure transducer (Omega PX26-005DV). Moreover, dynamic pressure transducers were placed near these two pressure taps (PCB Piezotronics Model 102A05) to measure the fluctuating pressure component. Spectra of the fluctuating pressures were measured with a Stanford Research Systems SR770 FFT network analyzer. A bandwidth of 1 Hz was used over a range of 1024 kHz, and 1000 individual spectra were averaged. Side view and top view images of the shear layer were recorded with a Nikon 35 mm camera using flash photography and with a high-speed digital imaging system (Kodak EktaPro HS Motion Analyzer Model 4540mx).

B. Void fraction measurement

The average void fraction of the shear layer was measured using two different techniques. Light scattering was used to detect the passage of bubbles in a small probe volume. The LDA system was used to detect the passage of bubbles within its probe volume. As bubbles passed through the probe volume (with dimensions of 1.0 mm for the probe volume length and 0.12 mm for the beam waist diameter), a strong flash of laser light was detected by the photomultiplier tube. This signal saturated the tube, creating an electrical

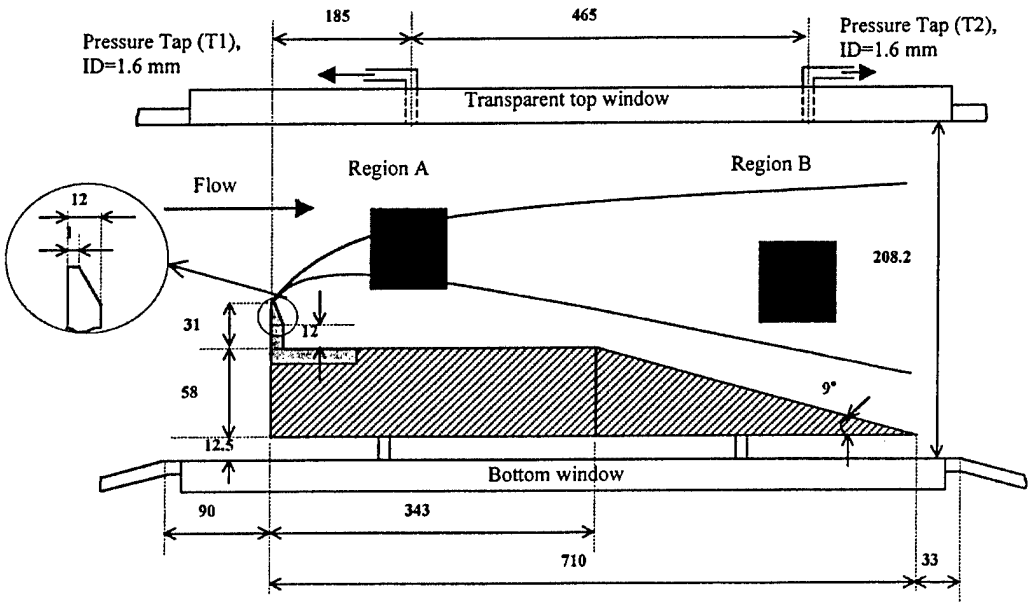

FIG. 1. Schematic diagram of the sharp-edged plate installed in the MLCO test section. The dimensions are in mm.

pulse with time width much longer that the actual bubble passage. Thus, the light scattering system could detect the passage of a bubble, but not the residence time within the probe volume. Instead, the residence time was measured with a high-speed digital imaging system (Kodak EktaPro HS Motion Analyzer Model 4540mx). The duration of the light pulses that resulted from the passage of bubbles within the probe volume was recorded and was typically 250 μs. Bubble event rates were measured for time intervals of 60 s and then averaged. With the bubble event rate, f_B, and residence time, t_B, the local void fraction, α, can be calculated as

$$\alpha = f_B t_B .$$

The above equation provides a rough estimate of the void fraction. Second, a laser light sheet was used to illuminate a plane of the cavitating shear layer and digital images of the shear layer were recorded. (More details of the light sheet and camera setup are provided below.) The image of the shear layer contained images of the bubbles within the shear layer with some in focus and others out of focus. The image was thresholded and scaled to produce a binarized image that recovered only the in-focus bubbles. A pixel value of "0" was liquid and a value of "1" was gas. Five-hundred images were averaged to yield the overall average pixel value for the image and this was considered the void fraction. The void fraction values computed this way were consistent with the values obtained from light scattering, although the uncertainty of both measurements is relatively large.

C. Particle imaging velocimetry

The noncavitating and cavitating flows were examined with planar particle imaging velocimetry (PIV). PIV measurements were performed in region A, upstream, for noncavitating flows and in region B, downstream, for both noncavitating and cavitating flows, as shown in Fig. 1. Two frequency-doubled Quanta-Ray Spectra-Physics GCR-130 Nd:YAG lasers were used to create a double-pulsed light sheet in the test section. These lasers emit light pulses with 10 ns duration at 532 nm wavelength with a repetitive rate of 30 Hz and 30 mJ/pulse. The light sheet was approximately 1 mm thick and 100 mm wide and was placed parallel to the mean flow direction. Single-frame, double-pulsed images were recorded at 90° to the light sheet plane with a Silicon Mountain Design SMD 4M4 digital camera that frames at 4 Hz and has a resolution of 2048×2048 pixels. The camera was mounted on an $X-Y$ traverse for easy translation along the test section. The light sheet making optics was also placed on a traverse that could be translated from region A to region B of the test section. The camera has an image-shifting feature whereby the image created by the first laser pulse is shifted vertically by a finite number of lines before the second image is recorded. This image shifting permits the introduction of a velocity bias in the double-pulsed image, thus eliminating ambiguity in the sign of the velocity. Images were acquired at 3 Hz, and the time between light pulses, Δt, was measured within an accuracy of 50 ns with an HP 54620 A logic analyzer. The time separation, Δt, determines the maximum and minimum velocities that can be measured. The time separation, Δt, used in region A, upstream, was 21.6 μs and in region B, downstream, 53.6 μs. PIV measurements were made with a field of view of 5.5×5.5 cm. Spatial calibration of the image was performed by registering the image on a fixed object after a known motion on the traverse, and the traverse motion was measured to an accuracy of 50 μm over a span of 55 000 μm. The flow was seeded with fluorescent latex particles 80 μm in diameter with a specific

gravity between 0.9 and 1.1. A filter was placed on the camera to block the green light of the lasers ($\lambda = 532$ nm) and only allow the fluorescent return of the particles ($\lambda = 580$ nm). In this way, images of vapor bubbles could be excluded from the PIV image.

The double-pulsed images were interrogated using autocorrelation with the software package VISIFLOW by AEA Technology. An interrogation region of 128×128 pixels was used with an overlap of 50%, resulting in a resolution of 1.7 mm with a field of view of 5.5×5.5 cm. There were typically 8–15 particle pairs within each interrogation region. With a time separation of 21.6 μs in region A and 53.6 μs in region B, a velocity of 5 m/s would correspond to a particle displacement of four pixels and ten pixels, respectively. The number of bad vectors in each image was typically 5% or less and interpolation was used to replace them. Each processed image yielded 32×32 instantaneous local velocity vectors in the plane of interest. The associated vorticity and strain-rate distributions were computed from the two-dimensional velocity field using centered finite differences:

$$\omega_z(i,j) = \frac{\partial v}{\partial x} - \frac{\partial u}{\partial y} = \frac{v(i+1,j) - v(i-1,j)}{2\Delta x} - \frac{u(i,j+1) - u(i,j-1)}{2\Delta y},$$

$$S_{xy}(i,j) = \frac{\partial v}{\partial x} + \frac{\partial u}{\partial y} = \frac{v(i+1,j) - v(i-1,j)}{2\Delta x} + \frac{u(i,j+1) - u(i,j-1)}{2\Delta y},$$

where u and v are the horizontal and vertical velocity components, i and j are the horizontal and vertical indices, and Δx and Δy are the horizontal and vertical grid spacing. Up to 1000 images were averaged to find the average and fluctuating component of these quantities.

D. Experimental uncertainty

The estimated uncertainty in the measured mean pressures and velocity is ±2%. The temperature was accurate to within ±0.2 °C. This leads to an uncertainty in the cavitation number of ±6%. The uncertainty of the PIV velocity is related to the uncertainty in the spatial and temporal measurements for the system. The uncertainty of the spatial measurement is related to the magnification of the image area, the particle displacement, and the size of the PIV autocorrelation interrogation area. For a speed of 5 m/s, the average particle displacement was 10 pixels. The displacements are known to subpixel resolution of ±0.2 pixels. This yields an uncertainty in the displacements of around ±2%. The uncertainty is larger for the cross-stream velocities since they are on the order of 0.5 m/s or less. The uncertainty in the spatial calibration is 0.1% (based on the traverse accuracy of 50 μm over a span of 55 000 μm). The time separation between successive laser light pulses is measured very accurately within 50 ns, which makes the uncertainty of the measured time interval less than ±0.1%. Thus, we estimate that the uncertainty in the measured velocity is approximately 1%–2% for the streamwise (u component) of the velocities, and 10%–20% for the cross-stream (v component) of the velocities. The uncertainty in the measurement of the average void fraction is about 25% of the reported average value.

The smallest resolvable velocity fluctuation, $\Delta u/U_{fs}$, is ±0.02 based on the minimum resolution of the PIV processing of ±0.2 pixels. Here $N = 1000$ images were averaged to achieve a higher level of precision, and the resulting uncertainty is approximated by $\Delta u/U_{fs} \cdot (1/\sqrt{N}) \sim \pm 0.001$. Differences of less than ±0.002 are within the uncertainty of the measurement. If the integral length scale of the flow is $\sim 2\delta = L_I$, the spatial resolution of the PIV images is $\sim 0.03 \cdot L_I$. This compares with an estimate of the Taylor length scale $L_\lambda \approx L_I \sqrt{(\nu/k^{1/2} L_I)} \approx L_I \sqrt{(\nu/0.2 \cdot U_{fs} \cdot 2\delta)} \approx 0.003 \cdot L_I$, where the turbulent kinetic energy, k, is approximated with $k^{1/2} \approx \sqrt{\overline{u'u'}} \approx 0.2 U_{fs}$. Consequently, these measurements do not spatially resolve the smallest turbulent length scales of the flow and the implication for not resolving all scales is that we will likely underestimate the local turbulent intensity.

The smallest resolvable Reynolds stress, $\Delta u \Delta u / U_{fs}^2$, is ±0.04, based on the minimum resolution of the PIV processing of ±0.2 pixels. The $N = 1000$ images were averaged to achieve a higher level of precision, and the resulting uncertainty is approximated by $\Delta(\Delta u \Delta u/U_{fs}^2) = \Delta u \Delta u/U_{fs}^2 \cdot (1/\sqrt{N}) \sim \pm 0.001$. Differences of less than ±0.002 are within the uncertainty of the measurement.

III. RESULTS AND DISCUSSION

A. The non-cavitating flow of the shear layer in region A

PIV was used to examine the noncavitating flow of the shear layer near the origin of the shear layer in region A. The free-stream velocity measured above the shear layer was $U_\infty = 9$ m/s, giving a Reynolds number based on the plate height, $h = 31$ mm, of $\mathrm{Re} = 2hU_\infty/\nu = 5.56 \times 10^5$ (O'Hern[17] reported data for $\mathrm{Re} = 2hU_\infty/\nu = 9.57 \times 10^5$). The free-stream pressure was sufficiently high to prevent cavitation ($\sigma = 2.3$). Figure 2 shows (a) the mean in-plane velocity, $\bar{u} - U_{\mathrm{Mean,A}}$, (b) the mean vorticity, ω_z, (c) the mean strain rate, S_{xy}, and (d) the mean Reynolds stress, $-\overline{u'v'}/U_{\mathrm{Mean,A}}^2$. Here $U_{\mathrm{Mean,A}} = 3.86$ m/s and is the average velocity determined by averaging all 32×32 vectors of the mean velocity field of region A. 700 individual vector realizations were averaged. As expected, high levels of vorticity, strain rate, and Reynolds stresses are observed in the middle of the shear layer.

The data from Fig. 2 was used to determine the nondimensional mean-axial velocity profiles $(\bar{u} - U_{\mathrm{Bottom,A}})/(U_{\mathrm{Top,A}} - U_{\mathrm{Bottom,A}})$. These are plotted against the nondimensional vertical distance, y/δ, at three cross-sections of region A: $x/h = 5.53$, $x/h = 5.96$, and $x/h = 6.4$, in Fig. 3. The y axis was first shifted by δ such that the origin of the y axis corresponds to the point where $(\bar{u} - U_{\mathrm{Bottom,A}})/(U_{\mathrm{Top,A}} - U_{\mathrm{Bottom,A}}) = 0.5$ and then the y values were nondimensionalized by $\delta = 26.2$ mm, corresponding to approximately half of the local shear layer thickness. Here $U_{\mathrm{Top,A}} = 7.0$ m/s and $U_{\mathrm{Bottom,A}} = 0.5$ m/s are the average ve-

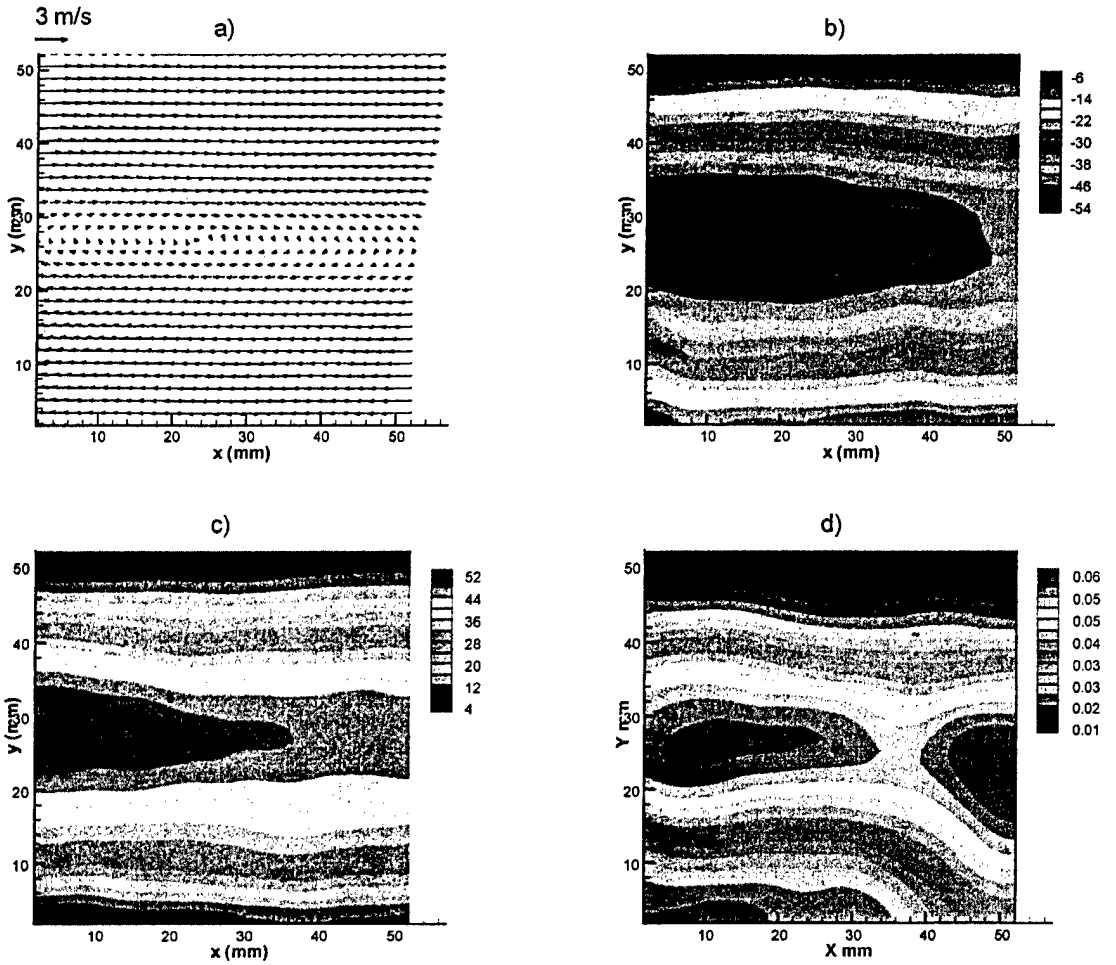

FIG. 2. Average noncavitating flow in region A presenting (a) mean velocity, $\bar{u}-U_{\text{Mean,A}}$ (m/s), (b) vorticity, ω_z (1/s), (c) strain rate, S_{xy} (1/s); and (d) the Reynolds stresses $-u'v'/U^2_{\text{Mean,A}}$. The flow is from left to right. Here 1000 individual images were averaged.

locities of the high- and low-speed free-stream flows measured at the top and bottom boundary of the PIV images in region A. Three averaged velocity profiles across the shear layer are shown for three distances measured from the vertex of the plate. In this figure the downstream distance x was nondimensionalized by the plate height h. (This length scale was similarly chosen by O'Hern[17] and it is on the order of the vortex spacing in region A.)

The velocity profiles indicate that the shear layer is close to achieving a similarity condition. Using the average shear layer thickness, 2δ, in region A and the velocity difference, $(U_{\text{Top,A}}-U_{\text{Bottom,A}})$, the average Reynolds number is calculated as $\text{Re}_\delta=2\delta(U_{\text{Top,A}}-U_{\text{Bottom,A}})/\nu=3.35\times10^5$. Wygnanski and Fiedler[24] used hot-wire probes to examine a two-dimensional, incompressible shear layer of air forming downstream of a backward facing step. This flow geometry is analogous to that of the present study. Their flow had a local Reynolds number on the order of $\text{Re}_\delta\approx10^4$ after the shear layer achieved similarity. Figure 4 presents the distribution of the nondimensional velocity fluctuation profiles, $\overline{u'u'}/(U_{\text{Top,A}}-U_{\text{Bottom,A}})^2$ and $\overline{v'v'}/(U_{\text{Top,A}}-U_{\text{Bottom,A}})^2$, at

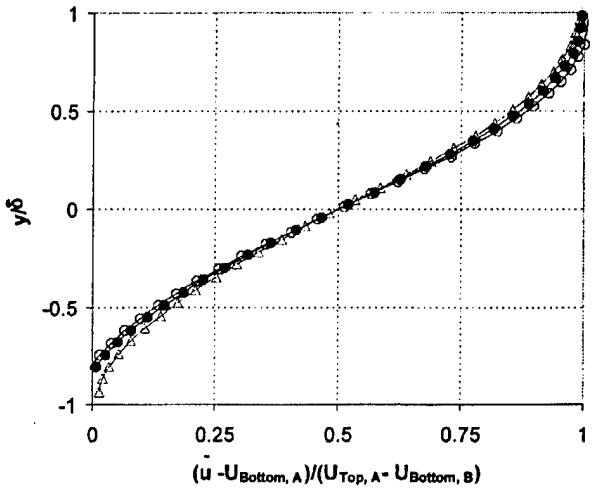

FIG. 3. Mean axial velocity profiles in region A derived from the data in Fig. 2. Here $(\bar{u}-U_{\text{Bottom,A}})/(U_{\text{Top,A}}-U_{\text{Bottom,A}})$ is plotted across the shear layer for three downstream positions, x/h. The symbols ○, ●, and △ indicate $x/h=5.53$, 5.97, and 6.40, respectively.

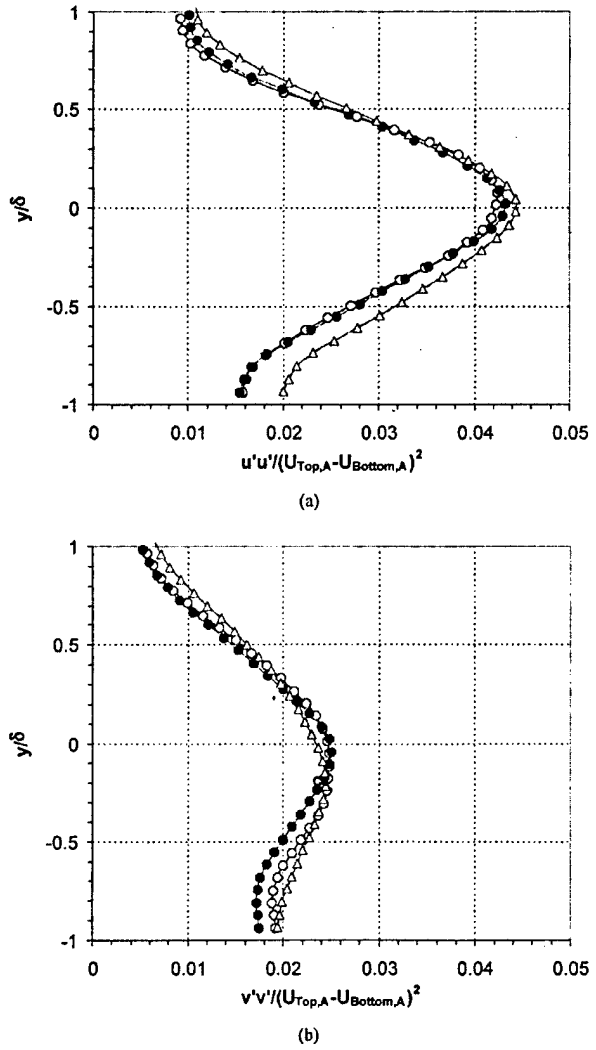

FIG. 4. Velocity fluctuation profiles (a) $u'u'/(U_{\mathrm{Top,A}}-U_{\mathrm{Bottom,A}})^2$ and (b) $v'v'/(U_{\mathrm{Top,A}}-U_{\mathrm{Bottom,A}})^2$ in region A derived from the data in Fig. 2 for three downstream positions, x/h. The symbols ○, ●, and △ indicate x/h =5.53, 5.97, and 6.40, respectively.

three cross-sections. The maximum velocity fluctuation amplitude is 4.4%, which qualitatively agrees with a maximum value of 18% reported by Wygnanski and Fiedler[24] for the nondimensional root-mean-square velocity fluctuations. It should also be noted that the turbulence level does not tend to zero outside of the shear layer, and this suggests that the free-stream turbulence levels are relatively high (on the order of 2% of the free-stream), even with the flow conditioning and 6:1 contraction. This indicates that the shear layer in region A is reasonably two-dimensional and has becomes self-similar before reaching the diffuser in region B.

B. Examination of the cavitating shear layer

While maintaining the free-stream velocity at 10 m/s, the free-stream pressure was reduced, and cavitation was observed in region A. The inception cavitation number was approximately $\sigma=0.65$ for a dissolved oxygen content of 3 ppm and $\sigma=0.57$ for a dissolved oxygen content of 1.7 ppm. O'Hern[17] reported a cavitation inception index of $\sigma=1.1$ for a dissolved air content of 3.6 ppm and $\sigma=1.4$ for an air content of 7–12 ppm. The extent of cavitation developed at 3 ppm is similar to that reported by O'Hern.[17] (See Yu and Ceccio[25] for a discussion of the relationship between dissolved oxygen content and dissolved air content.) In both the present experiment and those of O'Hern,[17] the free-stream nuclei content was not controlled or measured. These differences in inception indices between the work of O'Hern[17] and the present work can be partially explained by the free-stream nuclei content. However, our method used to call inception in the present work is "visual calls" and it leads to a delayed cavitation call compared to the method of O'Hern.

Figure 5 presents side-view photographs, taken under stroboscopic light, of different levels of cavitation in the shear layer (with an oxygen content of 2.7 ppm). Figure 5(a) shows that inception cavitation occurs in the form of long, thin streamwise cavities oriented at about 45° to the mean flow, visualizing the low-pressure cores of streamwise vortices of the shear layer that form between adjacent spanwise vortices. At lower cavitation numbers, the entire turbulent structure of the shear layer can be visualized by cavitation within both streamwise and spanwise vortices, as seen in Figs. 5(b)–5(e). At the lowest cavitation number [Fig. 5(e)] the recirculating region beneath the cavity becomes filled with a bubbly mixture. These observations of incipient and developed shear layer cavitation are consistent with those of Katz and O'Hern[16] and O'Hern.[17] Figure 6 presents a time series of the developed cavitating shear layer formed behind the sharp-edged plate ($\sigma=0.52$, $U_\infty=9.0$ m/s, and c_O =2.7 ppm, where c_O is the oxygen content). Such high-speed video images were analyzed to determine the shear layer growth rate and vortex spacing.

O'Hern[17] observed that the growth of the cavitating shear layer was little changed from that of the noncavitating shear layer, and a similar result was found in the present study. Figure 7 shows a plot of the dimensionless shear layer thickness, δ^*/h, versus the dimensionless downstream distance, x/h. The growth rate, δ^*/h, had a slope of 0.25, and this compares well to the value of 0.23 found by O'Hern[17] for a cavitating shear layer, and to the value of 0.22 found by Wygnanski and Fiedler.[24] The spacing of the spanwise cavitating vortices increases with an increasing downstream distance. Figure 8 shows the average spanwise vortex spacing, l, as a function of the downstream distance, x, for two cavitation numbers. The spanwise vortex spacing constant is defined as l/x, and this was found to be 0.47 for $\sigma=0.45$ and 0.51 for $\sigma=0.57$. A value of 0.50 was found by O'Hern[17] for a shear flow with developed cavitation. Bernal *et al.*,[11] Hernan and Jimenez,[26] and Jimenez[27] found values of 0.56 for noncavitating turbulent plane shear layer with Re_δ $>10^4$. The values found for the cavitating shear layer are equivalent to those measured for the noncavitating layer, within the uncertainty of the measurement.

Figure 9 presents the average spacing and diameter of the spanwise vortices, and the length of the streamwise vortices as a function of cavitation number. These quantities were averaged over the entire field of view (about 10 cm in

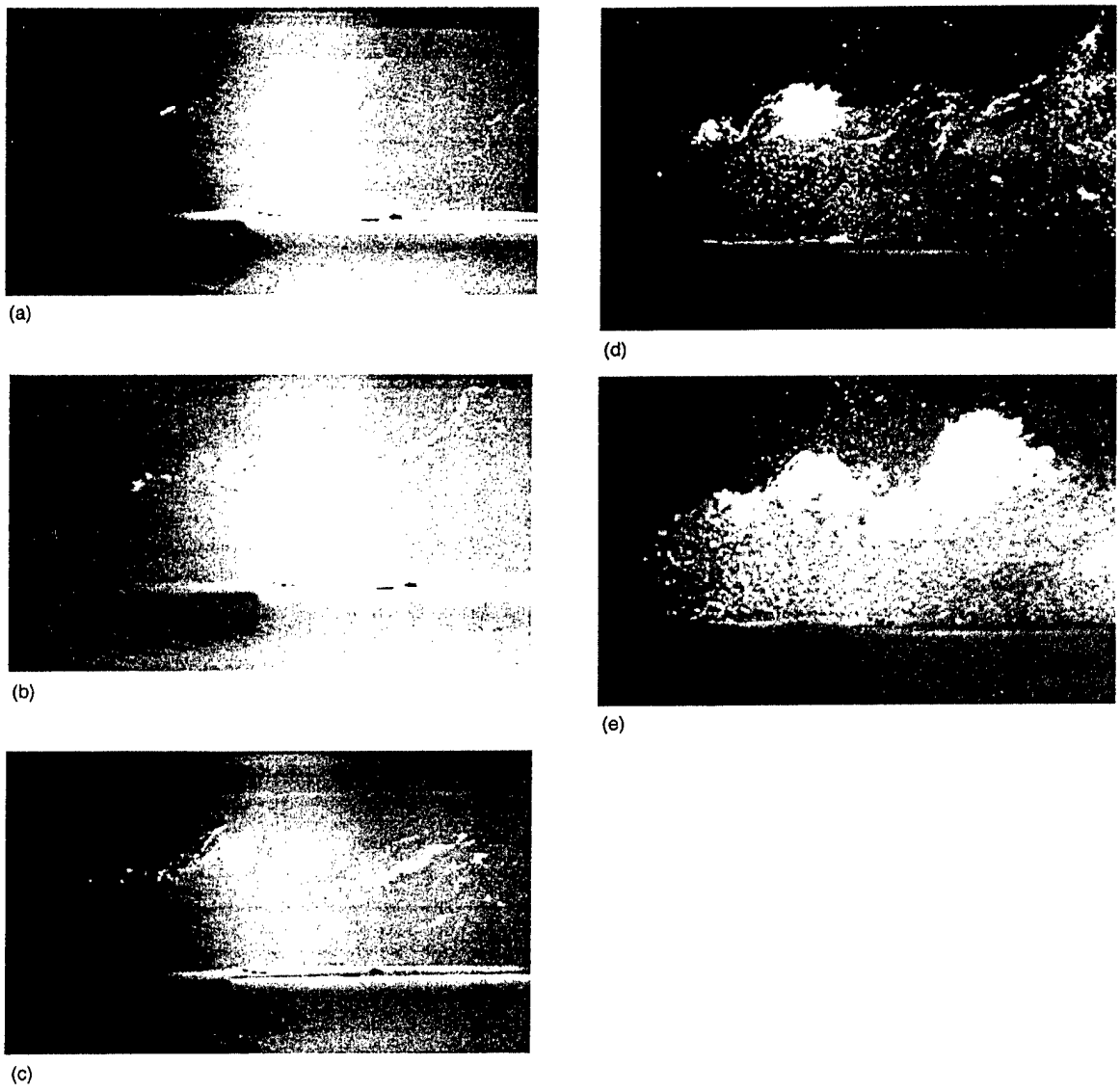

FIG. 5. (a) Photograph of incipient cavitation for $\sigma=0.65$, $U_\infty=9.0$ m/s. (b) Photograph of incipient cavitation for $\sigma=0.57$, $U_\infty=9.0$ m/s. (c) Photograph of incipient cavitation for $\sigma=0.50$, $U_\infty=9.0$ m/s. (d) Photograph of incipient cavitation for $\sigma=0.41$, $U_\infty=9.0$ m/s. (e) Photograph of incipient cavitation for $\sigma=0.33$, $U_\infty=9.0$ m/s.

the streamwise direction and 15 cm in the spanwise direction) for the growing shear layer. The lengths in this figure were nondimensionalized by 2δ, where $\delta=26.2$ mm is half the shear layer thickness measured in region A. Only small changes are seen with a variation in the cavitation number. In Fig. 9, the average spacing of the spanwise vortices, 1, decreases with decreasing cavitation number as the number of vortices observed increases. In the same figure, a slight increase in the diameter of the spanwise vortices and the length of the streamwise vortices is observed, although these changes are well within the range of uncertainty. Note that there is a slight increase in the diameter and the length of these vortices for $\sigma=0.50$ as the cavitation number is lowered to 0.45.

If a noncavitating streamwise vortex is simply modeled as a Rankine vortex with core radius, a, the pressure within the core, P_c, is given by

$$P_\infty - P_C = \rho\left(\frac{\Gamma_S}{2\pi a}\right)^2,$$

where Γ_s is the strength of the vortex. At the point of cavitation inception in the vortex, the core pressure reaches the vapor pressure, $P_c=P_v$, assuming that the water is sufficiently populated with cavitatable nuclei (i.e., the water is "weak"). In this case, the vortex strength would be given by

$$\Gamma_S = 2\pi a U_\infty \sqrt{\sigma_i},$$

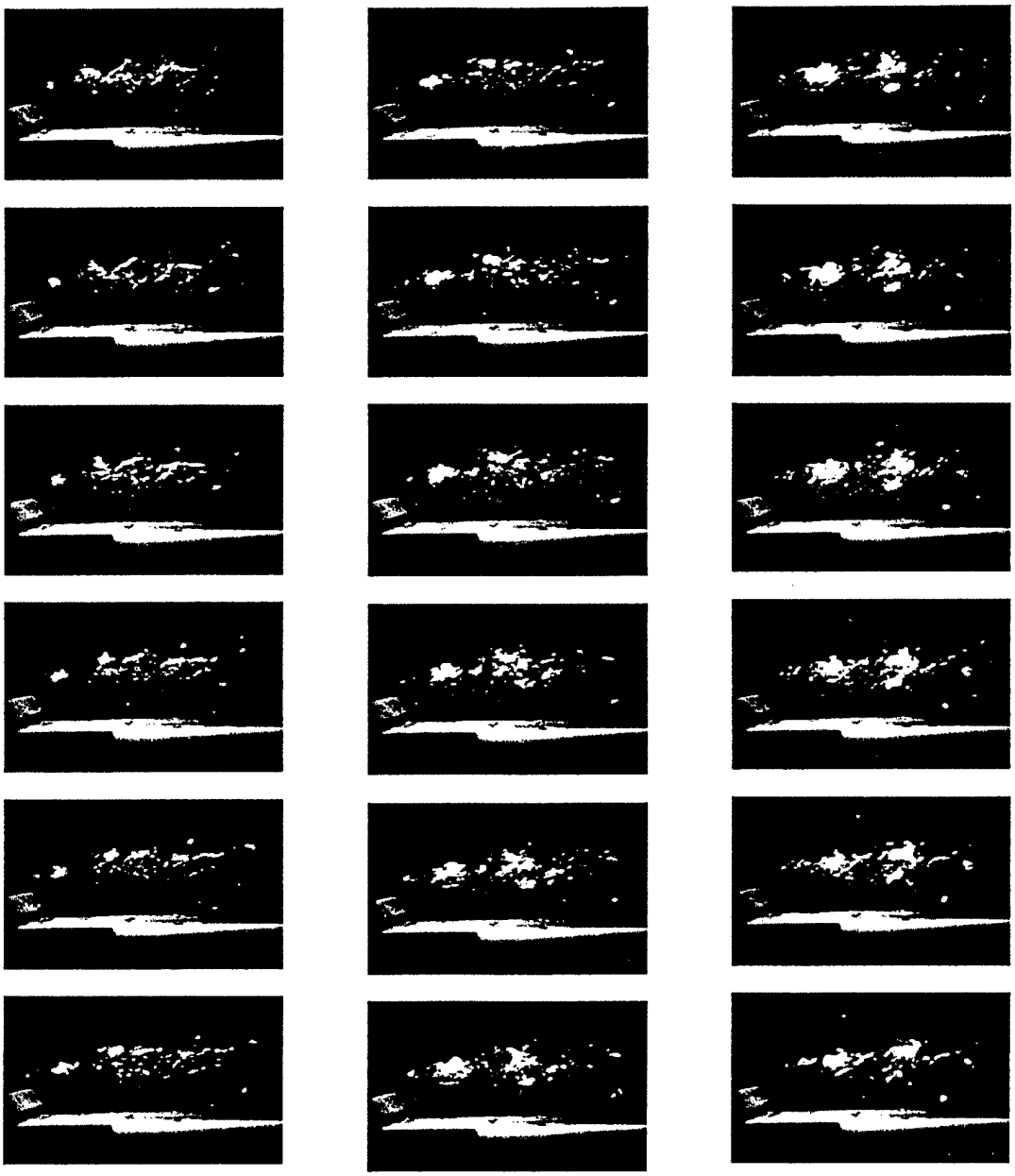

FIG. 6. A time series of images of shear-flow cavitation for $\sigma=0.52$ and $U_\infty=9.0$ m/s. The flow is from left to right in each image. The series progresses from top to bottom and left to right. The time interval between each frame is 1.11 ms.

where σ_i is the cavitation number at inception. O'Hern[17] examined cinemagraphic records of streamwise vortex cavitation inception, and the size of the initial bubble in the vortex at inception was determined. It was then assumed that the bubble radius was approximately equal to the original core radius, and this measurement was used to determine Γ_S. The spanwise vortex strength, Γ_P, was estimated to be $\Gamma_P \approx \Delta U \cdot l$, where ΔU is the velocity difference across the layer and l is the local spanwise vortex spacing. O'Hern concluded that the ratio Γ_P/Γ_s was between 0.01 and 0.10 near the inception point of the streamwise vortices. This ratio was smaller than the value suggested by Jimenez *et al.*[28] (who reported $\Gamma_S/\Gamma_P \approx 0.6 \pm 0.8$ for a single-phase plane shear layer). Recent investigations into developed tip–vortex cavitation suggest that incipient vortex cavitation does not fill the original viscous core (Briançon-Marjollet and Merle[29]). As the vortex fills with vapor, the diameter of the vapor tube may be several times the size of the original core size, but this is principally due to diffusion of gas into the vortex core. Arndt and Keller[30] analyzed a Rankine vortex before and after the advent of developed cavitation. If angular momentum is conserved, the vapor core diameter will be $a/\sqrt{2}$. Examining the data at low air content ($\sigma_i=1.1$), we will assume that the core size of noncavitating the vortex

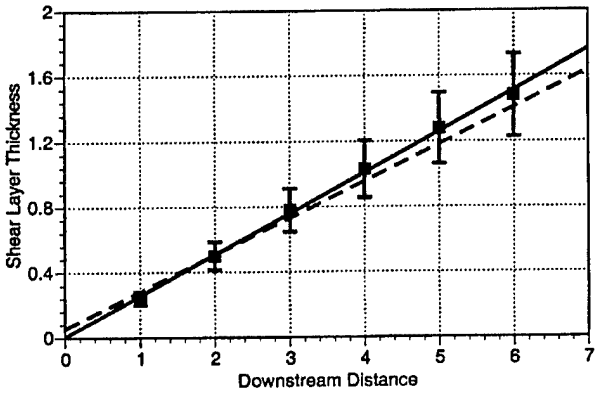

FIG. 7. Growth of shear layer thickness, δ^*/h, as a function of downstream distance, x/h, for $\sigma=0.50$ and $U_\infty=9$ m/s (b). The solid line is the linear regression $\delta^*/h=0.25(x/h+0.02)$. These data are compared to that of O'Hern (1990), who found a relationship of $\delta^*/h=0.225(x/h+0.05)$ shown with the dashed line.

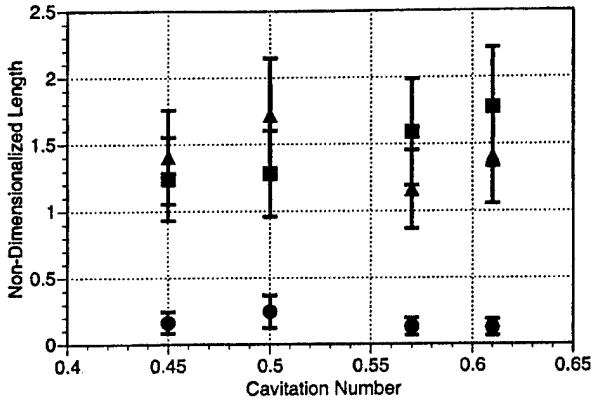

FIG. 9. The average spacing (■), length (▲), and diameter (●) of the streamwise vortices as a function of cavitation number observed in region A. The lengths are nondimensionalized by 2δ.

was 1.4 times the vapor core diameter. The average value of Γ_s is then about 0.14 m^2/s, and Γ_P is approximately 0.7 m^2/s. Then, $\Gamma_S/\Gamma_P \approx 0.2$. As we have assumed a larger initial core radius, this value is somewhat larger than that of O'Hern. However, it is still smaller than that expected from examination of noncavitating mixing layers.

C. Void fraction of the cavitating shear layer

Figure 10 presents a plot of the local void fraction measured in region A. Values reported are for two oxygen contents, and for both the light scattering and digital-imaging measurement methods. As the cavitation number decreases, the void fraction of the shear layer increases, as expected. However, the light scattering method consistently measured lower void fractions compared to the digital images measurement at higher cavitation numbers. The calculation of the void fraction from the bubble event rate employed a fixed bubble residence time, of 250 μs, in the measurement volume. However, the actual residence time will likely increase with decreasing cavitation number as the average length of the streamwise bubbles increases. Moreover, the light scattering method measured the void fraction at a small volume within the center of the shear layer, while the light-sheet method averaged the void fraction over the entire region A. Yet, even with these differences, the void fractions are qualitatively similar with maximum average void fractions of 1%–1.5% at the lowest cavitation numbers. Note that the average void fraction is reduced as the dissolved oxygen content is reduced for a given cavitation number. A reduction in dissolved gas content is often associated with a reduction in the free gas content (i.e., the number of small free-stream bubbles), and with a reduction in the number of free-stream nuclei the extent of the cavitation will be reduced.

D. Mean pressure

The mean pressure difference measured between the surface taps T1 and T2, shown in Fig. 1, was 5.8±0.2 kPa. This

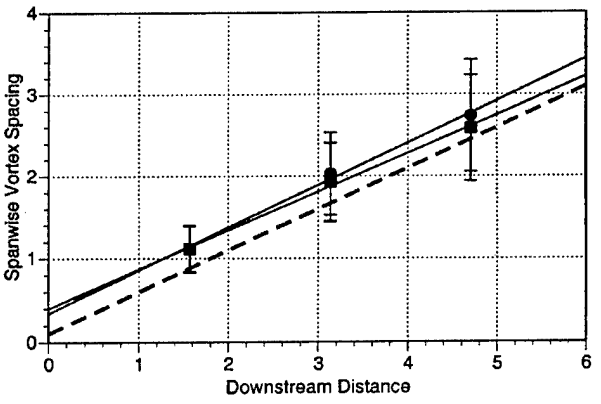

FIG. 8. Growth of the spanwise vortex spacing, l/h, as a function of downstream distance, x/h, for $\sigma=0.57$ (●) and $\sigma=0.45$ (■) and $U_\infty=9$ m/s. The solid lines are linear regressions $l/h=0.51(x/h+0.66)$ and $l/h=0.47(x/h+0.85)$. These data are compared to that of O'Hern (1990), who found a relationship of $l/h=0.50(x/h+0.20)$ shown with a dashed line.

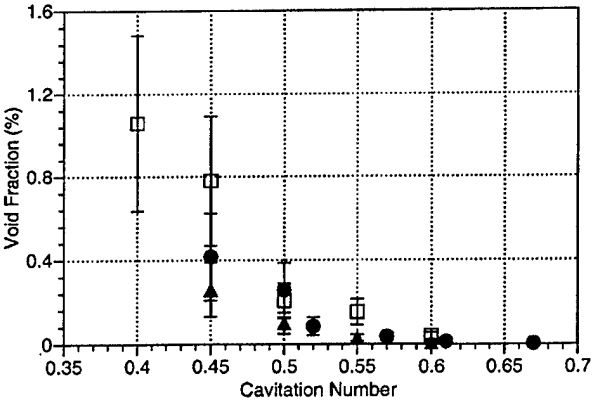

FIG. 10. Void fraction in region A as a function of cavitation number. Two methods were used to determine the void fraction. Light scattering was employed at a single point in the center of region A for 3 ppm (●) and 1 ppm (▲) dissolved oxygen content. The void fraction was inferred from planar digital images in region A for 3 ppm dissolved oxygen content (□).

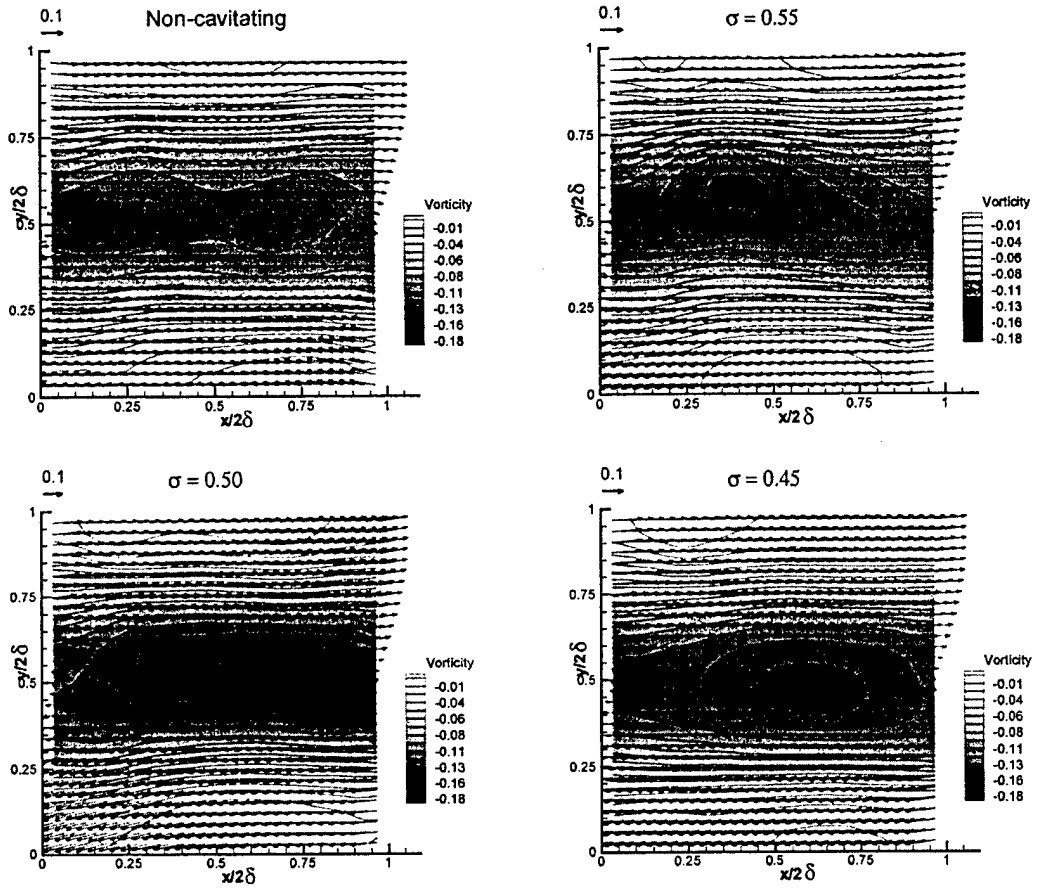

FIG. 11. Average flow in region B presenting the nondimensional mean velocity, $(\bar{u}-U_{\text{Mean,B}})/U_{\text{Mean,B}}$ and the nondimensional vorticity contours, $\omega_z 2\delta/U_{\text{Mean,B}}$. The flow is from left to right. Here 1000 individual images were averaged.

value was not influenced by the extent of cavitation within the test section over the range of cavitation numbers examined. This suggests that the mean flow through the test section was not substantially altered by the development of cavitation in the shear layer.

E. Comparison between the noncavitating and the cavitating mean flows in region B

As the shear layer enters the diffuser, the vapor pockets in the cavitating vortices collapse leaving only small gas bubbles in the flow. PIV measurements were performed in this downstream region of the cavitating flow using only seed particles as flow tracers. Measurements were performed downstream of the noncavitating shear flow ($\sigma=2.3$) and downstream of three cavitating shear flows, with cavitation numbers of 0.55, 0.50, and 0.45. As shown in Fig. 10, the void fraction of the cavitating shear layer increases sharply between $\sigma=0.50$ and 0.45. By conducting measurements in region B, the lasting influences of the growth and collapse of the cavitating vortices on the turbulent shear flow are examined.

One-thousand PIV images were acquired in region B and averaged for each cavitation number. Figure 11 presents the dimensionless mean in-plane velocity, $(\bar{u}-U_{\text{Mean,B}})/U_{\text{Mean,B}}$, superimposed on the dimensionless out-of-plane vorticity, $\omega_z 2\delta/U_{\text{Mean,B}}$. The mean velocity, $U_{\text{Mean,B}}$, has been subtracted from each image. Some differences are observed in the mean velocity field of the noncavitating flow compared to the cavitating shear flow. Figure 12 shows the average velocity profiles, $\bar{u}/U_{\text{fs}}$, for three cross-stream sections of region B: $x/h=20.54$ in the left half (upstream) of the image, $x/h=20.96$ in the middle of the image, and $x/h=21.38$ in the right half (downstream) of the image. The average free-stream velocity, U_{fs}, was computed by averaging 25 velocity vectors from the top left corner of the average velocity field.

At the lowest cavitation numbers, the gradient of the velocity across region B is increased. The influence of the cavitation decreases with increasing downstream distance. Convection of the flow across region B represents nearly one turnover of the spanwise eddies. Figures 13 and 14 present profiles of the average vorticity and strain rate for the same three cross-streams. These data are normalized by 2δ, the average shear layer thickness of region A, since for the purpose of scaling 2δ is the order of magnitude of the shear layer thickness in region B. With $\Delta u/U_{\text{fs}}\sim\pm 0.02$, and with

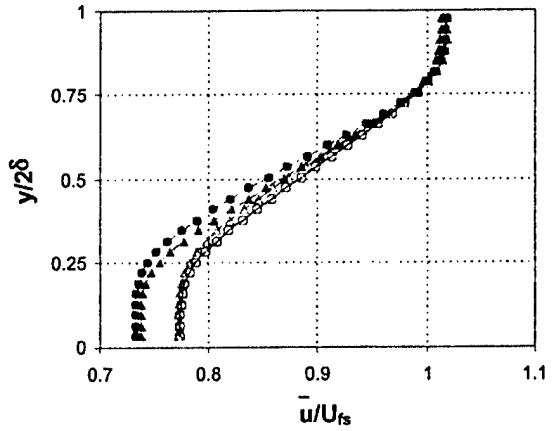

(a)

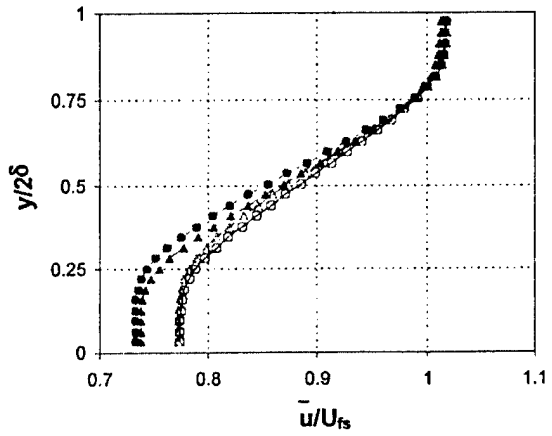

(b)

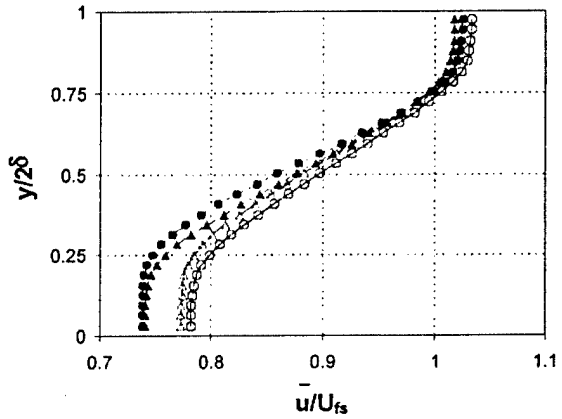

(c)

FIG. 12. Average velocity profiles, u/U_{fs}, as a function of cavitation number for three cross-stream sections of region B derived from the data in Fig. 13. (a) $x/h=20.54$, (b) $x/h=20.96$, (c) $x/h=21.38$. The symbols ○ is for the noncavitating case, △ is $\sigma=0.55$, ● is $\sigma=0.50$, and ▲ is $\sigma=0.45$. Here 1000 individual PIV images were averaged.

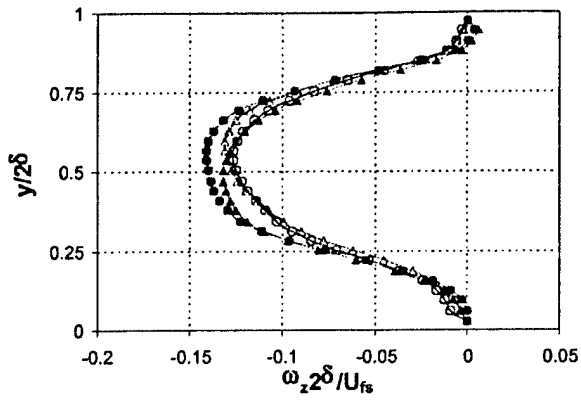

(a)

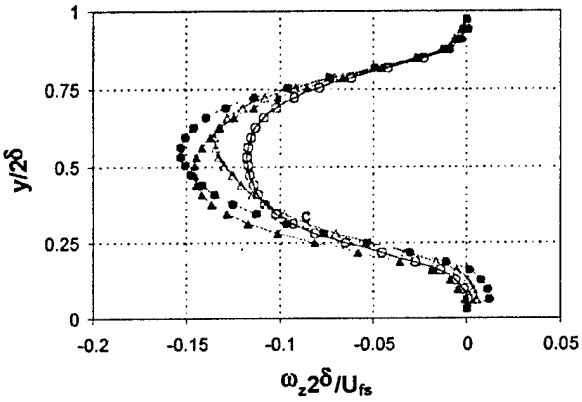

(b)

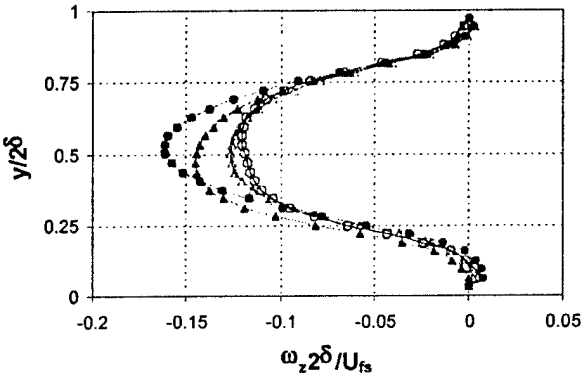

(c)

FIG. 13. Average vorticity profiles, $\omega_z 2\delta/U_{fs}$, as a function of cavitation number for three cross-stream sections of region B: (a) $x/h=20.54$, (b) $x/h=20.96$, (c) $x/h=21.38$. ○ is the noncavitating case, △ is $\sigma=0.55$, ● is $\sigma=0.50$, and ▲ is $\sigma=0.45$.

an uncertainty in the position of $\Delta x/2\delta \sim 0.001$, the uncertainty in the nondimensionalized vorticity and strain rate is approximately ± 0.10. After averaging, the uncertainty in the vorticity and strain profiles is ± 0.003. Differences of less than ± 0.006 are within the uncertainty of the measurement.

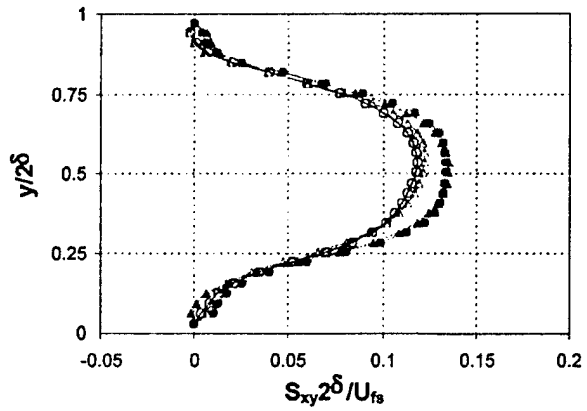

(a)

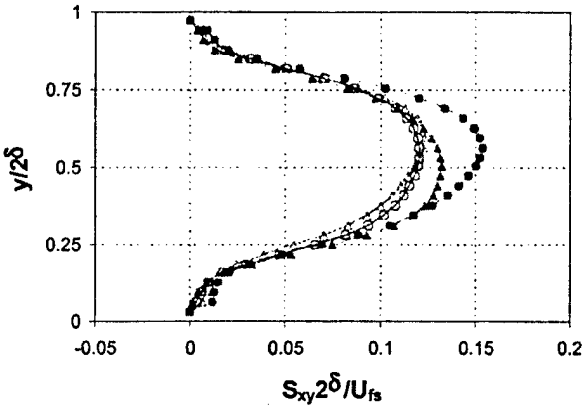

(b)

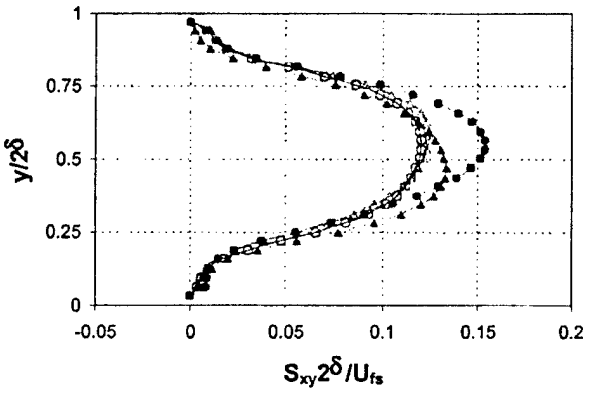

(c)

FIG. 14. Average strain rate profiles, $S_{xy}2\delta/U_{fs}$, as a function of cavitation number for three cross-stream sections of region B: (a) $x/h=20.54$, (b) $x/h=20.96$, (c) $x/h=21.38$. ○ is the noncavitating case, △ is $\sigma=0.55$, ■ is $\sigma=0.50$, and ▲ is $\sigma=0.45$.

The maximum absolute vorticity levels are higher in the cavitating flows than in the noncavitating flow, especially for the cavitation numbers $\sigma=0.50$ and $\sigma=0.45$. Similar results for the strain rate profiles are shown in Fig. 14. The higher vorticity and strain rates are consistent with the decrease in the shear layer thickness at lower cavitation numbers. The case of $\sigma=0.50$ is again anomalous with the highest maximum vorticity and strain rate magnitudes. A possible explanation for this may be the significant increase in the void fraction beneath the shear layer at the lowest cavitation numbers. This is observed in Figs. 5(d) and 5(e). Increasing concentration of bubbles beneath the shear layer reduces the mean density of this recirculating flow. This, in turn, would reduce the shear stresses across the layer upstream of region B.

F. Comparison between the turbulent fluctuations of the noncavitating and the cavitating flows in region B

Figures 15, 16, and 17 present profiles of the mean Reynolds stresses $\overline{u'u'}/U_{fs}^2$, $\overline{v'v'}/U_{fs}^2$, and $-\overline{u'v'}/U_{fs}^2$ at the three cross-stream locations. The average velocity at each vector location was determined, and this local average velocity was subtracted from each vector to determine the fluctuation velocity components u' and v' for each image. This data was then used to compute the average Reynolds stresses. Figure 18 shows the convergence plots for the Reynolds stresses at a point in the middle of the domain. It indicates that 1000 images are sufficient to achieve a statistically steady average.

Consider the trends in $\overline{u'u'}/U_{fs}^2$ in Fig. 15. First, it should be noted that the location of maximum fluctuations is not in the center of the shear layer. By the time the flow is in region B, the shear layer is in the diffuser and is no longer similar to the planar mixing layer of region A. The $\overline{u'u'}/U_{fs}^2$ profiles are not significantly changed with decreasing cavitation number, and the magnitude of the fluctuations increases with the extent of cavitation upstream. Laberteaux and Ceccio[5] showed that the collapse of cavitation bubbles leads to the production of turbulence within the flow, and this increase in streamwise turbulence may result from this mechanism. Again, the case of $\sigma=0.50$ is anomalous, as the level of turbulence observed at the lower boundary of the shear layer is reduced for just this case.

For the measurements of $\overline{v'v'}/U_{fs}^2$ (Fig. 16), the presence of cavitation has reduced the extent of the maximum cross-stream fluctuations compared with the noncavitating flow by as much as 30%. These results suggest that the presence of cavitation either damps out the cross-stream fluctuations or reduces their production. Similar trends are found in the measurements of $-\overline{u'v'}/U_{fs}^2$ (Fig. 17), where an increase in the extent of cavitation reduced the correlation between the streamwise and cross-stream velocities. The streamwise stretching of a vortex will lead to an increase in the rotation rate of the vortex; thus, streamwise velocity fluctuations are coupled to cross-stream fluctuations. Belahadji *et al.*[22] suggested that the presence of vapor in the cores of such vortices modifies the vortex-stretching process by decoupling the rate of vortex straining from the rotation rate. As a noncavitating vortex is stretched, the conservation of angular momentum implies that the rotation rate will increase and the pressure in the viscous core will decrease. However, the core of a cavitating vortex can maintain a constant pressure, and stretching

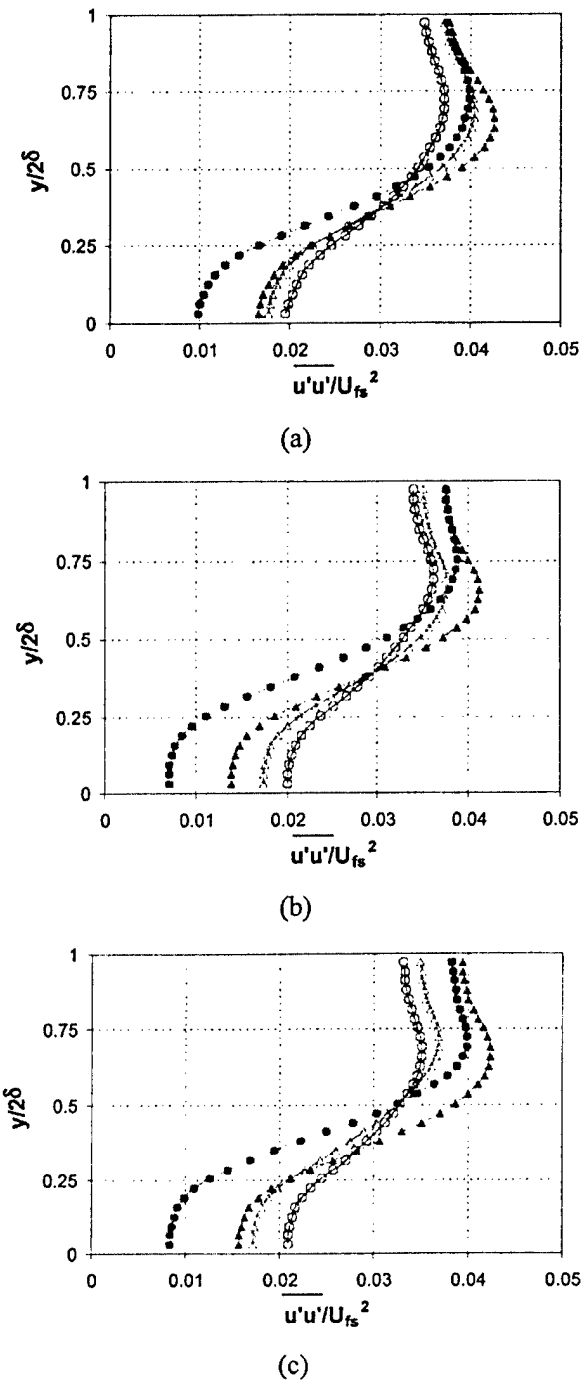

FIG. 15. Mean Reynolds stress profiles, $\overline{u'u'}/U_{fs}^2$, as a function of cavitation number for three cross-stream sections of region B: (a) $x/h=20.54$, (b) $x/h=20.96$, (c) $x/h=21.38$. ○ is the noncavitating case, △ is $\sigma=0.55$, ● is $\sigma=0.50$, and ▲ is $\sigma=0.45$.

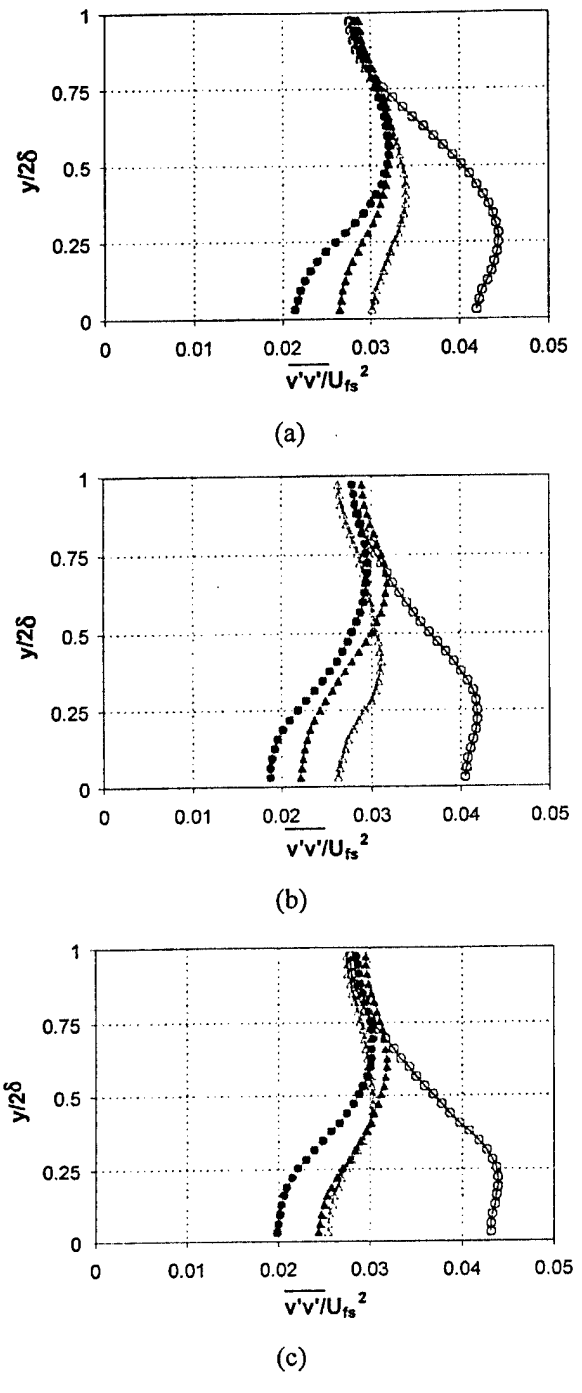

FIG. 16. Mean Reynolds stress profiles, $\overline{v'v'}/U_{fs}^2$, as a function of cavitation number for three cross-stream sections of region B: (a) $x/h=20.54$, (b) $x/h=20.96$, (c) $x/h=21.38$. ○ is the non-cavitating case, △ is $\sigma=0.55$, ● is $\sigma=0.50$, and ▲ is $\sigma=0.45$.

will result only in the production of more core vapor with little change in the vortex core diameter. Such a mechanism could be responsible for a decrease in the production of cross-stream fluctuations and a reduction in the stress $-\overline{u'v'}/U_{fs}^2$, as seen in the data. However, these distributions also exhibit some anomalies. Once more, the case of $\sigma=0.50$ shows the largest reductions in average Reynolds stresses compared to the noncavitating case. And, the case of $\sigma=0.45$ shows increasing values of $-\overline{u'v'}/U_{fs}^2$ near the top edge of the shear layer.

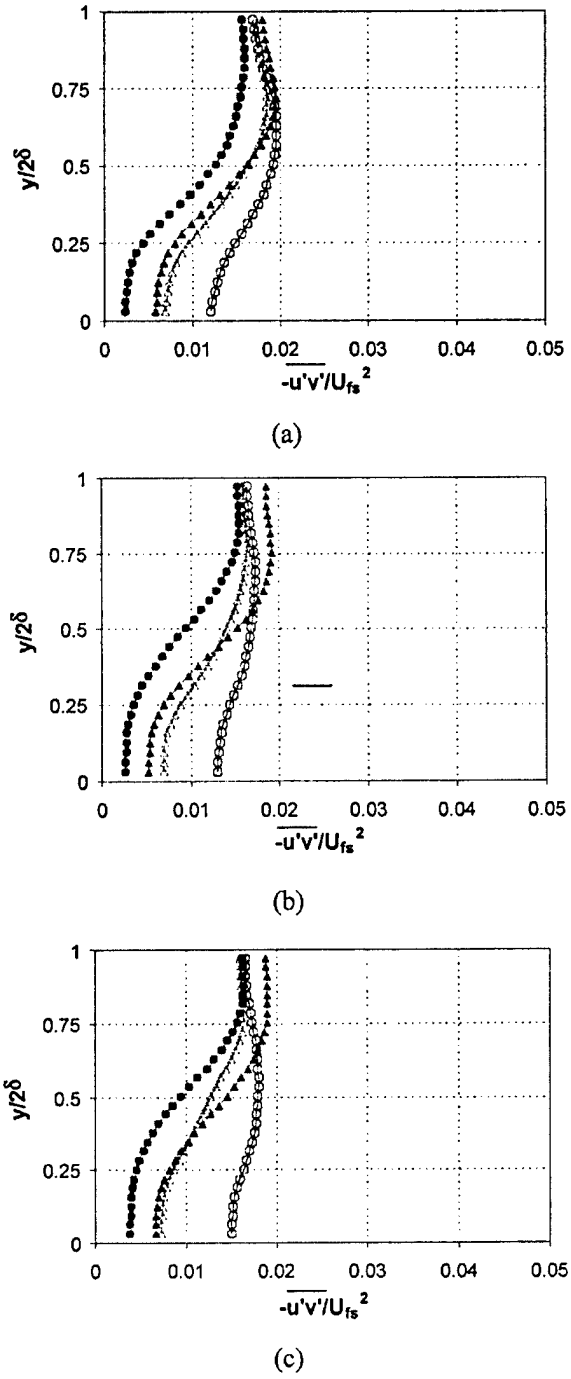

FIG. 17. Mean Reynolds stress profiles, $-\overline{u'v'}/U_{fs}^2$, as a function of cavitation number for three cross-stream sections of region B: (a) $x/h=20.54$, (b) $x/h=20.96$, (c) $x/h=21.38$. ○ is the non-cavitating case, △ is $\sigma=0.55$, ● is $\sigma=0.50$, and ▲ is $\sigma=0.45$.

The PIV images were analyzed to reveal the probability distributions of the instantaneous vorticity and strain rates measured within region B. Figures 19 and 20 show the probability distribution for the values of vorticity and strain rate taken from 1000 images. Differences are only observed at

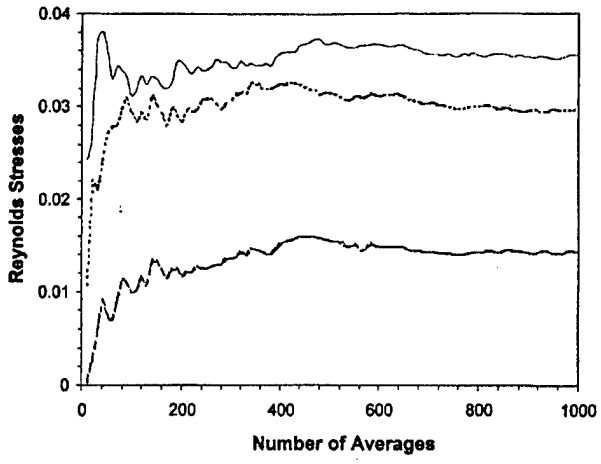

FIG. 18. Convergence plot for the mean Reynolds stresses at a point in the middle of region B: $\overline{u'u'}/U_{fs}^2$ (solid line); $\overline{v'v'}/U_{fs}^2$ (short-dashed line); and $-\overline{u'v'}/U_{fs}^2$ (long-dashed line).

the extreme positive and negative values, and the trends with cavitation number observed in the profiles can be detected in variations of the histograms. For the case of $\sigma=0.50$, there is a slight shift toward a higher probability of strong negative vorticity and strong positive strain rates, and these trends reverse for the condition of $\sigma=0.45$.

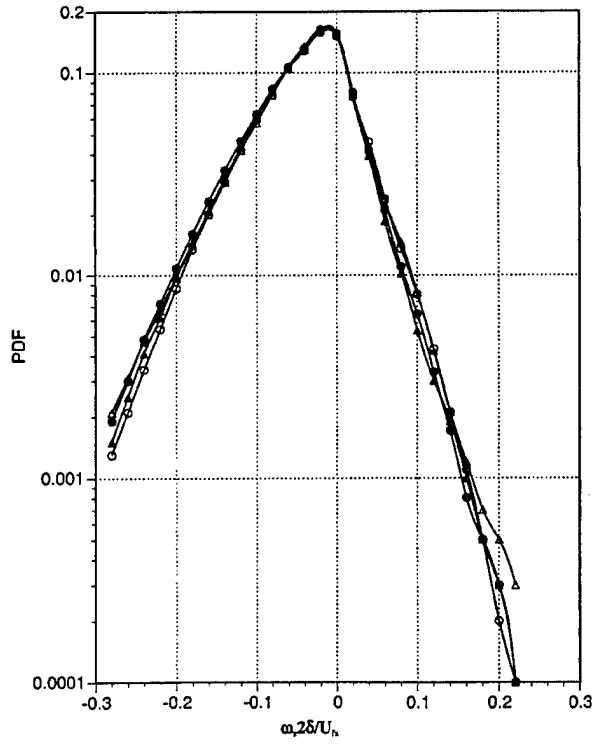

FIG. 19. Probability density function of the normalized vorticity, $\omega_z 2\delta/U_{fs}$, measured in region B for varying cavitation numbers. The measurements from 1000 PIV images are presented. ○ is the noncavitating case, △ is $\sigma=0.55$, ● is $\sigma=0.50$, and ▲ is $\sigma=0.45$.

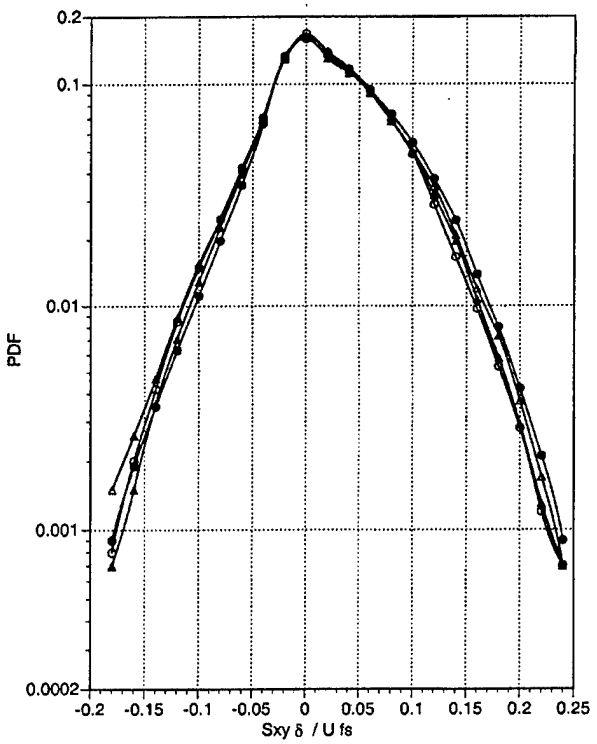

FIG. 20. Probability density function of the normalized strain rate, $S_{xy}\delta/U_{fs}$, measured in region B for varying cavitation numbers. The measurements from 1000 PIV images are presented. ○ is the noncavitating case, △ is $\sigma=0.55$, ● is $\sigma=0.50$, and ▲ is $\sigma=0.45$.

G. Influence of cavitation on the shear stress across the shear layer

The data presented above indicate that the shear layer was modified by the cavitation, but only subtly. As we are examining the flow after the collapse of the cavitation bubbles, interpretation of the results can be problematic, but it appears that the cavitation resulted in an increase of the mean shear rate across the layer and a decrease in the Reynolds stresses within the layer. While the flow examined here is not a classical mixing layer, the scaling of a variable density mixing layer may be useful in examining this flow (see Hermanson and Dimotakis[31] for a complete derivation). A similarity variable can be defined as

$$\eta = y/\delta(x),$$

where x is the streamwise direction and y is the cross-stream direction. The velocity distribution across the shear layer takes the form

$$U(\eta) = \hat{s} U_1 \frac{df(\eta)}{d\eta}$$

and

$$\tilde{V}(\eta) = \hat{s} U_1 \left(\eta \cdot \frac{df(\eta)}{d\eta} - f(\eta) \right) \frac{d\delta}{dx},$$

where U is the mean streamwise velocity, $\rho\tilde{V} = \rho V + \overline{\rho' v'}$, and U_1 is the velocity of the high-speed stream on the mixing layer. The density ratio $\hat{s}(\eta) = \rho/\rho_S$ compares the free-stream density to the local shear layer density. Substitution into the streamwise momentum equation yields

$$-\frac{U_1^2}{\Delta U^2}\frac{d\delta}{dx} f \left(\frac{d\hat{s}}{d\eta} f + \hat{s} \frac{d^2 f}{d\eta^2} \right) = \frac{1}{\rho \Delta U^2}\frac{d\tau}{d\eta} - \frac{\eta}{\rho \Delta U^2}\frac{dP}{d\eta}\frac{d\delta}{dx},$$

where $\tau = -\rho\overline{u'v'}$ is the Reynolds shear stress plus higher-order terms and ΔU is the velocity difference across the shear layer. Here, it is assumed that streamwise velocity fluctuation correlations are small compared to U^2, and that the Reynolds stresses are much larger than the viscous stresses. The pressure gradient term on the right-hand side is small compared to the shear-stress term. The second term on the left results from density gradients in the shear layer. The effect of buoyancy has been neglected here as the flow is momentum dominated. The Richardson number is

$$\mathrm{Ri} \approx \frac{\alpha g \delta_0}{U_{fs}^2} \approx 10^{-5},$$

where g is the gravitational constant.

While the advent of cavitation alters the local density of the shear layer, the maximum reduction in the mean density within the shear layer is less than 1%, based on the void fraction measurements. This is in contrast to reacting shear layers, where the density reduction variation can be as high as 60%. We will assume here that the gradient of density across the shear layer is small and can be neglected. The streamwise momentum equation becomes

$$-\hat{s}\frac{U_1^2}{\Delta U^2}\frac{d\delta}{dx}\frac{d^2 f}{d\eta^2} f \approx \frac{1}{\rho \Delta U^2}\frac{d\tau}{d\eta}.$$

This equation can be integrated numerically for a given measured velocity distribution with the constraint that the shear stresses vanish in the two free-streams. A constraint based on mass conservation can be applied to achieve this result (Hermanson and Dimotakis[31]).

Figure 21 shows the velocity profiles measured in region B [from Fig. 12(a)] scaled with the measured velocity difference across the layer. The profiles are nearly identical, and they are approximated by the function $\tanh[2(y/\delta - 1)]$, and this is approximately the form of

$$\frac{df(\eta)}{d\eta} = \frac{\Delta U}{2U_1}\tanh[2(y/\delta - 1)].$$

The function $f(\eta)$ can be found by integrating $df(\eta)/d\eta$. The maximum value of the shear stress is found on the dividing streamline, where $\tilde{V} = \eta_0 U$. Let us assume that the profiles across the layer are symmetric in $(\eta - \eta_0) = \hat{\eta}$. Both the shear-stress distribution $\tau(\hat{\eta})$ and $d^2 f(\hat{\eta})/d\hat{\eta}^2$ are even functions of $\hat{\eta}$. Consequently, $f(\hat{\eta})$ is an odd function of $\hat{\eta}$. An approximate expression for $f(\hat{\eta})$ is

$$f(\hat{\eta}) \approx \frac{\Delta U}{U_1}\hat{\eta}.$$

Also, the derivative of $df(\hat{\eta})/d\hat{\eta}$ yields

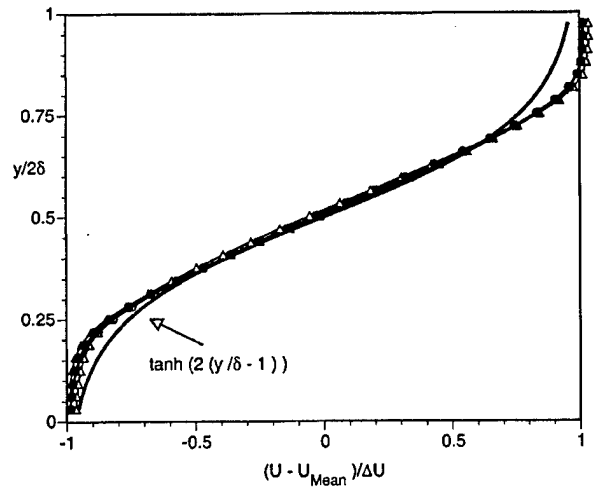

FIG. 21. Scaled velocity profiles, $(\bar{u}-U_{\text{Mean}})/\Delta U$, as a function of cavitation number for three cross-stream sections of region B for $x/h=20.54$ derived from the data in Fig. 14(a): ○ is the noncavitating case, △ is $\sigma=0.55$, ● is $\sigma=0.50$, and ▲ is $\sigma=0.45$. Also shown is the velocity profile $\tanh[2(y/\delta-1)]$.

$$\frac{d^2f(\hat{\eta})}{d\hat{\eta}^2}\approx\frac{\Delta U}{U_1}\operatorname{sech}^2(2\hat{\eta}).$$

These expressions can be integrated to determine an expression for the shear stress across the shear layer:

$$\int f\frac{d^2f}{d\hat{\eta}^2}d\hat{\eta}\approx\frac{\Delta U}{2U_1}[2\hat{\eta}\tanh(2\hat{\eta})-\ln\cosh(2\hat{\eta})-C],$$

where C is a constant chosen such that the shear stress tend to zero for large magnitudes of $\hat{\eta}$. In the limit as $\hat{\eta}\to\infty$, $2\hat{\eta}\tanh(2\hat{\eta})-\ln\cosh(2\hat{\eta})\to\ln(2)=0.693\approx C$. The shear stress distribution is then given by

$$-\frac{1}{4}\frac{d\delta}{dx}[2\hat{\eta}\tanh(2\hat{\eta})-\ln\cosh(2\hat{\eta})-C]\approx\frac{\tau}{\rho\Delta U^2}.$$

The maximum shear stress at $\hat{\eta}=0$ is then

$$C\frac{1}{4}\frac{d\delta}{dx}\approx\frac{\tau_{\max}}{\rho\Delta U^2}.$$

This scaling indicates that the magnitude of the maximum shear stress decreases linearly with a decreasing shear layer growth rate and decreasing mean flow density.

Plane mixing layers have growth rates of $d\delta/dx\approx0.16$, which suggests that $\tau_{\text{Max}}/\rho\Delta U^2\approx0.027$. This estimate is nearly twice the peak measured Reynolds stresses $\tau=-\overline{u'v'}/\Delta U^2\approx0.13$ (Spencer and Jones[32]). With $d\delta/dx\approx0.25$, $\tau_{\text{Max}}/\rho\Delta U^2\approx0.04$. This suggests that the maximum value of the Reynolds stress $(-\overline{u'v'}/U_{\text{fs}}^2)_{\text{Max}}\approx0.02\cdot(\Delta U/U_{\text{fs}})^2$. If ΔU is the measured velocity difference across the layer, $(-\overline{u'v'}/U_{\text{fs}}^2)_{\text{Max}}\approx0.002$, and this is about an order of magnitude smaller than the measured value of between 0.02 and 0.03. However, in the present experiment, the high-speed flow essentially drives a recirculating low speed flow in the manner similar to a rearward facing step, where $\Delta U\approx U_{\text{fs}}$. With this assumption, $(-\overline{u'v'}/U_{\text{fs}}^2)_{\text{Max}}\approx0.02$, which is close to the values measured here.

The above relationship can be used to determine trends in the shear stress with changes in the extent of cavitation within the shear layer. As the cavitation number decreases, the mean density in the cavitating shear layer decreases by less than 2%, and no significant variation was observed in the growth rate, although there is considerable uncertainty in this measurement. The mean profiles in the region just downstream of the cavitation suggest that ΔU in region B increases by about 10% at the lowest cavitation number. A reduction in mean density would suggest a reduction in the shear stresses in the cavitating layer, while an increase in the strain rate within the layer would suggest an increase. An examination of the Reynolds stresses in Fig. 17 indicates that the advent of cavitation reduced the stresses by about a factor of 2, and this is accompanied by a reduction of cross-stream fluctuations shown in Fig. 16. The changes in mean density or growth rate do not account for such a difference, and the changes in the strain rate across the layer suggest an increase in shear stress with cavitation.

Reduction in the Reynolds stresses is most pronounced for the case of $\sigma=0.50$. This is the condition when the cavitation has developed the most without the formation of a large bubbly mixture beneath the cavity. For the case of $\sigma=0.45$, the flow beneath the shear layer is full of large vapor bubbles that are trapped and recirculated [see Figs. 5(d) and 5(e), for example]. It is possible that the extent of the shear across the shear layer is reduced by the presence of this vapor. This could explain why the trend reverses with a further decrease in cavitation number below 0.50.

IV. CONCLUSIONS

Visual observations of the shear layer suggest that the overall formation, growth, and convection of the primary and secondary vortical structures in the shear layer are not significantly affected by the presence of cavitation. The average flow field downstream of the cavitating shear layer is not significantly altered both in terms of average velocities and mean pressure drop across the test section.

The largest differences between the cavitation and the noncavitating flows were in the turbulent fluctuations examined downstream of the cavitating shear layer. The streamwise fluctuations increased by about 15% compared to the noncavitating case in the center of the shear flow. However, the maximum cross-stream fluctuations and Reynolds stresses decreased by about 30%. As bubbles collapse, an increase in turbulence levels is expected (Laberteaux and Ceccio[5,6]). The decrease in the cross-stream fluctuations and Reynolds stresses suggest that the cavitation within the cores of streamwise vortices has decreased the coupling between the streamwise and cross-stream velocity fluctuations. This is consistent with the hypothesis of Belahadji *et al.*[22] whereby cavitation in the cores of the streamwise vortices decoupled the stretching and rotation rate of these flow structures. The reduction in Reynolds stresses downstream of the shear layer is inconsistent with the scaling of the shear stress within the shear layer based on the shear layer growth rate, mean den-

sity, and the mean flow profiles. As these measurements have limited spatial resolution, it may be necessary to examine turbulent fluctuation at smaller scales to resolve this issue.

The production and distribution of turbulent fluctuations seem to have been significantly altered by the presence of developed cavitation. It is problematic to interpret the data from this experiment in the context of a true mixing layer. Moreover, we are left to infer the flow processes within the cavitating layer from observations of the noncavitating flow downstream. It may be necessary to examine the turbulent cavitating flow directly to resolve the questions regarding the shear stress distribution and Reynolds stresses. However, the mean shear and Reynolds stress distribution in turbulent flows can be substantially altered when the rheological behavior of the flow is altered. An example is the addition of high surfactants to a turbulent shear flow. Warholic *et al.*[33] demonstrated that the addition of relatively small quantities of surfactants resulted in the substantial suppression of cross-stream velocity fluctuations and Reynolds stresses in a turbulent channel flow. This resulted in a substantial reduction in the shear stress at the wall of the channel. Similarly, researchers have noted that the addition of microbubbles will lead to the reduction of wall shear stresses, and dynamic shear stress measurements at the wall suggest that the bubbles are also altering the dynamics of the turbulent flow (Merkle and Deutsch[34]). It is therefore possible that the presence of the cavitation within the shear layer modifying the distribution of mean shear stress across the layer through a change in the effective rheology of the flow.

Cavitating wakes have been significantly modified by developed cavitation, especially with respect to the rate of vortex shedding. Such effects were not observed here. The void fraction of the cavitating shear layer was, at most, 2%. It is unclear if the void fraction in the separated region behind the bluff bodies is significantly higher, but this may be the case. Moreover, the dynamics of the shedding process behind bluff object is altered by changes in the pressure field near the bluff body. The presence of developed cavitation can alter the overall pressure field, especially if the cavitating object is confined in a flow channel. In the present study, the presence of the cavitation did not significantly change the average pressure field.

Last, these results suggest that a single-phase simulation of shear flow may be used to determine the extent of the cavitation within the shear flow. A method is needed that can successfully simulate the strongest vortices in the flow over a range of scales. While such single-phase simulations are, at present, difficult to conduct at high Reynolds numbers, methods such as large eddy simulations may eventually be used to reveal the largest vortical structure in a flow field. Once identified, the extent of the cavitation can be estimated. This is particularly true of incipient cavitation where the influence on the underlying shear flow may be neglected.

ACKNOWLEDGMENT

Financial support for this work was provided by the Office of Naval Research through Contract No. N00014-96-0076, Dr. E. P. Rood, Technical Monitor.

[1]C. E. Brennen, *Cavitation and Bubble Dynamics* (Oxford University Press, Oxford, 1995).
[2]K. L. Laberteaux and S. L. Ceccio, "Flow in the closure region of closed partial attached cavitation," 3rd International Symposium on Cavitation, April 1998, Grenoble, France, p. 197.
[3]K. Laberteaux, S. L. Ceccio, V. Mastrocola, and J. Lowrance, "High speed digital imaging of cavitating vortices," Exp. Fluids **24**, 489 (1998).
[4]S. Gopalan and J. Katz, "Flow structure and modeling issues in the closure region of attached cavitation," Phys. Fluids **12**, 895 (2000).
[5]K. R. Laberteaux and S. I. Ceccio, "Partial cavity flows: Part 1—Cavities forming on models without spanwise variation," J. Fluid Mech. **431**, 1 (2000).
[6]K. R. Laberteaux and S. L. Ceccio, "Partial cavity flows: Part 2—Cavities forming on test objects with spanwise variation," J. Fluid Mech. **431**, 43 (2000).
[7]Y. Kawanami, H. Kato, and H. Yamaguchi, "Three-dimensional characteristics of the cavities formed on a two-dimensional hydrofoil," in Ref. 2.
[8]M. Callenaere, J. P. Franc, and J. M. Michel, "Influence of cavity thickness and pressure gradient on the unsteady behavior of partial cavities," in Ref. 2.
[9]G. L. Brown and A. Roshko, "On density effects and large structure in turbulent mixing layers," J. Fluid Mech. **64**, 775 (1974).
[10]C. D. Winant and F. K. Browand, "Vortex pairing: The dynamics of turbulent mixing layer growth at moderate Reynolds numbers," J. Fluid Mech. **63**, 237 (1974).
[11]L. P. Bernal, R. E. Breidenthal, G. L. Brown, J. H. Konrad, and A. Roshko, "On the development of three-dimensional small scales in turbulent mixing layers," 2nd International Symposium on Turbulent Shear Flows, 1981, p. 305.
[12]J. C. Lasheras, J. S. Cho, and T. Maxworthy, "On the origin and evolution of streamwise vortical structures in a plane, free shear layer," J. Fluid Mech. **172**, 231 (1986).
[13]J. C. Lasheras and H. Choi, "Three-dimensional instability of a plane free shear layer: An experimental study of the formation and evolution of streamwise vortices," J. Fluid Mech. **189**, 53 (1988).
[14]R. E. A. Arndt, "Cavitation in fluid machinery and hydraulic structures," Annu. Rev. Fluid Mech. **13**, 273 (1981).
[15]J. Katz, "Cavitation phenomena within regions of flow separation," J. Fluid Mech. **140**, 397 (1984).
[16]J. Katz and T. J. O'Hern, "Cavitation in large scale shear flow," Trans. ASME J. Fluids Eng. **108**, 373 (1986).
[17]T. J. O'Hern, "An experimental investigation of turbulent shear flow cavitation," J. Fluid Mech. **215**, 365 (1990).
[18]R. W. Kermeen and B. R. Parkin, "Incipient cavitation and wake flow behind sharp-edged disks," California Institute of Technology Hydrodynamics Laboratory Report No. 85-4, 1957.
[19]J. O. Young and J. W. Holl, "Effects of cavitation on periodic wakes behind symmetric wedges," J. Fluid Mech. **63**, 237 (1966).
[20]R. E. A. Arndt, "Investigation of the effects of dissolved gas and free nuclei on cavitation and noise in the wake of a sharp-edged disk," Joint IAHR/ASME/ASCE Symposium on Fluid Machinery, Fort Collins, CO, 1978.
[21]R. E. A. Arndt and W. K. George, "Pressure fields and cavitation in turbulent shear flows," *12th Symposium on Naval Hydrodynamics* (National Academy, Washington, DC, 1979).
[22]B. Belahadji, J. P. Franc, and J. M. Michel, "Cavitation in the rotational structures of a turbulent wake," J. Fluid Mech. **287**, 383 (1995).
[23]D. L. George and S. L. Ceccio, "Cavitation and multiphase flow laboratory at the University of Michigan," 24th American Towing Tank Conference, edited by P. Johnson, 1995.
[24]I. Wygnanski and H. E. Fiedler, "The two-dimensional mixing region," J. Fluid Mech. **41**, 327 (1970).
[25]P.-W. Yu and S. L. Ceccio, "Bubble populations downstream of an attached cavity," J. Fluid Mech. **119**, 782 (1997).
[26]M. A. Hernan and J. Jimenez, "Computer analysis of a high-speed film of the plane turbulent mixing layer," J. Fluid Mech. **119**, 323 (1982).
[27]J. Jimenez, "A spanwise structure in the plane shear layer," J. Fluid Mech. **132**, 319 (1983).
[28]J. Jimenez, M. Cogollos, and L. P. Bernal, "A perspective view of the plane mixing layer," J. Fluid Mech. **152**, 125 (1985).
[29]L. Briançon-Marjollet and L. Merle, "Inception, development and noise of

a tip vortex cavitation," 21st Symposium on Naval Hydrodynamics, Trodheim, Norway, 1996.
[30]R. E. A. Arndt and A. P. Keller, "Water quality effects on cavitation inception in a trailing vortex," J. Fluids Eng. **114**, 430 (1992).
[31]J. C. Hermanson and P. E. Dimotakis, "Effects of heat release in a turbulent, reacting shear layer," J. Fluid Mech. **199**, 333 (1989).
[32]B. W. Spencer and B. G. Jones, "Statistical investigation of pressure and velocity fields in the turbulent two stream mixing layer," 11th Aerospace Sciences Meeting, 1971, AIAA Paper 71-613.
[33]M. D. Warholic, G. M. Schmidt, and T. J. Hanratty, "The influence of a drag-reducing surfactant on a turbulent velocity field," J. Fluid Mech. **388**, 1 (1999).
[34]C. L. Merkle and S. Deutsch, "Microbubble drag reduction in liquid turbulent boundary layers," Appl. Mech. Rev. **45**, 103 (1992).

TIP-LEAKAGE VORTEX INCEPTION ON A DUCTED ROTOR

Carolyn Q. Judge, Ghanem F. Oweis, Steven L. Ceccio
University of Michigan
Ann Arbor, MI, USA

Stuart D. Jessup, Christopher J. Chesnakas, David J. Fry
Naval Surface Warfare Center - Carderock Division
Carderock, MD, USA

Abstract

The tip-leakage vortex occurring on a ducted rotor was examined using both three component Laser Doppler Velocimetry (LDV) and planar Particle Imaging Velocimetry (PIV). The vortex strength and core size were examined for different vortex cross sections downstream of the blade trailing edge. The variability of these quantities are observed with PIV and the average quantities are compared between LDV and PIV. Developed cavitation is also examined for the leakage vortex. The implication of vortex variability on cavitation inception is discussed.

1 Introduction

Tip-vortex cavitation is a source of noise, propeller-induced hull vibration and erosion of downstream rudders. With a ducted propeller, the tip clearance vortex can cause damage to the duct surface as well. The pressure difference across the two sides of the blade along with the presence of a gap between the duct and propeller blade result in a tip clearance or leakage flow. The leakage flow interacts with the through-flow across the suction side of the blade to form a sheet of vorticity that rolls up into a tip clearance vortex. Tip-vortex cavitation occurs when the pressure in the core of this vortex drops below vapor pressure and small bubbles within the vortex core begin to explosively grow. With further decreases in pressure, the core of the vortex can fill with vapor.

Researchers have examined the flow of tip and leakage vortices in order to determine when cavitation will occur and to develop predictive scaling laws. Recent studies of tip-vortex cavitation are reviewed by Fruman *et al.*(1992), Fruman *et al.*(1995), and Maines and Arndt (1997). Research on leakage-vortex cavitation is more limited, and a recent review is given by Boulon *et al.* (1999). Of particular note is the study of Farrell and Billet (1994) where the scaling of leakage vortex inception was presented.

Scaling of vortex cavitation inception often follows the idea of McCormick (1962) whereby the pressure within the core of the vortex can be related to the viscous flow over the lifting surface and the lift that the surface produces. If axisymmetric vortex flow is assumed, the local depression of pressure at the center of the vortex is proportional to the circulation of the vortex and the size of the viscous vortex core. McCormick assumed that the core size is proportional to the mean boundary layer thickness on the lifting surface, and that the vortex circulation was proportional to the lift coefficient, C_L. Reynolds number dependence arises from the assumption that the boundary layer thickness grows as $Re^{1/5}$. Lastly, it is assumed that the vortex will cavitate when the core pressure falls below vapor pressure. When combined, these relations lead to the scaling:

$$\sigma \approx C_L^2 Re^{2/5}. \tag{1}$$

This scaling has been successfully used to determining the point of cavitation desinence across Reynolds numbers. Scaling of cavitation inception must also include the effect of both the dissolved and free gas content

in the flow. Farrell and Billet (1994) discuss how McCormick scaling should be modified for application to tip-leakage flows, especially with regard to the choice of scaling for the core size with varying tip clearance.

While the above scaling has proven useful and predictive, there are features of tip-vortex flows that are not directly captured. These include the dynamics of the vortex during roll-up near the point of vortex formation, the effect of secondary vorticity in the roll-up region, the influence of axial flow within the vortex core, and the effect of turbulence near and within the core (Pauchet, 1997). For tip-leakage flows, there is the added influence flow near the shroud.

We wish to examine the process of tip-leakage vortex cavitation inception and its scaling as it occurs on a ducted rotor. Our overall goal will be to determine what physical processes are at work within the flow field to lead to the inception of discreet cavitation events. As in previous studies of vortex cavitation inception, we will examine the flow field using three-component Laser Doppler Velocimetry (LDV). LDV provides time-averaged measurements of the three-dimensional flow-field with relatively high spatial resolution. However, it is well known that global unsteadiness of the vortex flow field ("vortex wandering") can lead to erroneous interpretation of average flow fields, especially with regard to the estimation of turbulent flow quantities (Straka and Farrell, 1992). Consequently, we have combined the LDV measurements with instantaneous velocity field measurements acquired with planar Particle Imaging Velocimetry (PIV) to examine the variability in the vortical flow. Tip-vortex cavitation and near-tip velocity distributions were measured on a three-bladed propeller designated "Propeller 5206". The tests were performed in the NSWCCD 36-inch water tunnel. Presented here are some preliminary results of this study and an accompanying discussion of their implications.

2 Experimental Setup

Water Tunnel All measurements were made in the David Taylor 36-inch Variable Pressure Water Tunnel. The tunnel is a recirculating design with interchangeable test sections. (See Brownell, 1962, for a detailed description of the water tunnel). The 36-inch diameter, open jet test section was used for these tests. For these test, the propeller was driven using the upstream dynamometer. Inflow to the propeller was uniform except for the wakes from three upstream shaft support struts.

Propeller Model Propeller 5206 is a three bladed rotor designed to operate in a cylindrical duct. The duct in this case is a cylindrical extension of the NSWCCD 36-inch water tunnel flow nozzle. This configuration produces an inner duct diameter of 0.8636 m (34 inches), the largest propeller operated in the 36-inch water tunnel. The rotor can be operated at speeds up to 500 rpm resulting in blade Reynolds Numbers on the order of 1/4 of full scale.

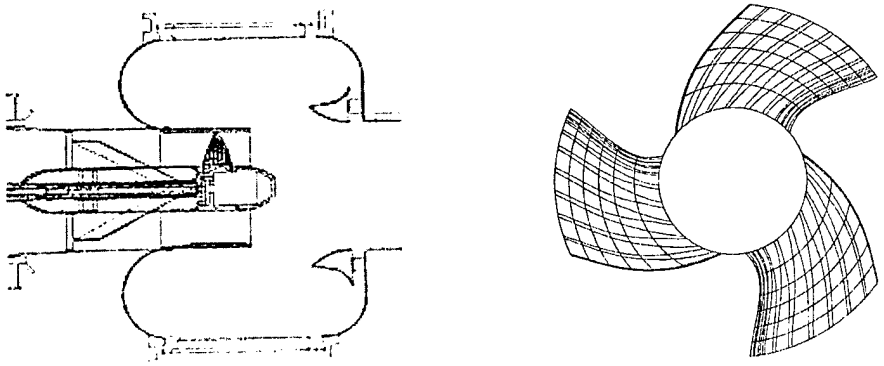

Figure 1: Propeller 5206 in the 36-inch water tunnel at the Naval Surface Warfare Center, Carderock Division and a view of the propeller along the shaft axis

The rotor has a diameter of 0.8504 m (33.475 inches), maintaining a $0.015R_P$ (Radius $R_P = 0.4252$ m) tip clearance resulting in a 6.67 mm (0.2625 in) tip gap. The blade chord-length is a constant 0.381 m (15 in) across the span. Blade thickness approaches 10% of chord at the tip. The tip geometry is simple with a

constant 3.175 mm (1/8 in) radius wrapped about the tip. The ratio of the tip clearance to the maximum thickness at the tip is 0.17, which is near the optimum value of 0.2 reported by Farrell and Billet (1994). The propeller was made using a numerically controlled milling process and manufactured to tolerances of approximately 0.1 mm (0.004 in) from a monobloc 6061T6 aluminum forging. The blade section is a NACA 66, DTMB (David Taylor Model Basin) modified thickness form, with $a = 0.8$ meanline camber, with trailing edges thickened to incorporate a typical anti-singing trailing edge bevel. The blade pitch was reduced at the hub and tip to minimize root and tip cavitation. Table 1 summarizes the blade geometry. Figure 2 shows the test setup with the propeller, duct, LDV and PIV systems as well as the trajectory of the developed cavitating vortex.

Table 1. Propeller 5206 Blade geometry description.

r/R_P	C/D	P/D	I_T/D	T/C	F/C	$\theta_s, Degrees$
0.416	0.446	0.92	-0.0063	0.172	-0.065	-0.4
0.5	0.446	1.135	0.0063	0.148	0.0	4.2
0.6	0.446	1.22	0.0145	0.119	0.037	10.0
0.7	0.446	1.175	0.0227	0.102	0.047	15.90
0.8	0.446	1.087	0.0309	0.100	0.047	21.5
0.9	0.446	0.995	0.0391	0.100	0.038	26.3
1.0	0.446	0.905	0.0473	0.100	0.02	30.0

R_P, Tip radius
C, Chordlength
P, Pitch
I_T, total rake, axial displacement of blade sections relative to propeller centerline
T, Blade section thickness
F, Blade section camber
θ_s, Blade section skew, angular displacement of blade sections relative to blade line perpendicular to the hub

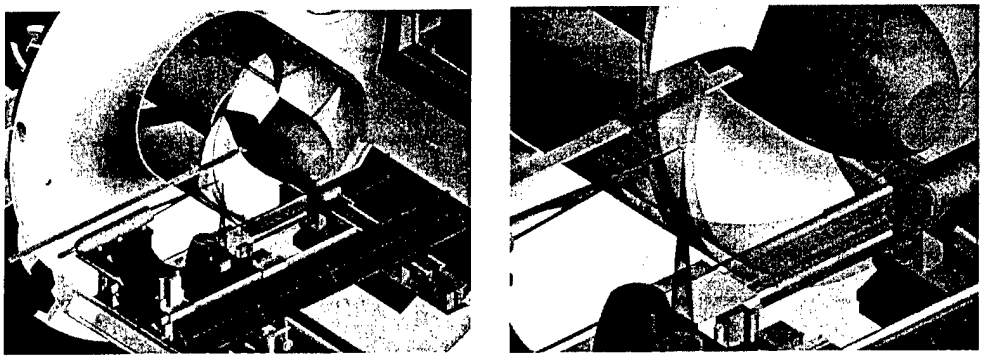

Figure 2: A drawing of the propeller with the duct, LDV system, PIV system, and vortex trajectory. Note the LDV laser beams and the PIV laser sheet and camera. The camera is looking up perpendicular to the laser sheet. The camera mount is on the same traverse as the LDV lasers.

Test Conditions Operation of the propeller poses interesting challenges due to its large size and its complete blockage of the test section flow. Under initial operation of the propeller, attempts to run at its design advance coefficient of $J = 0.75$ required completely shutting down the water tunnel impeller. At around 500 rpm, the rotor mass flow was such that the impeller would begin to free wheel, reducing the flow restriction of the stationary impeller blades and thus dropping the measured rotor thrust and torque. A unique feature of the 36-inch Water Tunnel is the controllable pitch impeller blade, which permits impeller operation over various speeds and blade pitch. It was found that by reducing the pitch of the impeller blades to around zero,

the tunnel flow could be controlled, enabling the rotor to operate over a relatively large range of advance coefficients, $0.65 < J < 1.0$. The standard test conditions at 500 rpm, the highest speed tested, was as follows in the table below. The inlet pressure was maintained high enough (45 psia for 500 rpm) during the LDV and PIV measurements to suppress cavitation.

Table 2. Measured flow conditions.

RPM	Advance Coefficient, J	Velocity ft/s (m/s)	Thrust lbs (kN)	Torque ft-lbs (N-m)	K_T	K_Q	$Re_{0.7}$
500	0.972	22.85 (6.89)	2560 (11.39)	1280 (1735)	0.314	0.056	7×10^6

The operating advance coefficient was selected to produce a typical leakage vortex, without unwanted flow conditions over the blade. The operating $J = 0.971$ was increased relative to design $J = 0.75$ to avoid the formation of the leakage vortex at the leading edge. Additional increase in J was avoided to prevent the occurrence of pressure side leading edge cavitation near the blade tip.

High-Speed Video Camera Photos of the cavitating vortex were taken with a Broadcast quality, Sony Digital Betacam camera. Examples of the cavitating vortex are shown in Figures 12 and 13.

Laser Doppler Velocimetry An all fiber-optic LDV system allowed for three component velocity measurements. The measurement volume was positioned at a point in the horizontal plane containing the propeller axis. The probe volumes are ellipsoidal, 0.7 x 0.7 x 1.3 mm. The probe volumes for the axial and tangential components are coincident, and are oriented with the long axis on a radial line. The probe volume for the radial component is perpendicular to the other two volumes, with the long axis on a tangential line.

LDV measurements were taken upstream and downstream of the rotor. A window upstream of the rotor permitted the measurement of axial and tangential velocities along a radial line upstream of the rotor. Figure 2 shows the windows installed in the shroud to permit measurement of the tip-leakage flow. Three velocity components were measured. The position of the shaft was encoded with an 8192 counts/revolution signal, which was recorded with each velocity measurement. The measurements are grouped into 1024 circumferential positions, each 8 encoder counts wide. At each measurement point, 300,000 velocity measurements were made. This means that each component of each vector on a plot respresents approximately 100 velocity measurements. Doppler signals were analyzed with a TSI Model IFA 655 Digital Burst Correlator. The processor performs a 256-sample, double-clipped, autocorrelation on each Doppler burst, allowing the measurement of velocity even when the signal-to-noise ratio is low. The processors were operated in the random mode. The fiber-optic LDV system consisted of two 3.25 inch TSI model 9832 fiber optic probes. The two probes were rigidly mounted together on a traverse that could translate in the axial and radial directions. The horizontal probe utilized the green (514.5 nm) and violet (476.5 nm) beams of the argon-ion laser to measure the tangential and axial components of velocity, respectively. The vertical probe utilized the blue (488 nm) beam of the argon-ion laser to measure the radial component of velocity.

Particle Image Velocimetry The PIV measurements were made using two Quanta-Ray PRO-Series Pulsed Nd:YAG lasers rated at 800 mJ/pulse output at 532 nm. The laser output was formed into a light sheet of 5 mm thickness. The light sheet passed through windows in the water tunnel and duct to illuminate the flow, and the sheet was oriented parallel to the propeller-shaft axis (Figure 2). The axial position of the camera and sheet were moved to place the mean center of the vortex in the center of the image. Silcon Carbide particles of mean diameter 1 μm were added the flow. A LaVision Flowmaster 3S PIV/PTV system was used to control the firing of the lasers and synchronize image capture with a digital imager, a 1280 x 1024 pixel cross-correlating camera with 12 bit resolution. The camera axis was perpendicular to the laser sheet and recorded the in-plane motion of the tracer particles. The light sheet was sufficiently thick to reduced the number of particles that entered or exited the light sheet due to strong cross-plane flow velocities. The camera was contained in a water-proof housing within the test section of the water tunnel.

The image field-of-view was 24 by 30 mm, and the lenses on the camera were chosen to have a depth-of-field much larger than the thickness of the light sheet. The PIV images were spatially calibrated by taking images of a registration target in the image plane. Images of the target were taken in the filled test section.

The double pulsed PIV images were analyzed using the LaVision software DaVis version 5.4.4. An adaptive multi-pass image process was employed starting with interogation windows of 64 x 64 pixels and

repeating with a final interrogation windows of 32 x 32 pixels. The spatial resolution of the velocity vector field is 0.75 mm. There were typically fewer than 10% bad vectors before postprocessing. A three-by-three gaussian smoothing filter was used on the vector fields. Averages were calculated from 532 individual PIV images.

With the advantage of the high spatial resolution of the PIV vector fields, it was possible to assess the vortex characteristics such as its core radius by direct measurement. The core radius was defined as the radius of a circle with an area equivalent to that enclosed by the polygon centered at the point of minimum speed and formed by the points of maximum speed magnitude positions (core contour). We will refer to the average value of these maximum speeds as the tangential speeds, V_t. The maximum tangential speed value on the core contour is denoted $V_{t_{max}}$. The strength of the vortex was calculated by integrating the vorticity vector over the core area. The vorticity vector at each cell (square) was calculated from the following formula, $w_z = (\oint_c \vec{u} \cdot d\vec{l})/(\oint_c dA)$; which is the circulation, or the line integral of the velocity around a closed path, c, enclosing the cell, divided by the area enclosed by c. The path c is a concentric square with the cell of interest and having twice the side length. The velocities from the eight neighboring cells, four at the sides and four at the corners of the cell under consideration were involved in the calculation. The area enclosed by the path c was made up of the area of the cell under consideration plus $1/2$ the area of the four side cells plus $1/4$ the area of the four corner cells. Three methods of vector field averaging are presented below: simple-averaging, center-averaging based on the location of minimum speed near the vortex core, and center-averaging based on the position of maximum vorticity near the vortex core.

3 Flow Upstream of the Rotor

Figure 3 shows the axial and tangential flow upstream of the rotor. The flow was measured at $x/R_P = -0.362$ where x is measured along the axial flow direction, and $x = 0$ corresponds to the center of the 12-inch (0.3048 m) long propeller hub. R_P is the radius of the rotor. The LDV velocity measurements were non-coincident and taken at various radial positions. The advance coefficient was $J = 0.983$ and data was taken at 250 and 500 rpm. U_x is the velocity in the axial direction, U_t is the tangential velocity, and U_0 is the tunnel flow velocity. The black line shows the axial velocity, the red line shows the tangential velocity, the solid points are for 250 rpm, and the outlined points are for 500 rpm. The boundary layers on the duct and on the hub can be seen. The duct boundary layer has a thickness of about $0.07R_P$. This corresponds to about 5 times the tip-clearance dimension. The tangential velocities are nearly zero near the tip.

4 Average Tip-Leakage Vortex Flow

LDV and PIV were used to measure the average flow near the tip of the blade. Presented here are planar velocity fields. The plane is parallel to the axis and corresponds to an axial distance $\Delta x/R_P = 0.071$ and to the radial distance $\Delta r/R_P = 0.056$. The axial position was moved to center the vortex for images taken at different blade delays. As the rotating blade passes through this plane, the tip-leakage vortex intersects the image plane, and the axis of the vortex is almost perpendicular to the plane.

Figure 4 shows a schematic diagram of the LDV and PIV vector fields with respect to the duct wall and the propeller blade. The images are taken such that the blade is moving into the paper. The leakage vortex is moving from the pressure side of the blade to the suction side showing a counterclockwise rotation when viewed from below (as the PIV camera imaged the flow.). The duct is at the top of the image and the mean tunnel flow is moving from left to right through the plane. The angular position of the rotor, θ, is measured with respect to this plane. When θ equals zero, the trailing edge of the blade intersects the plane, and as θ increases, the blade moves farther away. This distance is presented as $S = \theta R/C$ where C is the chord of the blade.

It is interesting to compare the average flow fields measured with LDV and PIV. Figure 5 presents velocity fields measured with LDV, on the left, and PIV, on the right. The LDV is shown with only 2-components of velocity for comparison with the PIV. The PIV has been simple-averaged over 532 images for comparison with LDV measurements. The PIV velocity field shows good spatial resolution and matches the LDV measurements.

Propulsor Inflow at 250 and 500 rpm

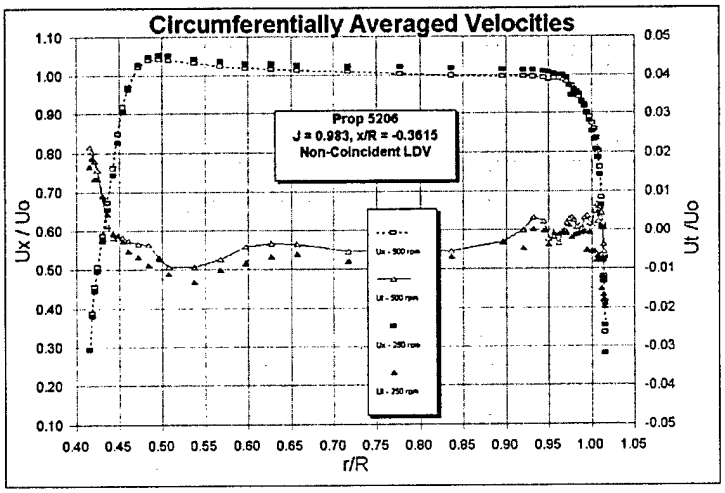

Figure 3: Upstream non-coincident LDV velocity measurements at various radial positions at an advance coefficient of $J = 0.983$and at an axial location of $x/R_P = -0.3615$. U_x is the velocity in the axial direction, U_t is the tangential velocity, and U_0 is the tunnel flow velocity. These measurements were taken at 500 and 250 rpm. The black line is the axial velocity and the red line is the tangential velocity. The solid points are for 250 rpm and the outlined points are for 500 rpm.

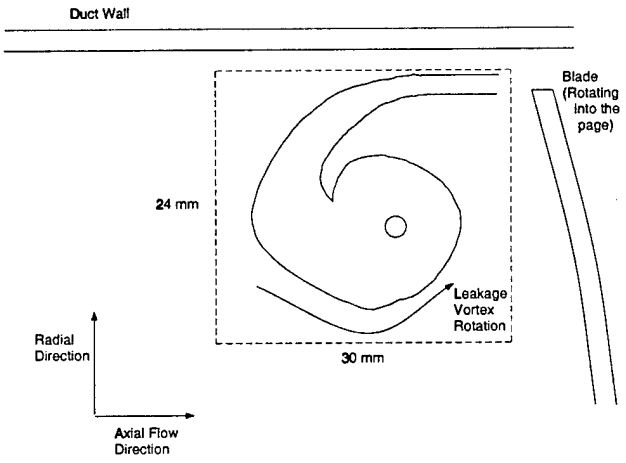

Figure 4: Schematic diagram of LDV and PIV velocity fields. Note that the images are taken such that the blade is moving into the paper (see Figure 2).

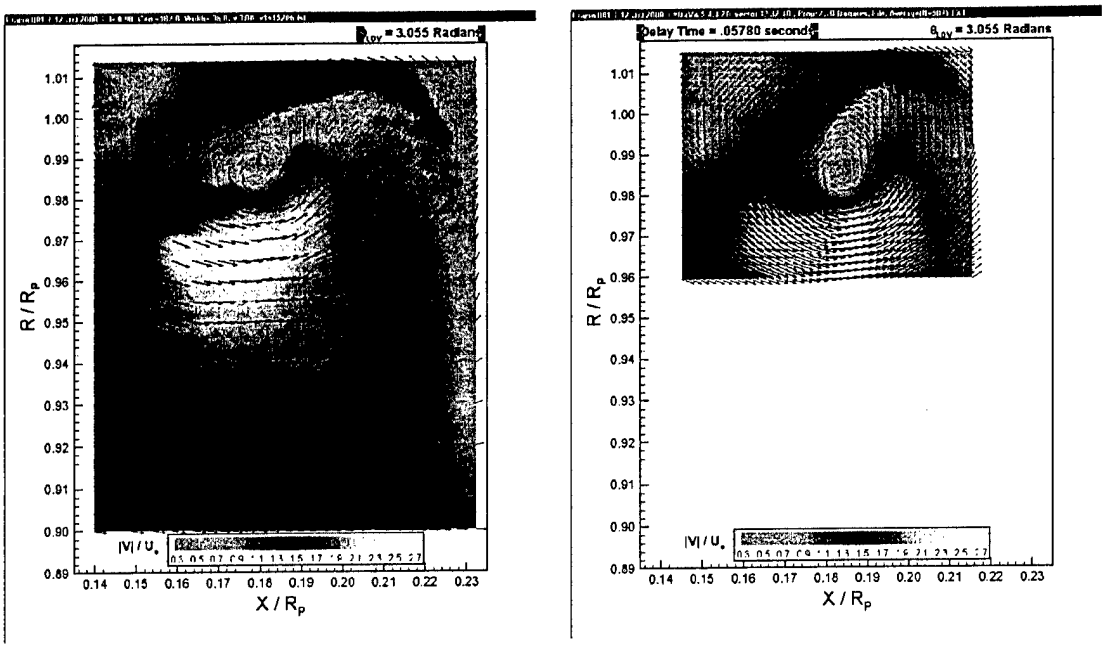

Figure 5: LDV and PIV velocity vectors for S=0.0296 at 500 rpm and 45 psia. The contour color shows the vector magnitude. x/R_P is the non-dimensional distance in the axial direction and r/R_P is the non-dimensional distance in the radial direction. The PIV is averaged over 532 images. The LDV is shown with only 2-components of velocity for comparison with the PIV. The LDV has a covers a larger domain, but the PIV shows good spatial resolution and matches the LDV velocity measurements.

It is important to remember that the vortical flow near the trailing edge is typically three dimensional, and that the PIV image is only a two-dimensional cut of this flow averaged across the PIV imaging light sheet. This is illustrated in Figure 6. Here a comparison is made between 2-component and 3-component LDV measurements. On the left is a 2-component velocity field parallel to the PIV measurement plane. On the right is the velocity field of a plane that was slightly tilted. Because the vortex does not necessarily cut the PIV measurement plane at a right angle, the vortex on the left appears less axially symmetric. The axial symmetry is recovered after tilting the plane. Consequently, it is important not to interpret the PIV images as perpendicular cuts of a two-dimensional vortex. The PIV imaging plane remained parallel to the axial flow direction, and the vortex may not intersect it at a right angle.

5 Variability of the Tip-Leakage Vortex Flow

While only a 2-dimensional realization of the flow, the advantage of the PIV visualization is the possibility of capturing many instantaneous flow fields. The tip leakage flow is highly unsteady, as evidenced by the variation in single PIV images. Figure 7 shows four PIV images taken at the same operating conditions and downstream location. All vector plots are for the same blade angles or blade positions, the trailing edge is 1.52^o ($S = 0.0296$) and 27.02^o ($S = 0.5259$) above the plane of measurement. Variation in the flow field can be readily observed. The position, strength, and core size of the vortex varies between images. The contours show changes in the measured out-of-plane vorticity.

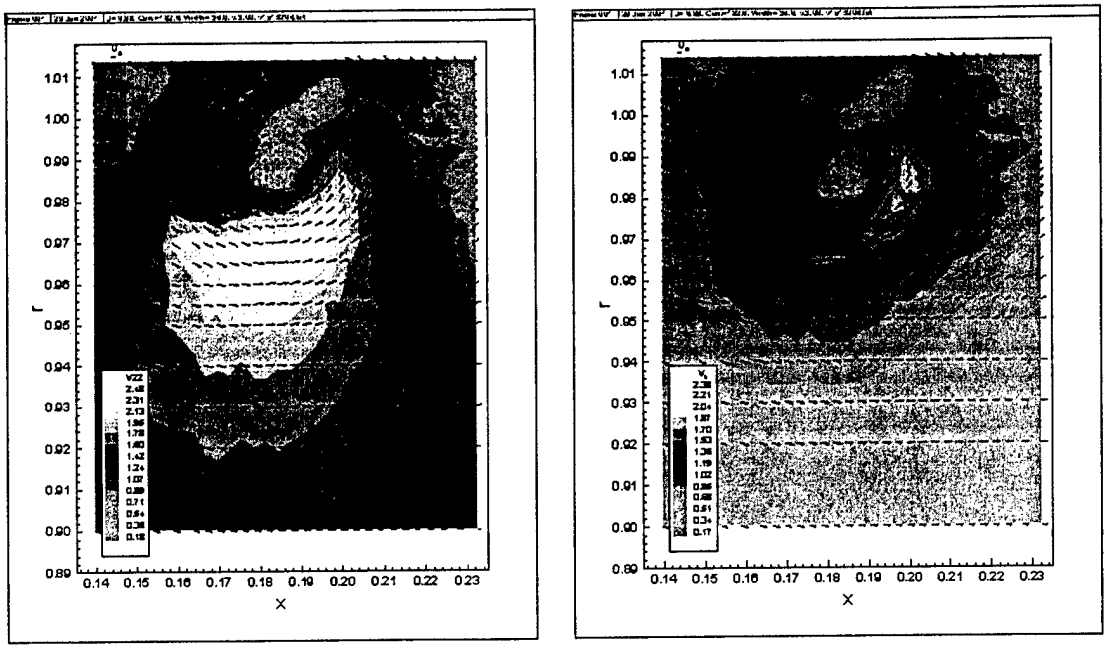

Figure 6: 2-component versus 3-component LDV measurements. These measurements were taken at 500 rpm, 45 psia, and S=0.0296. The 2-component LDV gives similar results to the simple-averaged PIV. The contour color corresponds to vector length. The 3-component measurements result in a more accurate mean core structure of the vortex. The vortex is not necessarily oriented with the horizontal plane. The 3-component LDV measurements allow a non-horizontal cut to be taken so that the vortex is perpendicular to the in-plane velocity measurements. r/R_P and x/R_P are shown.

Table 3. Comparison between simple-averaged PIV and center-averaged PIV vortex quantities.

S	Type of average	Radius, a (mm)	Circulation, Γ (m^2/s)	$-(\frac{\Gamma}{2\pi a})^2$ $(m/s)^2$	Average tangential velocity, V_t (m/s)	Maximum tangential velocity, $V_{t_{max}}$ (m/s)
0.0296	simple average	8.695	-0.7146	-171.1	13.16	18.01
0.0296	velocity centered average	8.511	-0.7026	-172.6	13.14	17.90
0.0296	vorticity centered average	8.630	-0.7034	-168.3	13.12	17.85
0.5259	simple average	12.62	-0.6193	-61.02	8.506	11.32
0.5259	velocity centered average	12.27	-0.6024	-61.06	8.440	11.12
0.5259	vorticity centered average	12.74	-0.5885	-54.03	8.060	10.56

Figure 11 shows histograms of the vortex-center location for S = 0.0296 and S = 0.5259. The location of the vortex core varied by ±1 mm and ±3 mm, respectively, or 11% and 26% of the vortex core radii. After identifying the position of the vortex, it is possible to shift the PIV images so that a centered-average can be computed. Table 3 shows three averages computed for 532 PIV images. The simple-average is just the non-shifted average of the PIV images. The velocity-centered average used the position of minimum velocity near the vortex core as the locus for the average, and the vorticity-centered average used the position of maximum vorticity near the vortex core. Figure 9 shows the averaged PIV images for these two blade values, S. For the case of S = 0.0296, the effect of vortex wandering is small, with changes in the core size of the centered-averages less than 2% compared to the simple-average. The wandering is greater for the case of $S = 0.5259$, with the differences approaching 3%. These results are consistent with the calculations of Straka and Farrell (1992). They computed the effect of vortex wandering on the resulting averaged flow field of a two-dimensional Burgers vortex and showed that the amplitude of vortex must wander by greater 50% of the core radius for the simple-average measurement to depart from the center-averaged measurement.

Figure 11 presents histograms of the core radius, a, the circulation around the viscous core, Γ, the average tangential speed, V_t, the maximum value for the tangential speed, $V_{t_{max}}$, and the quantity $-(\Gamma/2\pi a)^2$, for two blade angles. For S = 0.0296, the core radius ranges between 7.40 and 10.12 mm, the average circulation is between -0.82 and -0.66 m^2/s, and the average tangential velocities were between 12.82 and 14.96 m/s with the maximum tangential velocities between 16.66 and 21.01 m/s.

As discussed above, variation in the angle that the vortex axis makes with the PIV light-sheet can lead to variation in the measured quantities of the vortex. Consider a line vortex with radius a_0 that makes an angle of α with the PIV plane. The vortex core will be imaged as an ellipse with area $\pi a_0^2 \sec(\alpha)$. The measured average core diameter would then be larger than the actual core diameter by a factor of $(\sec(\alpha))^{1/2}$. A 10^o variation in the incidence angle will result in a 1% increase in the measured core size, and a 20^o inclination will result in a 3% variation. The actual angle of incidence is likely to be much less than $\pm 20^o$. Consequently, the observed variability in the instantaneous PIV quantities is not principally due to vortex wandering but is the result of true variations in strength and size of the vortex.

6 Development of the Tip-Leakage Vortex Flow Downstream of the Blade

The vortex core size and strength vary as the vortex flow moves downstream of the blade trailing edge. Figure 10 shows these quantities plotted as a function of S. Variation of these curves are relatively smooth, except for the region just downstream of the trailing edge where the leakage vortex is rolling up and may be interacting with a trailing edge vortex. For S > 0.2312 the variation is quite smooth. The radius of the core size increases as the blade moves up and away from the plane of measurement. The circulation shows a generally increasing trend as the trailing edge moves further out of the plane of measurement. The average tangential velocity and the maximum tangential velocity show a peak right when the trailing edge of the blade is in the plane of measurement ($S = 0$) and then decrease as the blade moves further away. Lastly, the quantity $(\Gamma/2\pi a)^2$ is largest near the trailing edge and is reduced farther downstream. These data can also be derived from the 3-dimensional LDV data, along with the axial velocity within the vortex core. We intend to compare the PIV and LDV results more closely.

7 Developed Tip-Leakage Vortex Cavitation

The cavitating vortex core was visualized by reducing pressure beyond inception, as shown in Figures 12 and 13. Visualization of the vortex shows that it is angled relative to the PIV plane by approximately 15^o in the upstream axial direction near the trailing edge and about 3^o upstream of the trailing edge. Surface cavitation can be observed in the gap region for the developed cavitation. High-speed video showed wandering of the vortex with a displacement that ranged from very little when the vortex was a along side of the blade (less then one-half the core width) to 100% of the observed vapor core diameter about 0.1524 m (6in) downstream. This is consistent with the wandering amplitude of the non-cavitating vortex. Downstream of that the vortex wanders more, probably due to the combining on the trailing edge vortex and general wake roll up. At this

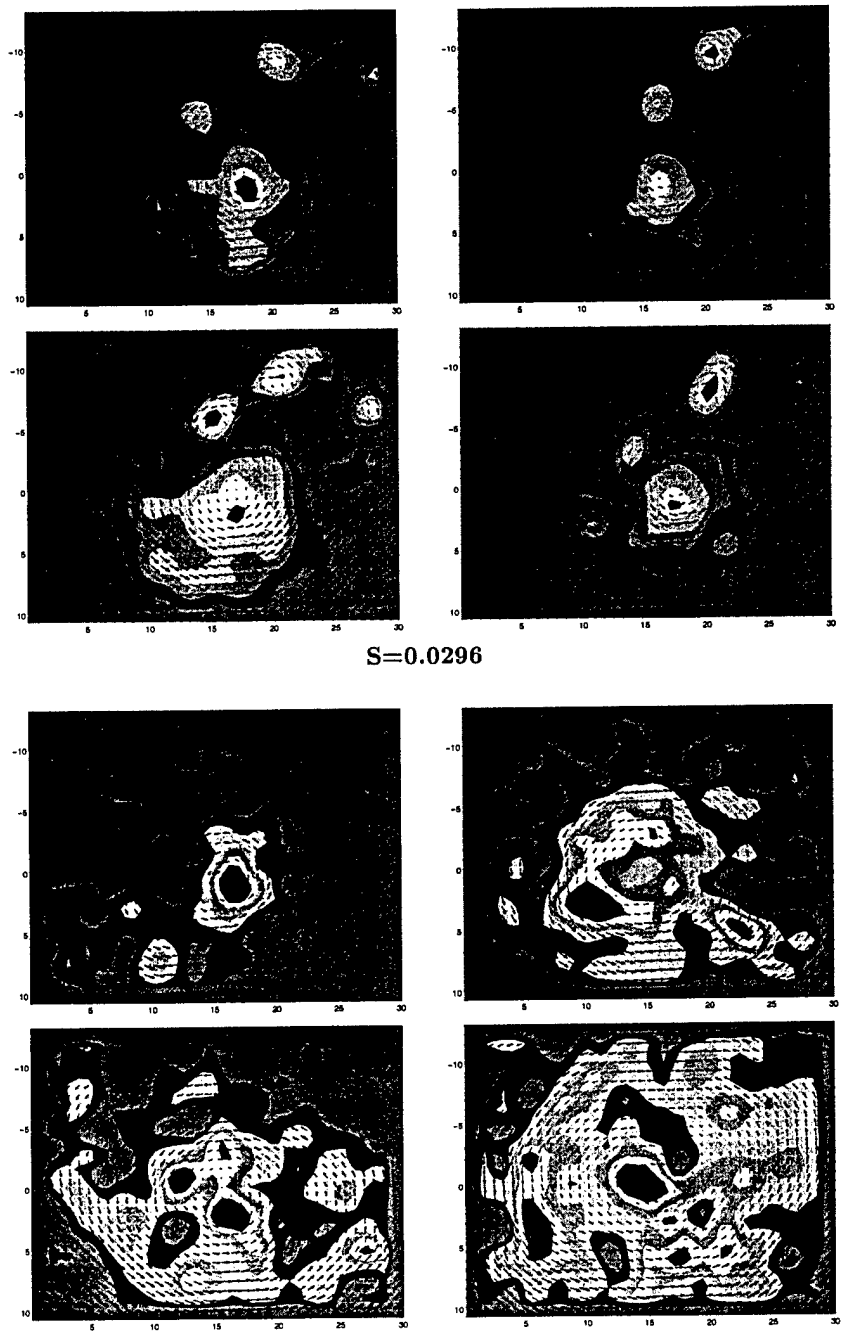

Figure 7: Four instantaneous PIV images taken at S=0.0296 and S=0.5259, 500 rpm, 45 psia. Velocity vectors are shown with contours of vorticity. The vortex center and vorticity changes with each image.

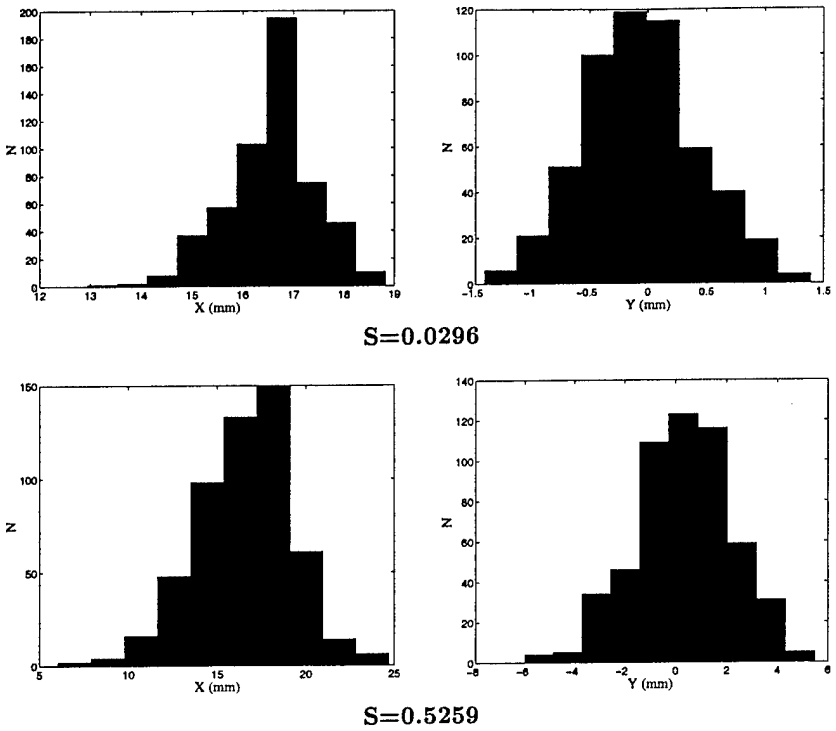

Figure 8: Histograms of the (X,Y) position of the vortex center showing the amount of wandering at S=0.0296 and S=0.5259, 500 rpm and 45 psia. The PIV measured the vortex core over a range of 5.36 (mm) in the x-direction and 3.06 (mm) in the y-direction for $S = 0.0296$. The wandering increases further from the blade.

point the vortex gets much more distorted and wanders up to 300% of the observed vapor core.

Arndt and Keller (1992) employed the principal of angular momentum conservation to show that the diameter of the vapor core of a developed cavitating Rankine vortex is smaller than the non-cavitating vortex core by a factor of $1/\sqrt{2}$. Here the non-cavitating core radius was measured to be 9 mm downstream of the trailing edge, and the measured vapor core had a radius of approximately 3 mm, or 0.3 times the original core radius. This is much lower than the expected value of $1/\sqrt{2} = 0.71$. Similar measurements of the cavitating to non-cavitating core ratio for tip vortex forming on a stationary elliptic hydrofoil yielded a ratio of 0.5 (Briançon-Marjollet and Merle, 1997).

Figure 13 shows a detail of the leakage vortex, where surface cavitation at the tip convects into the vortex. The flow direction can be observed along with the increase in cavitating vorticity, fed by the gap flow.

8 Conclusions

The tip-leakage vortex occurring on a ducted rotor was examined using both LDV and PIV. Preliminary analysis of the data indicates that the there is substantial variability in the instantaneous vortex quantities, such as the size of the viscous core and the strength of the vortex. Inception of discreet cavitation events will occur when nuclei are captured within the vortex, experience tension, and vaporously grow. Inception can occur when an unusually large nucleus is captured by the average vortex, and when an average nucleus is captured by an unusually strong vortex. We are presently conducting inception experiments to determine how variability of the vortex influences inception of discreet cavitation events. We will examine when and where discreet cavitation events occur, and attmpt to relate this to the measured two- and three-dimensional

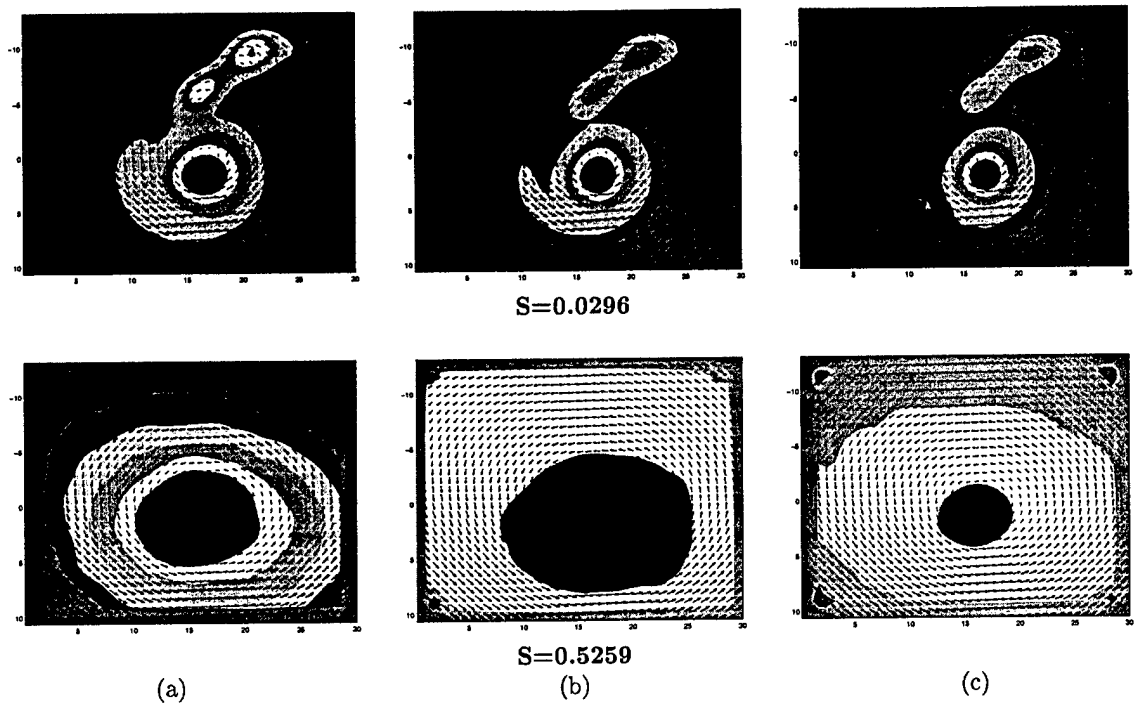

Figure 9: Averaged and centered-averaged velocity vectors and vorticity contours from 532 PIV images at 500 rpm, 45 psia, and S = 0.0296 and 0.5259. An average where the center of each vortex is in the same location is called 'centered-average'. The simple-averaged image shows a larger vortex core size and lower tangential velocities. Table 3 shows variations in vortex quantities between the two averaging methods.

flow quantities.

Acknowledgements

This work was sponsored by the Office of Naval Research, performed by the Carderock Division of the Naval Surface Warfare Center, Code 5400 and the University of Michigan under ONR contract N00014-99-1-0307.

References

Ardnt, E., A. and Keller, A. P. (1992). *Journal of Fluids Engineering.*, **114**, 430-438.

Boulon, O., Callanaere, M., Franc, J.-P., and Michel, J.-M. (1999). *Journal of Fluid Mechanics.*, **390**, 1-23.

Brennen, C.E. (1995). *Cavitation and bubble dynamics*, Oxford Univ. Press.

Briançon-Marjolet, L. and Merle, L. (1997). 21^{st} *Symposium on Naval Hydrodynamics.*, 851-864.

Brownell, W. F. (1962) *DTMB Report 1690*

Chesnakas, C. and Jessup, S. (1998). 22^{rd} *Symposium on Naval Hydrodynamics.*, 139-152.

Farrell, K. J. and Billet, M. L. (1994). *Journal of Fluids Engineering.*, **398**, 1-43.

Fruman, D., Dugué, C., Pauchet, A., Cerruti, P., and Briançon-Marjolet, L. (1992). 19^{th} *Symposium on Naval Hydrodynamics.*, 633-654.

Fruman, D.H., Pichon, T., and Cerruti, P. (1995). *Journal of Marine Science Technology.*, **1**, 13-23.

Gopalan, S., Liu, H., and Katz, J. (2000). 23^{rd} *Symposium on Naval Hydrodynamics.*, 177-187.

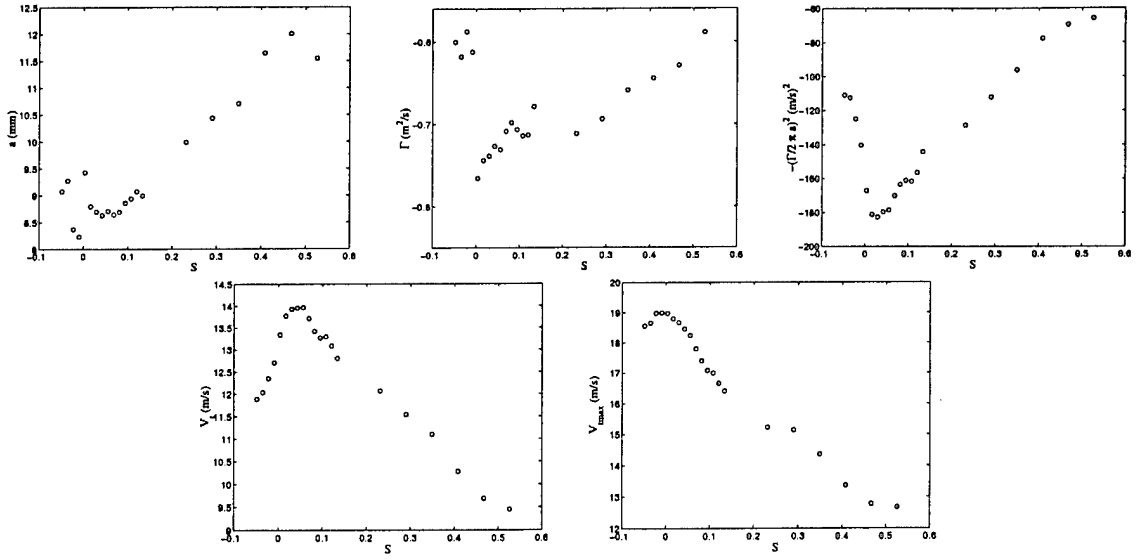

Figure 10: Distributions of radius (a), circulation (Γ), average tangential velocity (V_t), maximum tangential velocity ($V_{t_{max}}$), and the quantity $-(\Gamma/2\pi a)^2$ for 532 PIV images at various non-dimensional S locations at 500 rpm and 45 psia. S is the non-dimensional circumferential distance the trailing edge of the blade has traveled. It is non-dimensionalized by the chord-length.

Maines, B. H. and Arndt, R. E. A. (1997). *Journal of Fluids Engineering.*, **119**, 413-419.

McCormick, B. W. (1962). *ASME Journal of basic Engineering.*, Sept., 369-379

Pauchet, A. (1997). 21^{st} *Symposium on Naval Hydrodynamics.*, 865-881.

Straka, W. A. and Farrell, K. J. (1992). *Experiments in Fluids.*, **13**, 163-170.

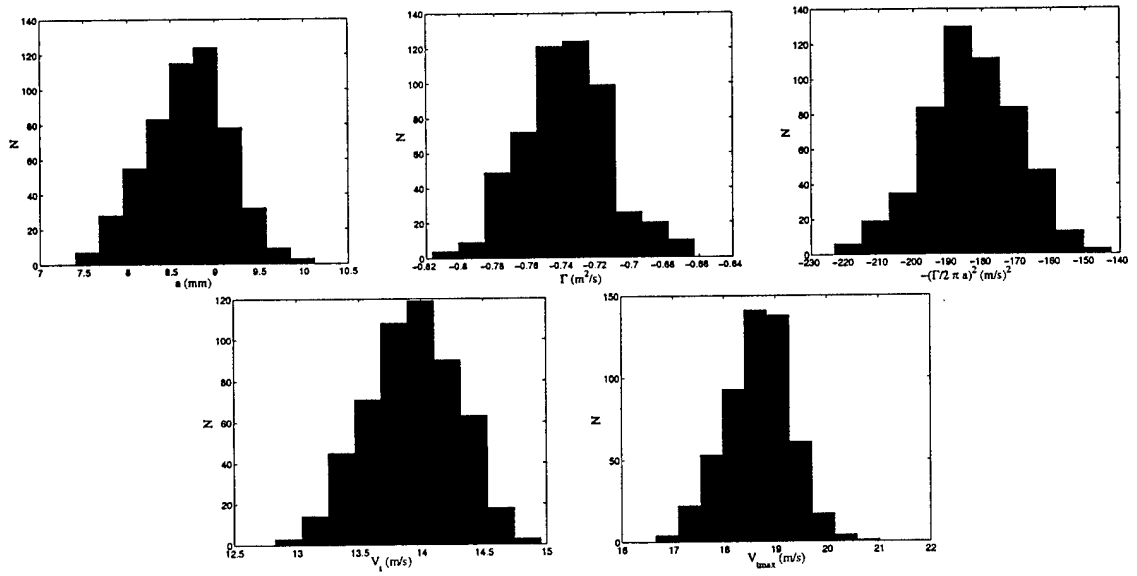

S=0.0296

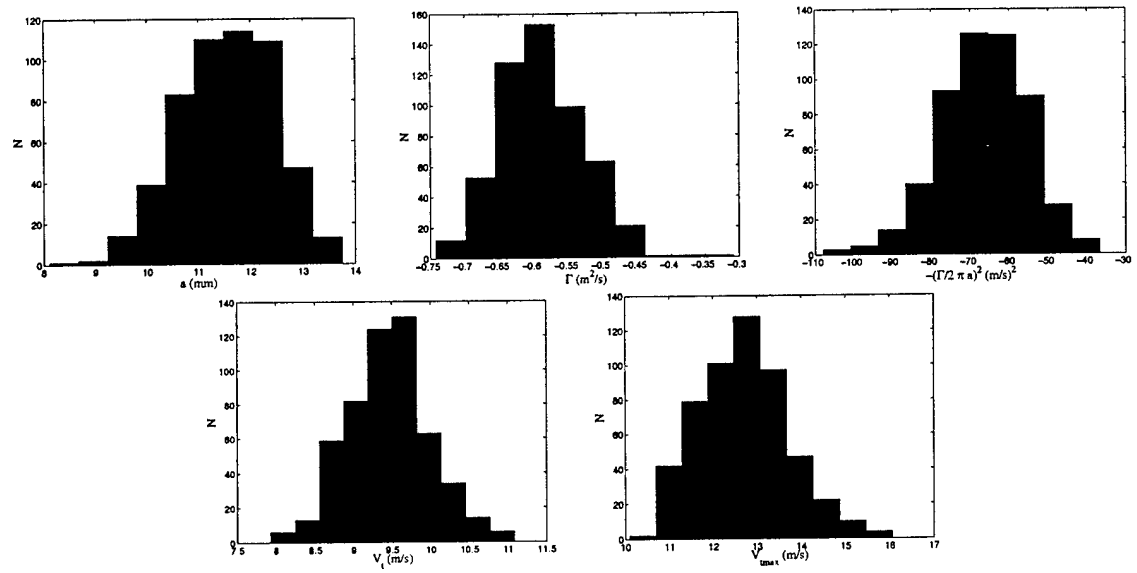

S=0.5259

Figure 11: Distributions of radius (R), circulation (Γ), average tangential velocity (V_t), maximum tangential velocity ($V_{t_{max}}$), and the quantity $-(\Gamma/2\pi a)^2$ for 532 PIV images for S=0.0296 and S=0.5259 at 500 rpm, 45 psia. Note the variation in vortex quantities for a single blade angle.

Figure 12: Photo of the cavitating vortex at 500 rpm and pressure at 25 psia. The cavitating vortex core is visualized by reducing the pressure beyond inception.

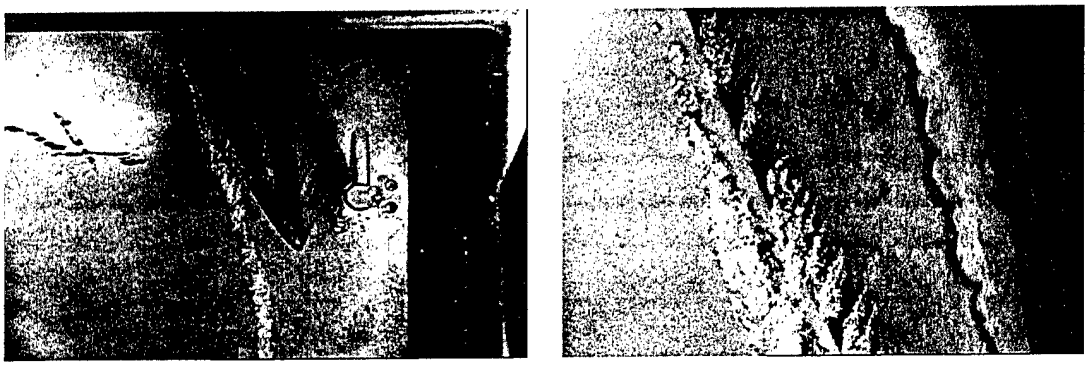

Figure 13: Photo of the cavitating vortex near the blade at 500 rpm and pressure at 18 psia with a close up of the surface cavitation. Note where the surface cavitation at the tip convects into the vortex.

Dynamics and Noise Emission of Laser Induced Cavitation Bubbles in a Vortical Flow Field

Ghanem F Oweis

Mechanical Engineering Department, University of Michigan, Ann Arbor, MI 48109

Jaehyug Choi

Mechanical Engineering Department, University of Michigan, Ann Arbor, MI 48109

Steven L Ceccio

Mechanical Engineering Department, University of Michigan, Ann Arbor, MI 48109

ABSTRACT

The sound produced by the collapse of discreet cavitation bubbles was examined. Laser-generated cavitation bubbles were produced in both a quiescent and a vortical flow. The sound produced by the collapse of the cavitation bubbles was recorded, and its spectral content was determined. It was found that the rise time of the sound pulse produced by the collapse of single, spherical cavitation bubbles in quiescent fluid exceeded that of the slew-rate of the hydrophone, which is consistent with previously published results. It was found that, as collapsing bubbles were deformed by the vortical flow, the acoustic impulse of the bubbles was reduced. Collapsing non-spherical bubbles often created a sound pulse with a rise time that exceeded that of the hydrophone slew-rate, although the acoustic impulse created by the bubbles was influenced largely by the degree to which the bubbles became non-spherical before collapse. The noise produced by the slow growth of cavitation bubbles in the vortex core was not detectable. These results have implications for the interpretation of hydrodynamic cavitation noise produced by vortex cavitation.

INTRODUCTION

The sound associated with the growth and collapse of single cavitation bubbles has been a topic of interest for some time [1-4]. Discreet cavitation events are often the source of significant cavitation noise in underwater flows and within turbo-machinery. Over time, researchers have undertaken to understand how cavitation bubbles create noise and how that noise can be scaled with changes in cavitation and Reynolds number.

A widely used scaling method for hydrodynamic cavitation noise was proposed by Fitzpatrick and Strasberg [5] in 1957. They used spherical bubble dynamics to analyze the volume growth and collapse of a single cavitation bubble in an infinite fluid. Fourier analysis of the volume acceleration was then used to determine the spectral content of the noise emitted by the bubble. A time scale of the problem is the Rayleigh collapse time, t_C,

$$t_C = 0.915 R_M \sqrt{\rho / \Delta P} \qquad (1)$$

where R_M is the maximum radius of the bubble (sometimes taken as the Equation.3 $|\Delta P\}$ is the pressure difference between the external fluid and the bubble contents, and ρ is the liquid density. With monopole sound generation, the acoustic pressure generated by the bubble will scale with the volume acceleration, an estimate of which can also be derived from Rayleigh's analysis. The sound pressure produced by the growth and collapse of the bubble is then given by

$$S(r,\omega) = \frac{\rho^2}{8\pi r^2} \left| \ddot{V}(\omega) \right|^2 \qquad (2)$$

where r is the distance between the bubble and the sound pressure measurement [6].

The Fitzpatrick and Strasberg model predicts that the sound spectrum generated by single bubble collapse should scale as $(\omega t_C)^4$ for $\omega t_C < 1$. The peak of the spectrum is near $\omega t_C = 1$, and higher frequencies will roll off as $(\omega t_C)^{-2}$. Mellen's [7] measurements of bubble cavitation noise spectra resulting from a bubble cloud formed at the end of a rotating rod exhibit theses spectral features and has been used to support the validity of this analysis. Corrections to this analysis have included the effect of liquid compressibility and the introduction of non-condensable gas within the cavity [8,9]. These processes tend to limit the predicted energy emitted at frequencies greater than $10 \cdot (\omega t_C)$.

If the external bubble pressure greatly exceeds the pressure of the non-condensable bubble contents at the time of the bubble maximum volume, the bubble wall velocity can approach the local liquid sound speed, leading to the formation of a pressure shock-wave during the rapid volume accelerations near the point of minimum bubble volume. Baiter [10] has shown that such a shock wave can exhibit a pressure pulse of the form

$$P_a(r,t) = P_S e^{-t/\theta} \qquad (3)$$

The peak pressure is $P_S(r) = f_1(r, R_M, R_m, P_G, \rho c^2)$, and the pulse width is $\theta(r) = f_2(r, R_M, R_m, P_G, \rho c^2)$. R_M, and R_m and maximum and minimum bubble radii, P_G, is the non-condensable gas pressure of the bubble at its maximum volume, and c is the liquid sound speed. The spectrum associated with the sound pulse

$$S(r,\omega) = \frac{(P_S\theta)^2}{1+(\omega\theta)^2} \qquad (4)$$

which is flat until the cut-off frequency $1/(\omega\theta)$. The cut-off frequency is strongly affected by the amount of non-condensable gas present in the collapsing cavity. The non-condensable gas may have existed within the original gas nucleus, and diffusion to or from the liquid may either increase or reduce the total mass of non-condensable gas, depending on the pressure/volume history of the bubble and saturation level of the surrounding liquid prior to bubble collapse.

Measurement of noise spectra from discreet hydrodynamic cavitation has been reported. Typically, the noise produced by traveling bubble cavitation has been examined [11-15]. The pressure pulse created by a collapsing cavitation bubble can be characterized by the acoustic impulse, I:

$$I = \int_\theta P_a dt \qquad (5)$$

where θ is the pulse width. However, shearing and fission of the bubble can significantly reduce the total emitted sound [16]. The presence of nearby bubbles can also lead to significantly reduced acoustic emission [17].

Measurements of the spectral content of discreet hydrodynamic cavitation events have not been consistent. Reverberations in confined flow facilities and the limitations of the fidelity and bandwidth of the measurement equipment can contaminate the measured spectrum. Much of the spectral data presented consists of the average spectra produced by many cavitation events. Beside the data reported by Mellen, there is little evidence that the spectral content of single cavitation bubble noise will scale as predicted by incompressible bubble dynamics. Spectra

measured from traveling bubble and vortex cavitation are not consistent [12-15]. Some spectra are reported to exhibit the features predicted by Fitzpatrick and Strasberg (i.e. low Mach number bubble collapse), while others are reported to be broadband. Moreover, the relative noise contribution due to the growth and collapse phases of hydrodynamic bubble cavitation are often considered comparable, although most researchers report experimental noise measurements principally from the bubble collapse. Further complications arise from the generally complex and non-spherical shape of hydrodynamic cavitation bubbles, the reverberant environment where experiments are conducted, and bandwidth limits of measurement equipment.

Capture of the true acoustic transients created by collapsing cavitation bubbles usually requires the construction of a high frequency response transducer, typically made from a thin film of polyvinylide fluoride (PVDF). The pressures measured with these devices has been compared to the optically measured volume change of the bubble, and it has been shown that, by far, the strongest noise is emitted when the bubble reaches a minima of volume [18,19]. Sound is produced as a shock wave that radiates away from the bubble, and the rise time of the shock wave is on the order of 5 nanoseconds, the maximum peak pressures on the order of hundreds of atmospheres near the bubble, and the pulse width is on the order of 10 to 100 ns. The collapse of non-spherical bubbles can produce less noise. Bubbles collapsing near a solid boundary can be deformed, and the lack of spherical focusing can significantly reduce the emitted noise [18]. The sharp rise time high pressures observed in these studies indicate that the spectrum of the emitted sound is dominated by the collapse processes and is, largely, broadband.

In the present work, we will measure the noise pulse and spectra associated with single cavitation bubble events using techniques that are often employed in the study of hydrodynamic cavitation. Bubbles will be produced in the vicinity of a low-pressure vortex core. We will

show that the noise emitted by the focused collapse of distorted bubbles is broadband and does not exhibit significant spectral content, even for highly distorted bubbles. The noise produced by highly distorted cavitation bubbles is still scaled by the dynamics of spherically collapsing bubbles. Lastly, we will show that the magnitude of the noise produced during bubble growth is significantly smaller that the noise produced upon collapse.

I. EXPERIMENT

Single cavitation bubbles were created in both a quiescent liquid and in a vortical flow. Figure 1a shows the schematic diagram of the quiescent cavitation bubble experiment. A small cubical Lucite water tank (205mm side) was created with an optical glass window (100 mm diameter) for the introduction of laser light. The infrared light pulse (1064 nm wavelength, ~10 nS pulse duration, 280 mJ/pulse, maximum) was produced by a Q-switched Nd:YAG laser (Spectra Physics PRO 250). Through a set of spherical lenses, the beam was expanded to a diameter of 100 mm and then focused to a waist within the tank. The cone angle was 19.4° in air. The space over the liquid in the tank could be evacuated, and the gas pressure was recorded with an Omega PX203 pressure transducer. Distilled water was placed within the tank. In order to increase the repeatability of bubble production, a small amount of drinking tap water was added to the tank. The tap water contained enough micron sized contaminants that led to the regular absorption of the laser light in the location of the beam waist and the production of a single cavitation bubble, although intermittent production of multiple bubbles was also observed. Variation in the static pressure above the tank and the energy of the light pulse resulted in variation of the maximum bubble volume and collapse time of the cavitation bubble.

Images of the bubble were observed with a Cooke Corporation "FlashCam" digital camera. This camera has an effective resolution of 752 by 240 pixels, and it is capable of recording up to

10 consecutive exposures on the same image frame, with varying integration times and delays between each exposure. A pulse delay generator (Stanford Research Systems model DG535) was used to trigger the camera at varying delays from the laser Q-switch pulse. These images were then recorded digitally. The acoustic center of a Brüel & Kjær type 8103 hydrophone was placed 30 mm from the location of the beam waist, and the resulting sound emission was conditioned with a Brüel & Kjær type 2635 charge amplifier and digitally acquired using a TekTronix storage oscilloscope. The A/D was 12-bit resolution, and the sampling rate was 2.5 million samples/second.

Figure 1b shows the setup for the creation of single cavitation bubbles in a vortical flow. The water tunnel has a circular contraction downstream of a series of flow management screens with area contraction ratio 6.4:1. The test section has a 22.9 cm (9 inch) diameter round inlet that is then faired into a rectangular test section with widely rounded corners. Four acrylic windows (93.9 cm by 10.0 cm viewing area) permit optical access to the test section flow. The flow in the test section can be operated at pressures from vapor pressure to approximately 200 kPa (30 Psia). The average velocity in the test section is variable up to 18 m/s (59.05 ft/s). A de-aeration system can be used to vary the dissolved gas content of the flow, and the inlet water is filtered to 1 microns.

A vortical flow was created using a cambered hydrofoil mounted to one window of the test section. The hydrofoil has a rectangular planform of 9.5 cm span and 16.8 cm chord, and the tip of the hydrofoil was truncated with sharp edges. The hydrofoil mount allows continuous changes of the incident flow angle. A series of tip and trailing edge vortices will be shed near the tip, and these vortices will merge to form a single vortex within one-half chord length downstream of the hydrofoil trailing edge. The tip vortex produced by the hydrofoil can be

visualized with developed cavitation, as shown in Figure 2. Measurements of the bubble/vortex interactions were conducted using a free-stream velocity of 10 m/s and a variety of pressures. The dissolved oxygen content was measured with an Orion Model 810 dissolved oxygen meter. In order to reduce the number of free-stream nuclei, the free-stream gas-content was reduced to below 1.5 ppm during the measurements.

Planar Particle Imaging Velocimetry (PIV) was used to measure the vortical flow field at a station 9.0 cm downstream of the trailing edge. A double-pulsed light sheet 9 mm thick was created perpendicular to the mean flow direction using two pulsed Nd:YAG lasers (Spectra Physics model Pro-250 Series). 15-micron average diameter silver coated glass spheres (from Potters Industries) were used to seed the flow. An acrylic prism was optically mounted to a window of the test-section for viewing of the light sheet with reduced optical distortion. The light sheet was imaged with a PIV image capture system produced by LaVision Inc. Double-pulsed images of the light sheet were acquired with a digital camera with 1280 x 1024 pixels. Optical distortion of the planar light sheet image was corrected through a calibration procedure that employed the imaging of a regular grid in the location of the light sheet plane. Velocity vectors were produced from the double-pulsed images using the LaVision image analysis software Davis6.0.4. Multi-pass processing with a final window size of 32 x 32 pixels was used with 12% window overlap in the final pass to produce 41 x 27 in plane velocity vectors at 0.62 mm spacing. Since the camera-imaging plane was not parallel to the light sheet and it had an angular shift of 45° with the horizontal direction, this velocity component was corrected by knowledge of the camera angle and the tunnel free stream velocity.

Optically stimulated vortex-cavitation bubbles were created at the vortex centerline. As the cavitation number was reduced, discreet cavitation events occurred in the vortex core due to the

capture of free-stream nuclei. This cavitation occurred at various locations along the vortex axis downstream of the location of vortex roll-up. However, at such lower air contents, the event rate of this cavitation was quite low (< 1 event per second). Vortex cavitation could then be stimulated by the introduction of a nucleus though a focused pulse of IR laser light near the axis of the vortex. By varying the free-stream pressure and laser energy, the initial size of the laser-induced bubble could be controlled. Images of the bubble's growth and collapse were captured with the pulse-synchronized digital camera after an appropriate delay, as described above. A small cast acrylic tank of water was placed in pool of water on the top window of the test section, and in this tank the hydrophone was mounted. This produced an acoustic path between the cavitation event and the hydrophone of relatively matched impedance, although acoustic impedance mismatches between the acrylic and the water led to some attenuation and internal reflections.

II. RESULTS- CAVITATION IN QUIESCENT FLUID

As discussed in the introduction, several researchers have examined in detail the noise emitted by single cavitation events in quiescent fluid. They have shown that the amplitude and frequency content of the noise emission often greatly exceeds the capabilities of standard high-frequency hydrophones. In the present work, we first recreated the basic elements of these experiments to characterize our process of bubble formation and noise measurement by examining spherical and near-spherical bubbles were created in the small tank. The effect of buoyancy can be characterized by the dimensionless quantity

$$\delta = \left(\frac{\rho g R_M}{\Delta P} \right)^{1/2} \qquad (6)$$

where g is the gravitational acceleration [19]. For sufficiently small values of δ, the effect of buoyancy can be neglected. Spherical bubbles corresponding to $\delta \approx 0.01$ were created to characterize the hydrophone's ability to record the noise pulse produced by a single vaporous cavitation event.

Figure 3a shows multiple images of a near spherical bubble created with a laser light pulse. The hydrophone acoustic pressure signal produced by the collapse of the spherical bubble is shown in Figure 3b. Two distinct sound pulses are detected. The first occurs during the rapid growth of the bubble volume when the bubble is created. Between the pulses, a slow reduction and increase in pressure is seen that corresponds to the relatively slow volume acceleration around the point of maximum bubble volume. The second pulse corresponds to the first collapse of the bubble. Figure 3c shows a time-expanded pressure trace recorded for the collapse of the bubble. The response is that of a single-degree-of-freedom linear oscillator. Also plotted is the response of a single-degree-of-freedom oscillator excited with a narrow pulse where the natural frequency and damping of the oscillator was chosen to best fit the measured voltage trace. The natural frequency of the oscillator, ϖ_n, was calculated to be 105 kHz, and the damping coefficient, ζ, was 0.18. The natural frequency is in good agreement with the specifications of the hydrophone, which reported a resonance frequency of nearly 109 kHz. Variation in laser input power changed the maximum bubble volume and the corresponding maximum pulse amplitude, but the pulse response of the hydrophone did not vary. This was also true for bubbles undergoing non-spherical collapse as well. Rebounding bubbles and bubbles collapsing near a wall could sometimes produce two discernable pulses, due to bubble fission or the interaction of

jet impingement with the wall. But, the temporal response of the hydrophone was always that of a single-degree-of-freedom oscillator responding to an impulsive pressure input.

The measurement illustrates that the high-frequency limit of the measured sound spectrum is limited by the hydrophone response, even though the hydrophone would be considered "broadband" relative to other commercially available hydrophones. The pressure pulse created by the bubble may be approximated as $P_a(r,t) = P_S e^{-t/\theta}$ as discussed above. Pulse widths measured with optical and piezoelectric transducers are on the order of 10 to 100 ns [18,19]. An oscillator will respond to such a pulse with an under-damped response like that of Figure 3c. The peak amplitude of the response will be proportional to P_S, and the initial pulse width will be proportional to $1/\varpi_n$, the natural frequency of the hydrophone, if $1/\varpi_n >> \theta$. The measured pulse widths were typically 10 ± 2 μs $\approx 1/\varpi_n$, which is consistent with the reported hydrophone natural frequency.

The actual acoustic impulse will be approximately $I(r_H) \approx P_S(r_H)\theta(r_H)$ at the location of the hydrophone, r_H. The *measured* acoustic impulse, I_m, will scale as

$$I_m(r_H) \approx \frac{P_S(r_H)}{\varpi_n}\theta(r_H)\varpi_n \approx P_S(r_H)\theta(r_H) \quad (7)$$

based on the dynamic impulse response function of the hydrophone. However, the measured peak pressure and the pulse duration will be approximated by $P_S(r_H)\theta(r_H)\varpi_n$ and $1/\varpi_n$, respectively. The maximum bubble volume accelerations achieved and the resulting amplitude and time-scale of the emitted pressure wave is affected by the amount of non-condensable gas in the cavity, the collapsing pressure, and the topology of the collapsing bubble.

A scaling for the acoustic impulse can be derived from on spherical bubble dynamics and energy conservation [10]. However, for highly deformed bubbles, it may be more appropriate to scale the impulse based on the initial energy of the collapsing bubble, E_M,

$$E_M = \tfrac{4}{3}\pi R_M^3 \Delta P \qquad (8)$$

The energy radiated away from the bubble after the collapse and rebound, E_R, is given by

$$E_R(r) = \eta_R \frac{4\pi r^2}{\rho c}\int_0^\infty P_a^2 dt \qquad (9)$$

where η_R is the proportion of mechanical potential energy that is converted into acoustic energy. Vogel and Lauterborn [17] have shown that up to 90% of a bubble's mechanical energy can be converted to acoustic energy during the first collapse of spherical laser-produced cavitation bubbles, but the percentage can be reduced substantially if the collapsing bubble is non-spherical.

The measured peak shock pressure, P_S, is expected to scale with the maximum potential energy:

$$P_S \sim \frac{1}{2r_H}\left(\frac{\rho c E_R}{\pi\theta}\right)^{1/2} \sim \frac{1}{2r_H}\left(\frac{\eta_R \rho c E_M}{\pi\theta}\right)^{1/2} \qquad (10)$$

The acoustic impulse would then scale as

$$I_m(r_H) \sim \frac{1}{2r_H}\left(\frac{\eta_R \rho c E_M \theta}{\pi}\right)^{1/2} \sim \frac{1}{r_H}\left(\tfrac{1}{3}\eta_R \rho c\, \Delta P\, R_M^3 \theta\right)^{1/2} \qquad (11)$$

The functional relationship between θ and the other parameters of the flow are not straightforward, especially in the case of non-spherical collapse. The amount of non-condensable gas within the laser-produced bubble will vary due to variation in the process of bubble creation. Moreover, the amount of non-condensable gas at collapse will increase with increased maximum bubble volume, due to gas diffusion, and the minimum bubble volume and shape during the last phases of collapse will also vary. Consequently, variability of the measured impulse was observed given nominally constant laser-energy pulse input. However, the relationship between the impulse and the maximum bubble volume can be discerned.

III. RESULTS- VORTEX CAVITATION

Next, the growth and collapse of non-spherical hydrodynamic cavitation is considered. Cavitation bubbles were produced in the vicinity of a strong line vortex. The free-stream velocity was fixed at 10 m/s. Figure 4a shows a vector map of the average planar vortical flow field measure perpendicular to the vortex axis produced after averaging 100 instantaneous flow fields. Figure 4b plots the average tangential velocity, $u_\theta(r)$, as a function of the distance from the vortex center, r, along with a fitted curve for a Gaussian vortex:

$$u_\theta(r) = \frac{\Gamma_O}{2\pi r}(1 - e^{-\alpha(r/r_C)^2}) \qquad (12)$$

Here, $\alpha \approx 1.255$ which make r_C the "core radius" defined as the radius where the tangential velocity is maximum:

$$u_\theta(r_C) = \beta \frac{\Gamma_O}{2\pi r_C} \qquad (13)$$

where $\beta = 0.715$. For the measured vortex, the fitted core radius was 5.6 mm and the strength was 0.290 m^2/sec. Examination of the instantaneous images indicated that the vortex core did not wander significantly. The amplitude of wandering was consistently less than 15% of the core radius. Consequently, no correction for vortex wandering was needed [21].

The pressure depression due to the vortex is given by

$$P(r) - P_\infty = \int_\infty^0 -\frac{\rho {u_\theta}^2(r)}{r} dr$$

$$= -\rho\left(\frac{\Gamma_O}{2\pi r_C}\right)^2 \left(\frac{1}{2(r/r_C)^2}\right) \times \begin{bmatrix} -1 + 2e^{-\alpha(r/r_C)^2} - e^{-2\alpha(r/r_C)^2} \\ -2\alpha(r/r_C)^2 Ei(\alpha(r/r_C)^2 \\ +2\alpha(r/r_C)^2 Ei(2\alpha(r/r_C)^2 \end{bmatrix} \qquad (14)$$

where *Ei(x)* is the exponential integral function. The calculated radial pressure distribution for the vortex is also shown in Figure 4b. Here we are assuming that $\partial u_z / \partial r \approx 0$, where z corresponds to the direction along the vortex axis. Time exposed images of these bubbles in the vortex core indicate an axial velocity within 95% of the free-stream speed. The pressure at the axis of the vortex, $r = 0$, is given by

$$P_C = P_\infty - \eta\rho\left(\frac{\Gamma_O}{2\pi r_C}\right)^2 \qquad (15)$$

where $\eta = 0.870$.

Bubbles captured by the vortex can cavitate if the core pressure is at or below vapor pressure. The free-stream cavitation number is defined as $\sigma_\infty = (P_\infty - P_V)/\frac{1}{2}\rho U_\infty^2$, where U_∞ is the free-stream velocity. Captured bubbles can grow if $P_C \le P_V$, making the cavitation number at inception, $\sigma_{\infty,i}$,

$$\sigma_{\infty,i} \le \frac{\eta}{2}\left(\frac{\Gamma_O}{\pi r_C U_\infty}\right)^2 \qquad (16)$$

For the measured vortex, this corresponds to a free-stream cavitation number of 1.18.

Before creating bubbles within the vortex, near-spherical bubbles were created in the test section but without any flow. Figure 5a shows ten superimposed images of the laser produced bubble taken with a time interval $\Delta t = 40$ μs, and Figure 5b shows the resulting acoustic pulse. The test-section static pressure was 31.1 kPa. Again, when the laser pulse initiates the bubble, an acoustic pulse is created. The bubble passes through its maximum volume and collapses, creating a second pulse of sound. The sound pulse created upon collapse is still limited by the response of the hydrophone. Numerous bubbles were created with fixed static pressure. The maximum size of the bubbles varied with the amount of laser-light energy deposited in the liquid. The laser pulse energy could be varied manually, but the actual amount of light absorbed by the liquid varied with the size and density of small particulates that were present in the focal

volume of the laser during the pulse. This is the principal cause for the variability of the laser-induced bubbles.

The acoustic pulse created during the collapse of the bubble was recorded, and the acoustic impulse was calculated by time integration of the pressure pulse using the trapezoidal rule. The maximum bubble diameter was recorded with the digital camera. Figure 5c shows the variation of the acoustic impulse with the maximum bubble radius. While there is significant scatter, the data indicate that the impulse increases with the bubble volume, as expected. The spectrum analyzer was triggered to capture the noise signal produced by the collapse, although the residual echo from the initiation pulse was also present. To calculate the impulse, the average reverberant pattern was subtracted from the individual noise traces, and then the collapse pulse was identified and measured. This reverberant pattern from the bubble initiation pulse was highly repeatable when the bubble and hydrophone locations were fixed.

Figures 6, 7, and 8 present similar series of data for bubbles induced in the center of the vortex. Bubbles were created with three free-stream cavitation numbers: σ_∞ = 2.15, 1.73, and 1.49. With σ_∞ = 2.15, the bubbles collapse immediately after they are created, with σ_∞ = 1.73, the bubbles slowly collapse after growing along the vortex axis, and with σ_∞ = 1.49, the bubbles do not collapse but continue to grow along the axis.

The normalized acoustic impulse, $\hat{I}$, is defined as:

$$\hat{I} = I \frac{r_H}{\left(\frac{1}{3}\eta_R \rho c \, \Delta P \, R_M^3 \theta\right)^{1/2}} \qquad (17)$$

While the values of η_R and θ are unknown, the pulse width, θ, is expected to be on the order of 10 ns, for the case of spherical collapse [18,19]. The energy conversion efficiency, η_R, can vary with the collapse geometry of the bubble [18], but is expected to be > 60% for the bubbles under consideration. Figure 9 shows a plot of the normalized $\hat{I}$ against the bubble maximum radius with $\eta_R = 1$ and $\theta = 10$ ns for all the cases studied. The normalized acoustic impulse of bubbles imploding in quiescent fluid as well as bubbles that are not greatly deformed by the vortex field ($\sigma_\infty = 2.82$ and $\sigma_\infty = 2.15$) are independent of the bubble maximum radius, as expected from a proper scaling. The deformed bubbles ($\sigma_\infty = 1.73$) have a normalized impulse that is clearly lower than the spherical and less deformed bubbles. If it is assumed here that the collapse pressure pulse width does not change with the bubble collapse geometry. The results then imply that highly deformed bubbles are less efficient (have lower η_R) in converting their mechanical energy into radiated acoustic pressure in comparison to the slightly deformed and spherically imploding bubbles. Still in all of these highly deformed as well as spherical bubbles, resolution of the collapse pressure pulse is limited by the hydrophone response. The measured bubble collapse time (time from maximum volume to minimum volume) relative to the Rayleigh collapse is plotted in figure 10. This figure shows that highly deformed bubbles (($\sigma_\infty = 1.73$) have a longer collapse time than the more acoustic-efficient spherical bubbles, but the collapse time is on the same order.

A second case was considered where the bubbles did not collapse but continued to grow at $\sigma_\infty = 1.19$, and this is shown in figure 11. Here, the laser energy was greatly reduced, created only a small bubble that grew slowly under the influence of the low-pressure in the vortex core. In this case, the nucleus grew slowly and no noise was detectable. The magnitude of the volume acceleration during the natural bubble growth is much smaller that the acceleration during the

last stages of bubble collapse. As the bubble grows under the influence of the low vortex core pressure, $\dot{R} \sim \sqrt{-\Delta P/\rho}$, and $\ddot{R} \sim 0$. Consequently, the minimal amount of noise produced during the slow process of bubble growth was not detectable over the background noise created by the water tunnel flow.

Lastly, the pressure spectra recorded by the hydrophone for many bubble collapses was collected for the cases described above. The sound traces for 1000 events were collected. These are shown in figure 12. These spectra do not include the noise pulse produced by the initial bubble growth, but do include some of the reverberation resulting from bubble production. The case of the small bubble production (sb) corresponds to the background noise of the tunnel operating at 10 m/s. The spectral features below 30 kHz correspond to reverberant modes of the facility. As the impulse of the bubbles increases, the energy in the reverberations increases as well. Also, the energy in frequencies greater than 30 kHz increases, but the spectra is flat until 100 kHz. This is consistent with the input of a sharp impulse into the bandwidth-limited hydrophone.

IV. DISCUSSION AND CONCLUSIONS

Acoustic transients by discreet hydrodynamic cavitation events were examined in both a quiescent and a vortical flow, and the following conclusions were found:

The hydrophone used was not capable of resolving the dynamics of the pressure pulse produced upon the collapse of a spherical cavitation bubble.

The acoustic impulse produced by a collapsing bubble scales with the collapse pressure and the maximum volume, even for non-spherical collapse. The noise pulse produced by

deformed collapsing bubbles is often sufficiently narrow to be unresolved by the hydrophone.

The normalized impulse created by the collapse of spherical bubbles represents the most efficient collapse, converting potential mechanical energy into acoustic energy. Deformed bubbles collapse with less transfer efficiency.

The noise produced by the natural bubble growth in the vortex is not measurable.

Vortex cavitation occurs when naturally occurring nuclei are captured by a concentrated vortex, and they grow and collapse. The results of this study suggest that significant noise is created only when the bubbles collapse, even if they are highly distorted. The noise produced is broadband, with a high-frequency cut-off beyond the bandwidth of most conventional hydrophones. However, the impulse created by the collapsing bubbles can be scaled with spherical bubble dynamics. Such scaling will provide the upper bound on the noise that a bubble of a given maximum volume can create when collapsing under a given pressure difference.

Finally, an unsteady pressure in the vortex core is required for a single nucleus to experience both rapid growth and collapse. The vortical flow employed in the present study is steady, and natural cavitation occurred only when the core pressure dropped below vapor pressure. At this point, captured nuclei continued to grow and ultimately filled the vortex core as the bubble convected downstream. The case of growth without collapse can be contrasted with cavitation accompanying more complicated vortical flows. In these flows variation in the local mean pressure, vortex-vortex interactions, and other flow unsteadiness can result in rapid growth and collapse of bubbles in the vortex core. Such cavitation occurs in turbulent shear flows and in the wake vortex system of complex turbo-machinery. However, the results of this study suggest

that spherical bubble dynamics can be used to scale the upper bound of the noise impulse produced by discreet cavitation events, even when the bubbles are quite deformed.

ACKNOWLEDGMENTS

This work was supported by a grant from the Office of Naval Research under contract number N00014-99-1-0307, Dr. K.-H. Kim, technical monitor.

REFERENCES

1Rayleigh, L. 1917, 'On the pressure developed in a liquid during the collapse of a spherical cavity', *Phil. Mag.*, **34**, 94.

[2]Coles, R. 1948 *Underwater Explosions*, Princeton University Press

[3]Harrison, M. 1952 'An experimental study of single bubble cavitation noise', *D.T.M.B. Rep. No.815 DTNSRDC.* Washington D.C.

[4]Knapp, R. T. and Hollander, A. 1948 'Laboratory investigations of the mechanism of cavitation', *Trans. A.S.M.E.*, **70**, 419

[5]Fitzpatrick, H. M. and Strasberg, M. 1956 'Hydrodynamic sources of sound' *Proc. 1st Symp. on Naval Hydro.*, Washington D.C.

[6]William K. Blake 1986 'Mechanics of Flow-Induced Sound and Vibration', *Academic Press Inc.*, **2**

[7]Mellen R. H. 1954 'Ultrasonic Spectrum of cavitation noise in water', *J. Acoust. Soc. Am.*, **26**, 356-360

[8]Gilmore, F. R. 1952, 'The growth and collapse of a spherical bubble in a viscous compressible liquid', *Hydrodynamics Laboratory Rep.* 26-4. California Institute of Technology.

[9]Noltingk B. E and Neppiras E. A. 1950 'Cavitation produced by ultrasonics' *Proc. Phys. Soc.* **63**(B), 674-685

[10]Baiter, H. J., 1974, 'Aspects of Cavitation Noise', *Proc. of the Symp. on High Powered Propulsion of Ships*, Wageningen, The Netherlands

[11]Blake, W. K. Wolpert, M. J. and Geib, F. E. 1977, 'Cavitation noise and inception as influenced by boundary-layer development on a hydrofoil', *J. Fluid Mech.* **80**(4), 617-640

[12]Hamilton, M. F. Thompson, D. E. and Billet, M. L. 1986, 'Experimental study of traveling bubble cavitation noise', *J. of Fluids Engineering, Transactions of the ASME*, **108**(2), 241-247

[13]Ceccio, S. L. and Brennen , C.E. 1991, 'Observation of the dynamics and acoustics of traveling bubble cavitation', *J. Fluid Mech.*, **233**, 633-660

[14]Kumar and Brennen, C. E. 1993, 'A study of pressure pulse generated by traveling bubble cavitation', *J. Fluid Mech.*, **255**, 541-564

[15]Li, C. I. and Ceccio, S. L. 1996, 'Interaction of single traveling bubbles with the boundary layer and attached cavitation' *J. Fluid Mech.*, **322**, 329-353

[16]Brennen, C. E. 2002, 'Fission of Collapsing Cavitation Bubbles', *J. Fluid Mech.*, **472**, 153-166

[17]Arakeri, V. H. and Shanmuganathan, V. 1985, 'On the evidence of the effect of bubble interference on cavitation noise' *J. Fluid Mech.*, **159**, 131-150

[18]Vogel, A. and Lauterborn, W. 1988 'Acoustic transient generation by laser-produced cavitation bubbles near solid boundaries' *J. Acoustic Soc. Am.*, **84**(2), 719-731.

[19]Matula, T. J., Hallaj, I. M., Cleveland, R. O., Crum, L. A., Moss, W. C., Roy, R. A. 1998 'The acoustic emissions from single-bubble sonoluminescence' *J. Acoustic Soc. Am.*, **103**(3), 1377-1382.

[20]Blake. J.R. and Gibson D.C. 1987 'Cavitation bubbles near boundaries' *Ann. Rev. Fluid Mech.* **19**, 99-123.

[21]Boulon, O., Callenaere, M., Franc, J.-P. , and Michel, J.-M. 1999 'An experimental insight into the effect of confinement on tip vortex cavitation of an elliptical hydrofoil' *J. Fluid Mech.* Vol. **390**, 1- 24.

FIGURE CAPTIONS

Figure 1: (a) Schematic diagram of the quiescent cavitation bubble experiment; (b) the bubble-vortex interaction experiment. A single laser pulse is used to create a cavitation bubble in the bulk of the fluid. Images of the bubble are captured with a multi-exposure digital camera, and the acoustic emission of the bubble is captured with a hydrophone.

Figure 2: Photograph of the hydrofoil in the water tunnel test section with developed tip-vortex cavitation with U_∞ = 10 m/s, and σ_∞ = 1.4. Flow is from left to right

Figure 3: (a) Five superposed exposures of a laser produced spherical cavitation bubble taken every 6 μs in a quiescent water container; (b) the resulting acoustic pressure trace recorded from the hydrophone; (c) the expanded hydrophone pressure trace produced upon bubble collapse (solid line) along with the second-order response of a SDOF oscillator to a Dirac-delta input with system ϖ_n = 105 kHz and damping ratio, ζ=0.18 (dashed line).

Figure 4: (a) The average vector map of the flow perpendicular to the vortex axis 90 mm downstream of the tailing edge for U_∞= 10 m/s; (b) the measured tangential velocity, $u_\theta(r)$,

along with the velocity distribution for the Gaussian vortex with r_c = 5.6 mm and Γ_o = 0.290 m^2/s and the resulting calculated pressure depression, $P(r) - P_\infty$.

Figure 5: (a) Ten images of a laser produced bubble taken 40 μs apart in the water tunnel test section without flow with P_∞ = 31 kPa; image dimensions (V 23.1 x H 31.9 mm); (b) the pressure-time trace recorded by the hydrophone; (c) the acoustic impulse created during bubble collapse versus the maximum bubble radius.

Figure 6: (a) Ten exposures of a laser produced bubble created in the vortex taken 54 μs apart with σ_∞ = 2.15, U_∞=10m/s; the bright region on the right results from pixel saturation from the original laser pulse; image dimensions (V 15.9 x H 21.0 mm); (b) the pressure-time trace recorded by the hydrophone; (c) the acoustic impulse created during bubble collapse versus the normalized maximum bubble radius (normalized by the vortex core radius).

Figure 7: (a)Ten exposures of a laser produced bubble created in the vortex taken 94 μs apart with σ_∞ = 1.73, U_∞=10m/s; the bright region on the right results from pixel saturation from the original laser pulse; image dimensions (V 15.9 x H 21.0 mm); (b) the pressure-time trace recorded by the hydrophone; (c) the acoustic impulse created during bubble collapse versus the normalized maximum bubble radius (normalized by the vortex core radius).

Figure 8: (a) Ten exposures (last two exposures outside the frame) of a laser produced bubble created in the vortex taken 154 μs apart with σ_∞ = 1.49, U_∞=10m/s; the bright region on the right results from pixel saturation from the original laser pulse; image dimensions (V 15.9 x H

21.0 mm); (b) the pressure-time trace recorded by the hydrophone. At this cavitation number, the bubble continues to grow along the vortex axis after initiation with the laser.

Figure 9: The dimensionless acoustic impulse, $\hat{I} = I.r_H / \left(\frac{1}{3}\eta_R \rho c \, \Delta P \, R_M^3 \theta\right)^{1/2}$, versus the dimensionless maximum bubble radius, $\hat{R}_M = R_M / r_C$, for P_∞= 10 kPa without flow (·), P_∞ = 31 kPa without flow (*), σ_∞ = 2.82 (+), σ_∞ = 2.15 (o), and σ_∞ = 1.73 (<). For this plot the acoustic conversion efficiency η_R was chosen to be 100%, and the collapse pulse width θ 10 nanoseconds.

Figure 10: The dimensionless collapse time $t_c/T_{Rayleigh}$ versus the dimensionless maximum radius, $\hat{R}_M = R_M / r_C$, for P_∞= 10 kPa without flow (·), P_∞= 31 kPa without flow (*), σ_∞ = 2.82 (+), σ_∞ = 2.15 (o), and σ_∞ = 1.73 (<).

Figure 11: (a) Ten exposures of a bubble created by a low energy laser pulse in the vortex taken 300 μs apart with σ_∞ = 1.19; the initial nucleus is small and not visualized in the image; flow is from right to left; (b) the pressure-time series recorded by the hydrophone, which is equivalent to the baseline hydrophone signal before inception.

Figure 12: Average power spectral density of the hydrophone signal for the 5 different cases corresponding to macroscopic bubbles created without test-section flow, and in the vortex for σ_∞ = 2.8, 1.70. 1.28 The spectrum of the noise recorded when the microscopic bubbles (sb) were created at σ_∞ = 1.19 is also included, and this is equivalent to the baseline spectrum without cavitation. The spectrum analyzer was triggered to analyze the noise signal produced due to the bubble collapse only, and the spectra from 1000 acoustic events were averaged.

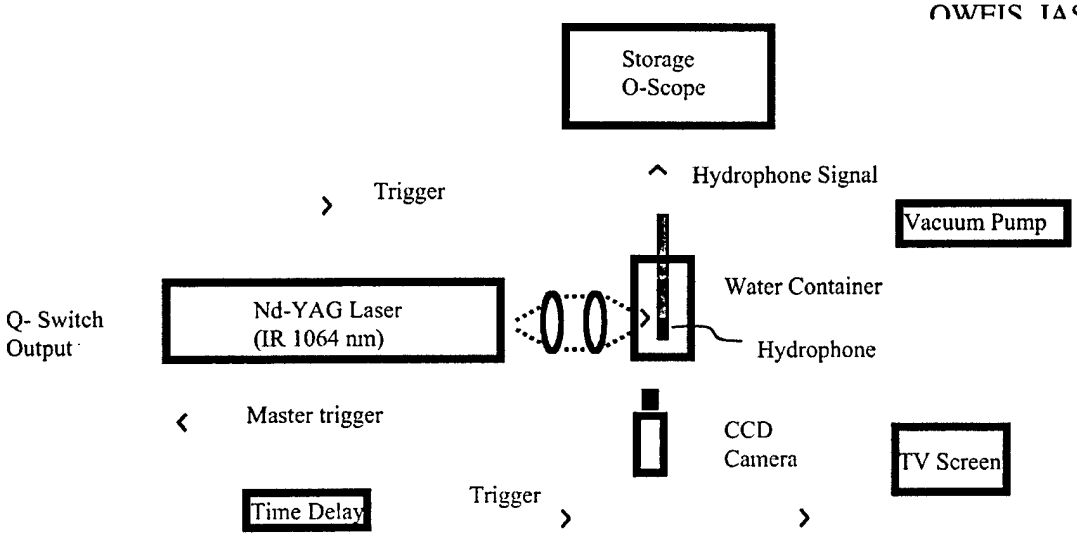

(a)

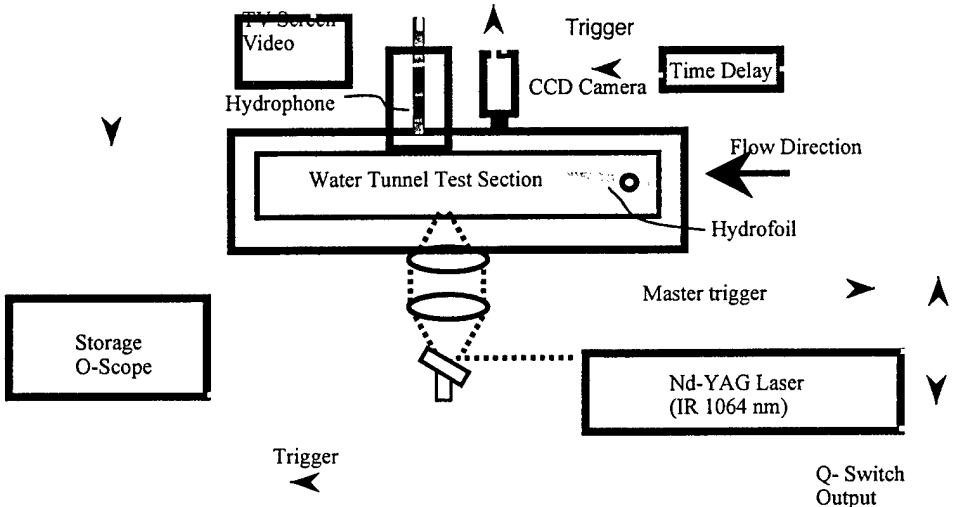

(b)

Figure 1: (a) Schematic diagram of the quiescent cavitation bubble experiment; (b) the bubble-vortex interaction experiment. A single laser pulse is used to create a cavitation bubble in the bulk of the fluid. Images of the bubble are captured with a multi-exposure digital camera, and the acoustic emission of the bubble is captured with a hydrophone.

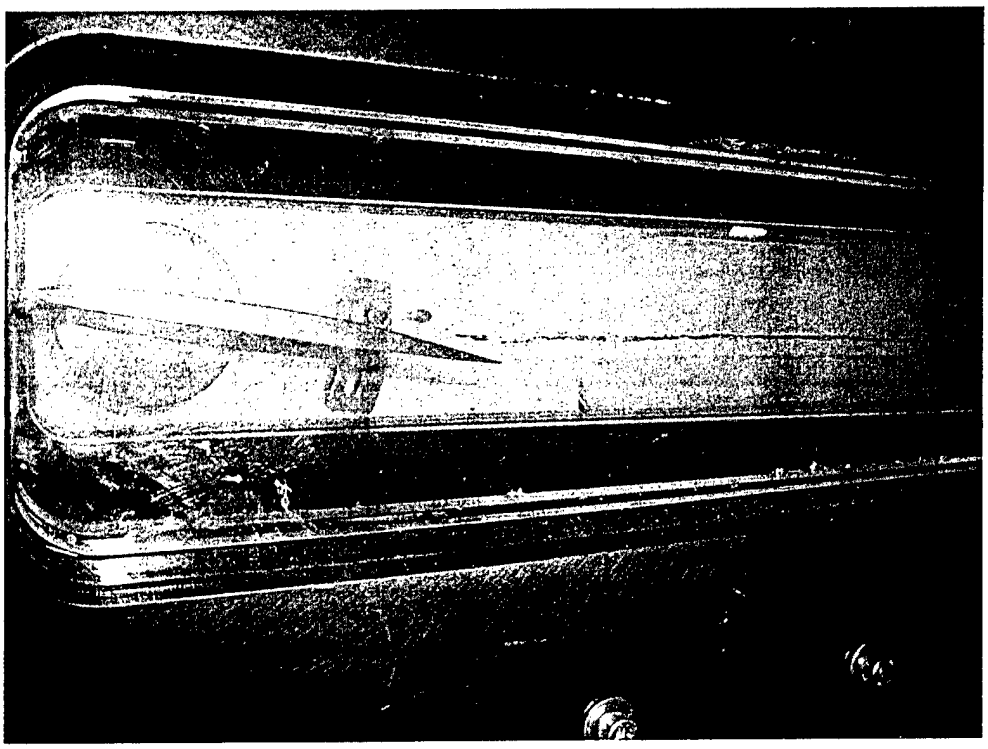

Figure 2: Photograph of the hydrofoil in the water tunnel test section with developed tip-vortex cavitation with U_∞ = 10 m/s, and σ_∞ = 1.4. Flow is from left to right

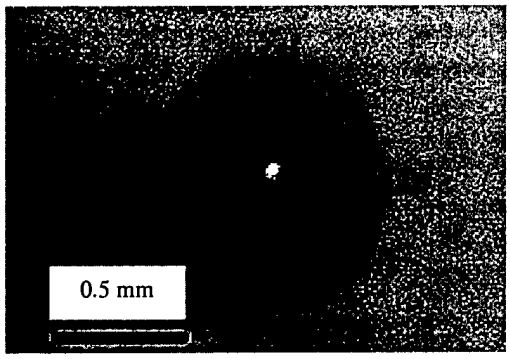

(a)

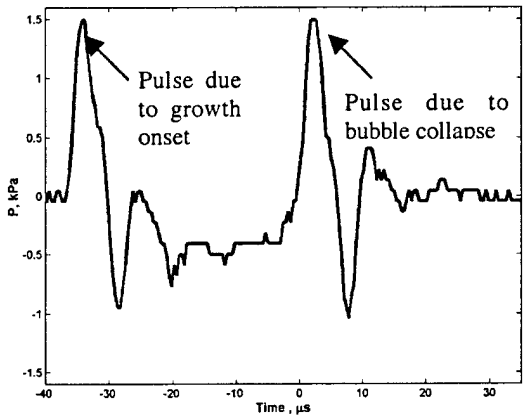

(b)

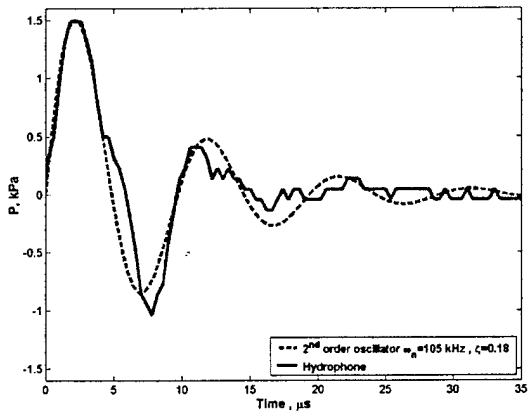

(c)

Figure 3: (a) Five superposed exposures of a laser produced spherical cavitation bubble taken every 6 μs in a quiescent water container; (b) the resulting acoustic pressure trace recorded from the hydrophone; (c) the expanded hydrophone pressure trace produced upon bubble collapse (solid line) along with the second-order response of a SDOF oscillator to a Dirac-delta input with system ϖ_n = 105 kHz and damping ratio, ζ=0.18 (dashed line).

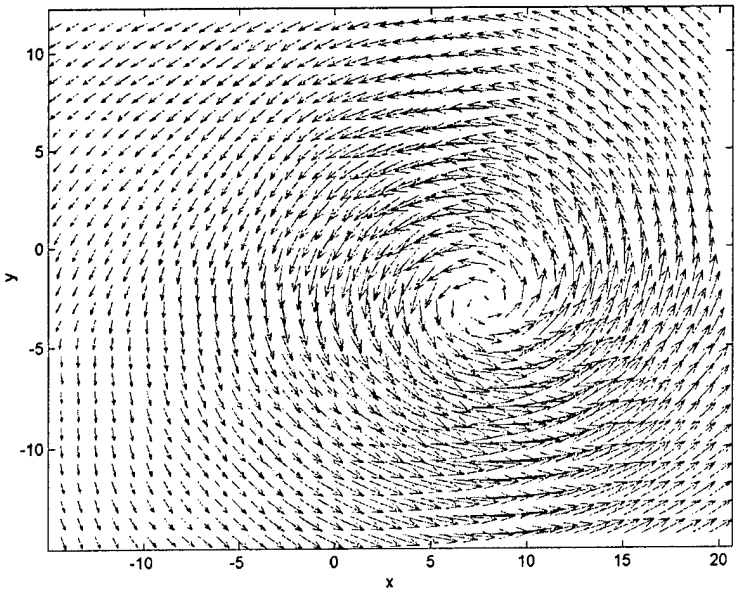

(a)

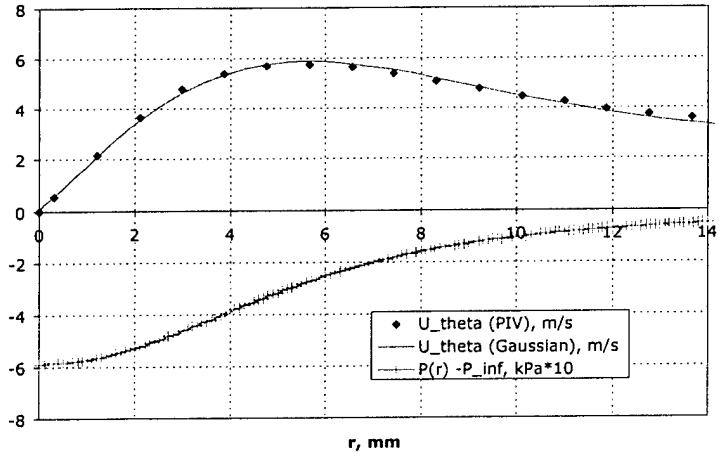

(b)

Figure 4: (a) The average vector map of the flow perpendicular to the vortex axis 90 mm downstream of the tailing edge for U_∞= 10 m/s; (b) the measured tangential velocity, $u_\theta(r)$, along with the velocity distribution for the Gaussian vortex with r_c = 5.6 mm and Γ_o = 0.290 m^2/s and the resulting calculated pressure depression, $P(r) - P_\infty$.

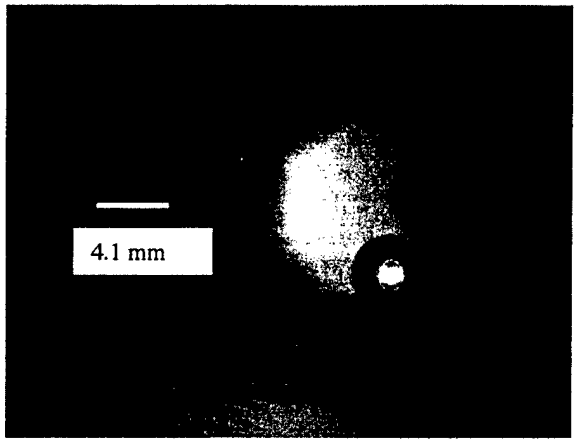

(a)

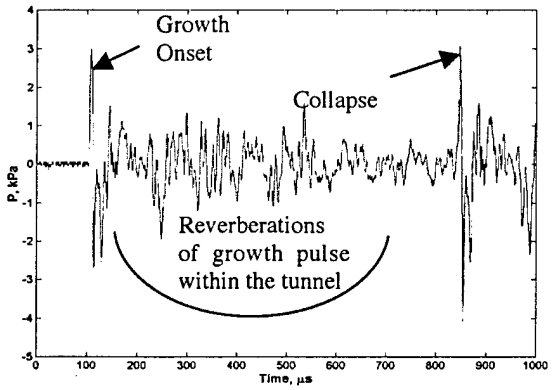

(b)

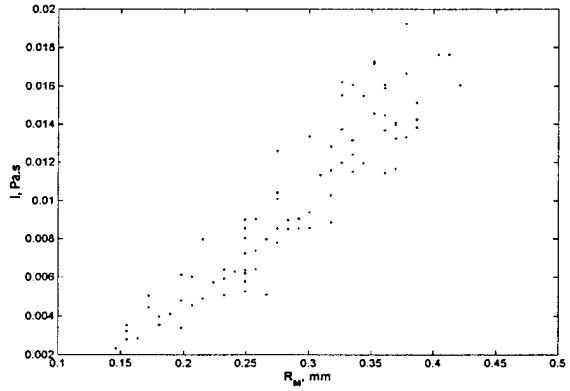

(c)

Figure 5: (a) Ten images of a laser produced bubble taken 40 μs apart in the water tunnel test section without flow with P_∞ = 31 kPa; image dimensions (V 23.1 x H 31.9 mm); (b) the pressure-time trace recorded by the hydrophone; (c) the acoustic impulse created during bubble collapse versus the maximum bubble radius.

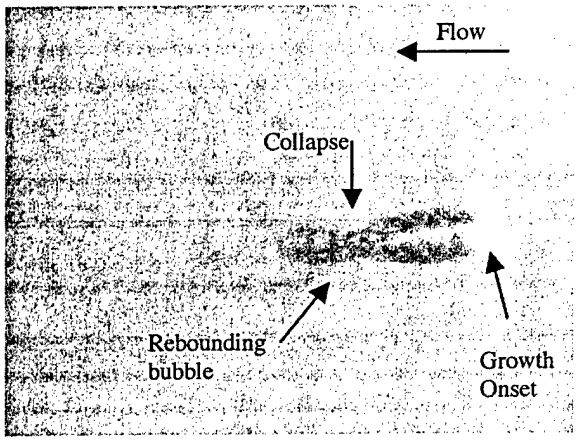

(a)

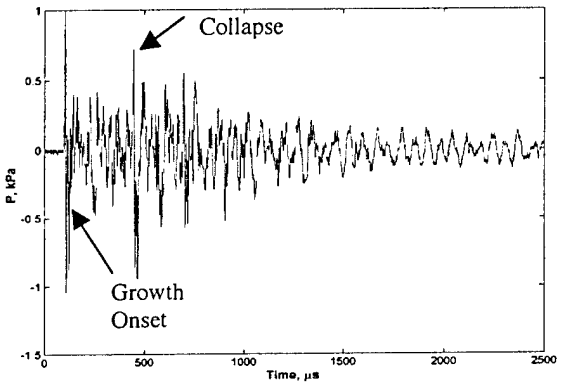

(b)

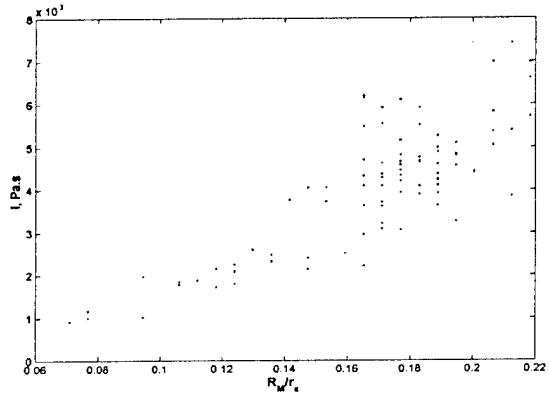

(c)

Figure 6: (a) Ten exposures of a laser produced bubble created in the vortex taken 54 μs apart with σ_∞ = 2.15, U_∞=10m/s; the bright region on the right results from pixel saturation from the original laser pulse; image dimensions (V 15.9 x H 21.0 mm); (b) the pressure-time trace recorded by the hydrophone; (c) the acoustic impulse created during bubble collapse versus the normalized maximum bubble radius (normalized by the vortex core radius).

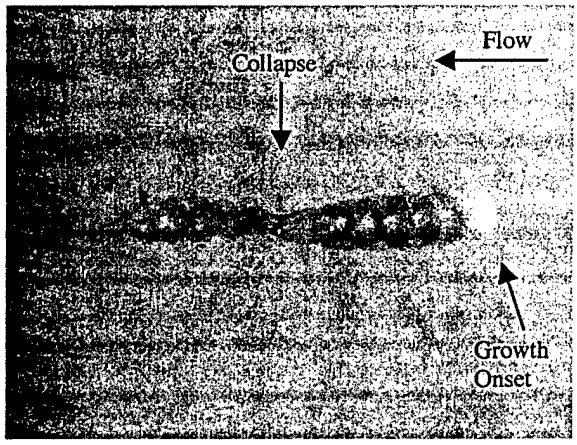

(a)

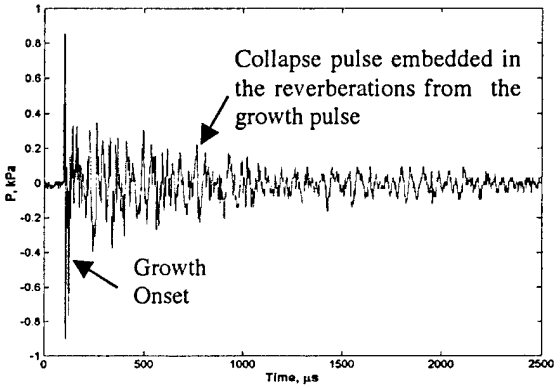

(b)

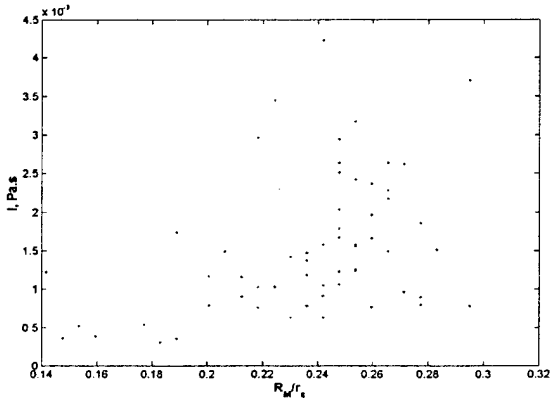

(c)

Figure 7: (a)Ten exposures of a laser produced bubble created in the vortex taken 94 μs apart with σ_∞ = 1.73, U_∞ =10m/s; the bright region on the right results from pixel saturation from the original laser pulse; image dimensions (V 15.9 x H 21.0 mm); (b) the pressure-time trace recorded by the hydrophone; (c) the acoustic impulse created during bubble collapse versus the normalized maximum bubble radius (normalized by the vortex core radius).

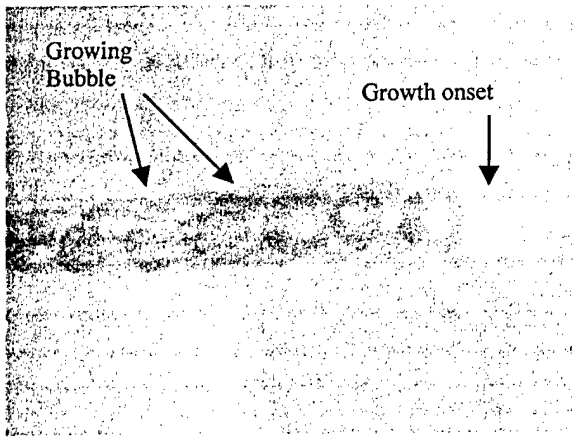

(a)

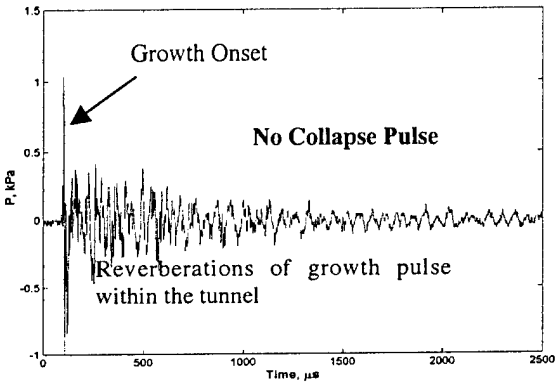

(b)

Figure 8: (a) Ten exposures (last two exposures outside the frame) of a laser produced bubble created in the vortex taken 154 μs apart with σ_∞ = 1.49, U_∞=10m/s; the bright region on the right results from pixel saturation from the original laser pulse; image dimensions (V 15.9 x H 21.0 mm); (b) the pressure-time trace recorded by the hydrophone. At this cavitation number, the bubble continues to grow along the vortex axis after initiation with the laser.

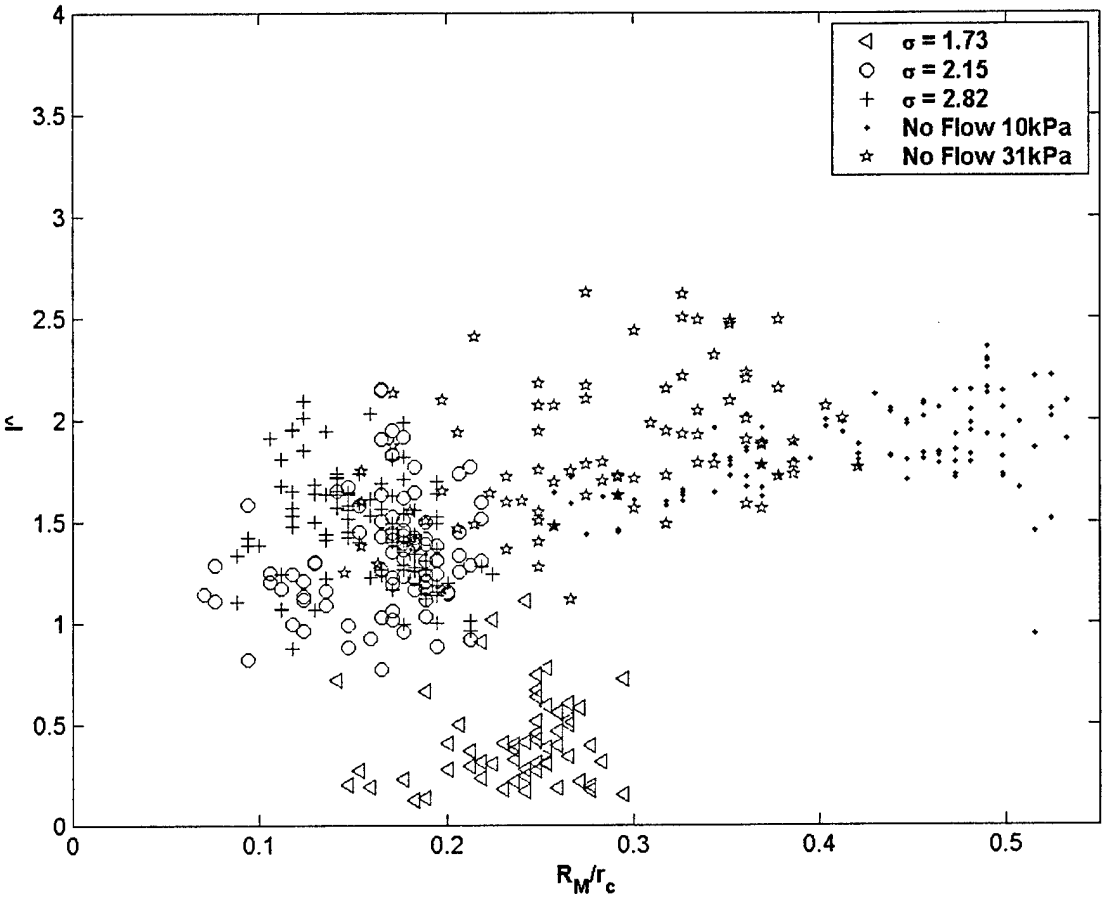

Figure 9: The dimensionless acoustic impulse, $\hat{I} = I.r_H / \left(\frac{1}{3}\eta_R \rho c \, \Delta P \, R_M^3 \theta\right)^{1/2}$, versus the dimensionless maximum bubble radius, $\hat{R}_M = R_M / r_C$, for P_∞= 10 kPa without flow (·), P_∞ = 31 kPa without flow (*), σ_∞ = 2.82 (+), σ_∞ = 2.15 (o), and σ_∞ = 1.73 (<). For this plot the acoustic conversion efficiency η_R was chosen to be 100%, and the collapse pulse width θ 10 nanoseconds.

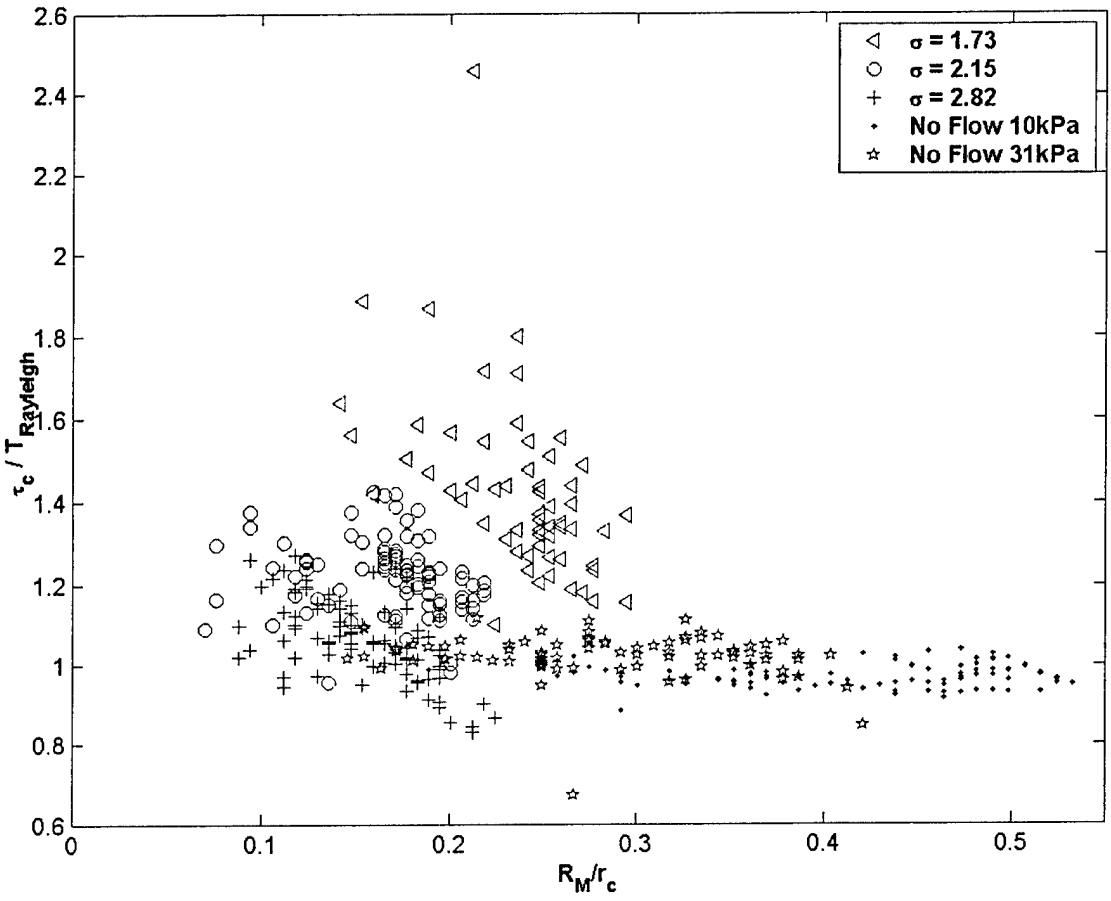

Figure 10: The dimensionless collapse time $t_c/T_{Rayleigh}$ versus the dimensionless maximum radius, $\hat{R}_M = R_M / r_C$, for P_∞= 10 kPa without flow (·), P_∞= 31 kPa without flow (*), σ_∞ = 2.82 (+), σ_∞ = 2.15 (o), and σ_∞ = 1.73 (<).

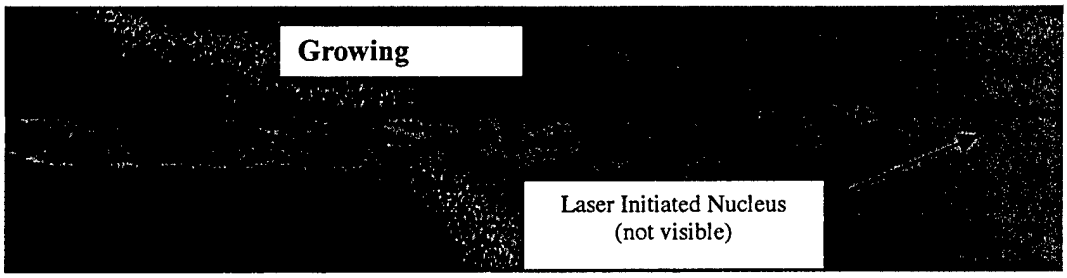

(a)

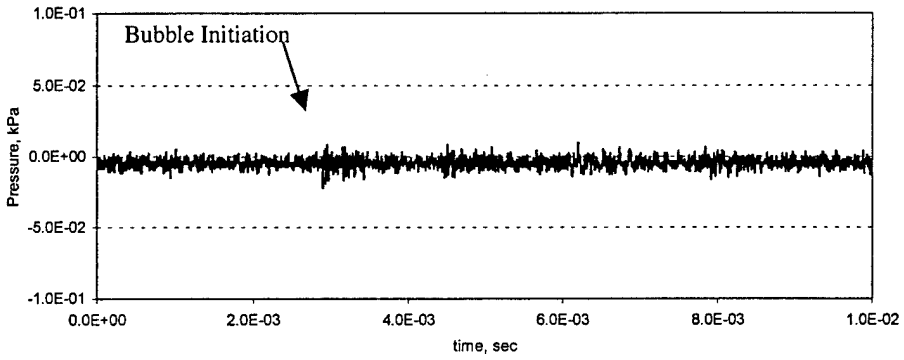

(b)

Figure 11: (a) Ten exposures of a bubble created by a low energy laser pulse in the vortex taken 300 μs apart with σ_∞ = 1.19; the initial nucleus is small and not visualized in the image; flow is from right to left; (b) the pressure-time series recorded by the hydrophone, which is equivalent to the baseline hydrophone signal before inception.

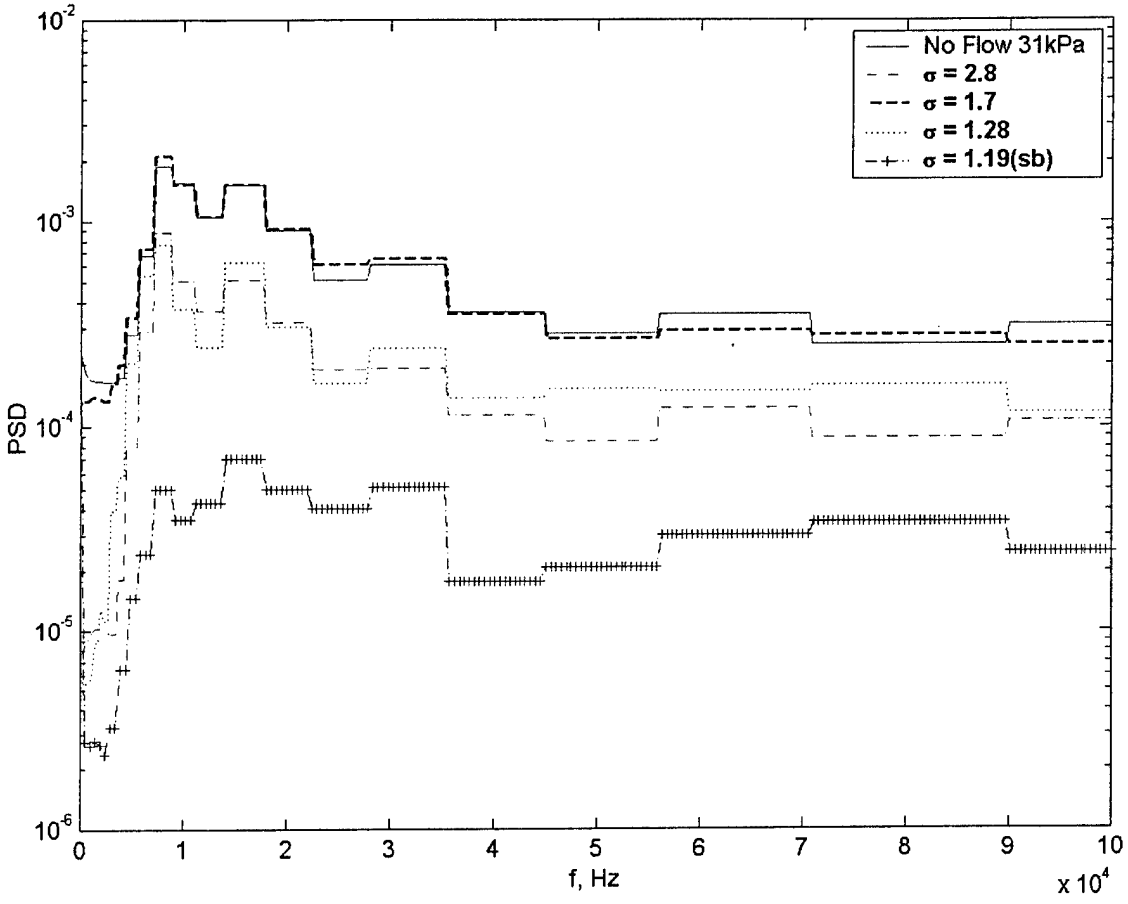

Figure 12: Average power spectral density of the hydrophone signal for the 5 different cases corresponding to macroscopic bubbles created without test-section flow, and in the vortex for σ_∞ = 2.8, 1.70. 1.28 The spectrum of the noise recorded when the microscopic bubbles (sb) were created at σ_∞ = 1.19 is also included, and this is equivalent to the baseline spectrum without cavitation. The spectrum analyzer was triggered to analyze the noise signal produced due to the bubble collapse only, and the spectra from 1000 acoustic events were averaged.

Capture and Inception of Bubbles Near Line Vortices

G. Owies*, I. E. van der Hout, C. Iyer†, G. Tryggvason††, and S. L. Ceccio***

*University of Michigan, Ann Arbor

**Delft University of Technology

†The Ford Motor Company

††Worcester Polytechnic Institute

Submitted to *Physics of Fluids*

Abstract

The capture of a bubble by a line vortex for both non-cavitating and cavitating conditions using a one-way Particle-Tracking Model (PTM) and Direct Numerical Simulation (DNS) is examined. These results are compared to experimental observations. The particle-tracking model can successfully predict the capture time for small bubbles by a line vortex. For the small bubbles starting far from the vortex, variation in capture time with differing choices of the lift coefficient are relatively small. The accuracy of the PTM is reduced as the bubble moves to within the core radius, and the DNS solutions suggest that the PTM will under-predict the capture time in the final stages of collapse. The effect of bubble deformation and bubble vortex interactions will be important only at the final stages of bubble capture. The non-cavitating PTM can be used when considering the capture of cavitation nuclei. The bubble volume changes very slowly until the final stages of bubble capture. Consequently, it is useful to separate the process into the non-cavitating capture of the nucleus and then the growth of the nucleus in the low-pressure core region. The growth of the nucleus prior to cavitation inception is relatively small, but such bubble growth will lead to a somewhat faster capture as the bubble comes near the core.

*corresponding author

1. Background

Hydrodynamic lifting surfaces associated with propulsion and control systems often develop concentrated trailing vortices. Small bubbles near the concentrated vortex will be drown toward to axis of flow rotation, and if the core pressure falls below vapor pressure, these small bubbles can act as nucleation sites for vortex cavitation, and Arndt (2002) has recently this phenomenon. The probability that a cavitation bubble will occur is related the concentration and size distribution of the free-stream nuclei (*i.e.* the nuclei number distribution) and the likelihood that the bubble is found in the possibly transient region of low pressure. The bubble may already be present in the core region when an unsteady flow phenomenon, such as vortex stretching, reduced the core pressure. Or, the nucleus could be captured by the low-pressure vortex. The likelihood of bubble capture is related to the probability of the nuclei's presence within or near the vortex core and to the probability that nuclei may be captured by the vortex while the core pressure in the vortex is reduced. This second process is governed by the time a nucleus takes to move close to the vortex axis, the capture time. With an estimate of the capture time, it is then possible to identify which nuclei surrounding an unsteady vortex will lead to discreet vortex cavitation bubbles.

The vortex-induced capture, interaction, and growth of small bubbles have been studied by several researchers. Sridhar and Katz (1999) studied the effect of an entrained bubble in a vortex ring using a particle image velocimetry and showed that in certain cases the entrained bubble can substantially change the structure of the vortex. Hsiao *et al.* (1999) examined the capture of a cavitation nucleus by a tip vortex employing a Reynolds Averaged Navier Stokes (RANS) model of the non-cavitating flow along with a particle-tracking model to describe the dynamics of the nucleus. This approach assumes that the dynamics of the bubbles can be

predicted with spherical bubbles dynamics and a one-way coupled momentum balance on the bubble. Chahine and co-workers have used using both RANS and boundary integral methods to study vortex bubble interaction (Chahine,1990; Chahine and Hsaio, 1994; Hsiao and Chahine 2001; Chahine and Hsaio, 2002). They have shown how captured bubbles can significantly deformed as they are captured by the vortex, grow, and collapse.

Models of bubble-flow interactions often employ one-way coupling between the flow and the motion of the bubble whereby the presence of the bubble does not alter the underlying flow field. An equation of motion for the trajectory of the bubble is solved using a force balance on the bubble. For cavitating flows, the Rayleigh-Plesset equation is employed to describe the dynamics of the cavitating bubble. Such Particle Tracking Models (PTM) often assumes that the bubbles remain spherical during the bubble capture, growth, and collapse. However, as the volume of a bubble increases, the pressure and flow gradients near the vortex can cause the bubble to deform and can lead to significant modification of the forces on the bubble. Higher fidelity simulations of the bubble-flow interactions are possible, but can be computationally intensive. It would be preferable if the one-way particle tracking models can be used to yield an accurate estimate of the bubble capture times.

In the present work, we will examine the capture of a bubble by a steady line vortex for both non-cavitating and cavitating conditions using a one-way particle-tracking model and Direct Numerical Simulation (DNS). Experimental observations of bubble capture are then compared with the predicted results of the PTM. These data are used to explore the accuracy and limitations of the one-way particle-tracking models.

2. One-Way Coupled Particle Tracking Model of Bubble Capture

The dynamics of small bubbles in the flow can be calculated assuming that their presence does not significantly alter the non-cavitating flow. The effect of the flow on a bubble can be determined through the equation of motion for the particle (Maxey and Riley (1983); Magnaudet and Eames (2000)):

$$\rho_B V_B \frac{d\mathbf{u}_B}{dt} = V_B(\rho_B - \rho_f)\mathbf{g} - V_B \nabla p + \tfrac{1}{2}\rho_f V_B\left(\frac{D\mathbf{u}}{Dt} - \frac{d\mathbf{u}_B}{dt}\right) + \mathbf{F}_D + \mathbf{F}_L + \mathbf{F}_B + \mathbf{F}_V \qquad (1)$$

where ρ_B is the bubble density, ρ_F is the fluid density, V_B is the volume of the bubble, $\mathbf{u}_B$ is the bubble velocity, $\mathbf{u}$ is the fluid velocity in the absence of the bubble at the center of the bubble (the unperturbed velocity). $\mathbf{F}_D$ is the drag force, $\mathbf{F}_L$ is the lift force, $\mathbf{F}_B$ is the Basset history force, and $\mathbf{F}_V$ is the force due to volume changes. In the present analysis, the drag force is given by

$$\mathbf{F}_D = C_D \tfrac{1}{2}\rho_f A_B |\mathbf{u} - \mathbf{u}_B|(\mathbf{u} - \mathbf{u}_B) \qquad (2)$$

where

$$C_D = \frac{24}{\mathbf{Re}_B}(1 + 0.197\mathbf{Re}_B^{0.63} + 2.6(10^{-4})\mathbf{Re}_B^{1.38}) \qquad (3)$$

and $\mathbf{Re}_B = |\mathbf{u} - \mathbf{u}_B| 2R/\nu_f$ is the bubble Reynolds number based on the bubble radius, R, and projected area, A_B (Haberman and Morton (1953)). We will neglect the Basset force term, as the bubble relative acceleration is expected to be small (a detailed discussion of the relative size of the Basset term is found in Maxey and Riley (1983)). The force due to the bubble volume variation is given by Johnson and Hsieh (1966) as:

$$\mathbf{F}_V = 2\pi R^2 \rho(\mathbf{u} - \mathbf{u}_B)\frac{dR}{dt} \qquad (4)$$

The buoyancy, pressure gradient, and added mass terms are also included in equation, with an added mass coefficient of 1/2 for spherical bubbles. We will ignore the effects of buoyancy on the small bubbles considered here.

The lift forces on the bubble is related to the slip velocity and the circulation of the unperturbed fluid at the center of the bubble:

$$\mathbf{F}_L = C_L \tfrac{1}{2}\rho_f A_B |\mathbf{u}-\mathbf{u}_B|(\mathbf{u}-\mathbf{u}_B) = \tfrac{3}{8}\rho_f V_B C_L \frac{(\mathbf{u}-\mathbf{u}_B)\times\omega}{\alpha} \tag{5}$$

where $\alpha = |\omega|R/|\mathbf{u}-\mathbf{u}_B|$ is the dimensionless shear rate, and $\boldsymbol{\omega}$ is the fluid vorticity of the undisturbed flow at the center of the bubble. The lift coefficient is a function of both the shear and vorticity. Auton (1987) and Auton *et al.* (1988) showed that for weak shear ($\alpha << 1$) the lift coefficient is given by

$$C_{L,A} = \tfrac{4}{3}\alpha \tag{6}$$

Saffman (1965) showed that, for low Reynolds numbers ($\mathbf{Re}_B < 20$),

$$C_{L,S} = 5.82\mathbf{Re}_B^{-0.5}\alpha^{0.5} \tag{7}$$

For higher Reynolds numbers, Dandy and Dwyer (1990) used numerical analysis to show that for $0.0005 < \alpha < 0.4$ and $\mathbf{Re}_B > 20$,

$$C_{L,D} \approx 0.3\alpha \tag{8}$$

Lastly, Sridar and Katz (1995) experimentally determined the lift coefficient on bubbled with diameters between 500 and 800 μm and $20 < \mathbf{Re}_B < 80$, and found relatively high lift coefficients

$$C_{L,SK} = 0.59\alpha^{0.25} \tag{9}$$

To determine the volume variation for a spherical bubble, the Rayleigh-Plesset equation given is used to determine the time-varying bubble radius, $R(t)$:

$$R\frac{d^2R}{dt^2}+\frac{3}{2}\left(\frac{dR}{dt}\right)^2=\frac{1}{\rho_f}\left(p_V+p_{GI}\left(\frac{R_O}{R}\right)^{3k}-p_B-\frac{2\overline{\sigma}}{R}-\frac{4\mu_f}{R}\frac{dR}{dt}\right) \tag{10}$$

This relation is derived for a spherical bubble in an unbounded fluid, and p_B is the pressure far away from the bubble, p_{GI} is the pressure of the non-condensable gas initially in the bubble, k is the polytropic exponent, and $\overline{\sigma}$ is the surface tension. For the particle tracking model, p_B is often taken as the local fluid static pressure at the location of the bubble center. If the bubble is small and the pressure gradients near the bubble are mild, then $\nabla p \cdot R/p << 1$ at the bubble center, and we may model $p_B \approx p$.

3. Gaussian Vortex Model

We will consider the capture of bubbles by a Gaussian vortex. Also known as Lamb-Oseen vortex, the vorticity distribution at a radius, r and at time, t is given by:

$$\omega=\frac{\Gamma_O}{4\pi\nu_f t}e^{\frac{-r^2}{4\nu_f t}} \tag{11}$$

The tangential velocity around the axis is given by:

$$u_\theta(r)=\frac{\Gamma_O}{2\pi r}\left(1-e^{\frac{-r^2}{4\nu_f t}}\right) \tag{12}$$

In many cases of high Reynolds number flows, the time-scale associated with vorticity diffusion, $\tau_\nu \approx r_C^{\,2}/4\nu_f$, is long compared to the time of bubble capture. We can then assume that the vorticity distribution is constant, with a resulting velocity distribution

$$u_\theta(r)=\frac{\Gamma_O}{2\pi r}\left(1-e^{-\eta_1(r/r_C)^2}\right) \tag{13}$$

where $\eta_1 = 1.255$, and the maximum tangential velocity, u_C, occurs at the core radius and is given by

$$u_C = \eta_2 \frac{\Gamma_O}{2\pi r_C} \tag{14}$$

where $\eta_2 = 0.715$. The pressure depression at the vortex centerline, $r = 0$, is given by

$$p(r) - p_\infty = \int_\infty^0 -\frac{\rho_f u_\theta{}^2(r)}{r} dr = -\rho_f \left(\frac{\Gamma_O}{2\pi r_C}\right)^2 f\left(\frac{r}{r_C}\right)$$

where

$$f\left(\frac{r}{r_C}\right) = \left(\frac{-1}{2(r/r_C)^2}\right) \times \begin{bmatrix} -1 + 2e^{-\alpha(r/r_C)^2} - e^{-2\alpha(r/r_C)^2} \\ -2\alpha(r/r_C)^2 Ei(\alpha(r/r_C)^2) \\ +2\alpha(r/r_C)^2 Ei(2\alpha(r/r_C)^2) \end{bmatrix} \tag{15}$$

At the vortex core,

$$p_C - p_\infty = -\rho_f \left(\frac{\Gamma_O}{2\pi r_C}\right)^2 f(0) = -\eta_3 \rho_f \left(\frac{\Gamma_O}{2\pi r_C}\right)^2 \tag{16}$$

where $\eta_3 = f(0) = 0.870$. Here we are neglecting the possibility that there may be non-uniform flow along the vortex axis.

The vortex Reynolds number is

$$\mathbf{Re}_C = \frac{u_C r_C}{\nu_f} \tag{17}$$

The Weber number of a bubble with radius R_O is

$$\mathbf{We} = \frac{\rho_f R_O u_C^2}{2\bar{\sigma}} \tag{18}$$

The vortex cavitation number is defined as:

$$\sigma_\infty = \frac{p_\infty - p_V}{\frac{1}{2}\rho_f u_C^2} \tag{19}$$

4. Direct Numerical Simulations of Bubble Dynamics

The numerical method used in this study to compute the Navier-Stokes equations is a Direct Numerical Simulation (DNS) front- tracking method for multiphase flows developed by Unverdi and Tryggvason (1992) and improved by Esmaeeli and Tryggvason (1998, 1999). The fluids inside and outside the bubbles are taken to be Newtonian and the flow is incompressible and isothermal, so that the densities and viscosities are constant within each phase. The unsteady, viscous, incompressible Navier-Stokes equations are solved by a finite-difference approximation on a fixed staggered grid, while the interface between the bubbles and fluid were explicitly represented by a separate, unstructured grid that moves through the stationary one. The front (interface) keeps the density and viscosity discontinuities sharp and also provides means for calculation of the surface tension forces. A numerical method based on the Marker-And-Cell method is used to solve the unsteady Navier-Stokes equations over the entire computational domain. This "one-field" formulation, which computes both the properties within the bubbles and in the ambient fluid, is used in conjunction with a linked list of markers that is used to explicitly track the position of the fluid interfaces. A single Navier- Stokes equation with variable density and viscosity is solved for the entire domain, and the surface tension is added as a body force concentrated at the fluid interfaces. The numerical scheme used is a conservative second-order accurate, centered difference scheme for spatial variables, and explicit second-order time integration. Yu *et al.* (1995) used this front tracking method to examine collapse of bubbles is shear-flow, and the model developed in this study is used in the present work. Resolution and accuracy studies for the cavitation models were reported in that study.

5. Experimental Setup

Figure 1a shows the setup for the creation of single cavitation bubbles in a vortical flow. Single cavitation bubbles were created near a steady line vortex using the University of Michigan 9-Inch Cavitation Tunnel. The water tunnel has a circular contraction downstream of a series of flow management screens with contraction ratio 6.4:1. The test section has a 22.9 cm diameter round inlet that is then faired into a rectangular test section with widely rounded corners. Four acrylic windows (93.9 cm by 10.0 cm viewing area) permit optical access to the test section flow. The flow in the test section can be operated at pressures from vapor pressure to approximately 200 kPa. The average velocity in the test section is variable up to 18 m/s. A de-aeration system can be used to vary the dissolved gas content of the flow, and the inlet water is filtered to 1 microns.

A vortical flow was created using a cambered hydrofoil mounted to one window of the test section. The hydrofoil has a rectangular planform of 9.5 cm span and 16.8 cm chord. The tip of the hydrofoil was truncated with sharp edges. The hydrofoil mount allows continuous changes of the incident flow angle. A series of tip and trailing edge vortices will be shed near the tip, and these vortices will merge to form a single vortex within one-half chord length downstream of the trailing edge. Measurements of the bubble/vortex interactions were taken for a free-stream velocity of 10 m/s and a variety of pressures. The dissolved oxygen content was measured with an Orion Model 810 dissolved oxygen meter. In order to reduce the number of free-stream nuclei, the free-stream gas-content was reduced to below 1.5 ppm during the measurements. A photograph of the hydrofoil with developed tip vortex cavitation is shown in **Figure 1b**.

Planar Particle Imaging Velocimetry (PIV) was used to measure the vortical flow field at a station 9.0 cm downstream of the trailing edge. A double-pulsed light sheet 9 mm thick was created perpendicular to the mean flow direction using two pulsed Nd:YAG lasers (Spectra Physics model Pro-250 Series). 15.3 micron average diameter silver coated glass spheres were used to seed the flow. An acrylic prism was optically mounted to a window of the test-section for viewing of the light sheet with reduced optical distortion. The flow was captured with a PIV image capture system produced by LaVision Inc. Double-pulsed images of the light sheet were acquired with a digital camera with 1280 x 1024 pixels. Optical distortion of the planar light sheet image was corrected through a calibration procedure that employed the imaging of a regular grid in the location of the light sheet plane. Velocity vectors were produced from the double-pulsed images using the LaVision image analysis software Davis6.0.4. Multipass processing with a final window size of 32 x 32 pixels was used with 12% window overlap in the final pass to produce 41 x 27 in plane velocity vectors at 0.62 mm spacing. Since the camera-imaging plane was not parallel to the light sheet and it had an angular shift of 45° with the horizontal direction, this velocity component was corrected by knowledge of the camera angle and the tunnel free stream velocity.

For these experiments, the free-stream velocity was fixed at 10 m/s. **Figure 2a** shows a vector map of the average planar vortical flow field measure perpendicular to the vortex axis produced after averaging 300 instantaneous flow fields. **Figure 2b** plots the average tangential velocity, $u_\theta(r)$, as a function of the distance from the vortex center, r, along with a fitted curve for a Gaussian vortex and the computed pressure depression as a result of the vortex. For the measured vortex, the fitted core radius was r_c =5.6 mm and the strength was Γ_o = 0.290 m^2/sec. Examination of the instantaneous images indicated that the vortex core did not wander

significantly. The amplitude of wandering was consistently less than 10% of r_c. Consequently, no correction for vortex wandering was needed, as discussed by Boulon *et al.* (1999).

Optically stimulated vortex-cavitation bubbles were created at the vortex centerline. As the cavitation number was reduced, discreet cavitation events occurred near the vortex core due to the creation of a nucleus after the collapse of the initial laser-induced bubble. Natural cavitation also occurred are various locations along the vortex axis downstream of the location of vortex roll-up. However, at such low air content, the event rate of this cavitation was relatively low (< 0.1 event per second). Bubble-capture and any resulting vortex cavitation could then be examined after the introduction of a nucleus though a focused pulse of laser light near the axis of the vortex. By varying the free-stream pressure and laser energy, the initial size of the laser-induced bubble could be controlled. Images of the bubble were observed with a Cooke Corp. "FlashCam" digital camera. This camera has an effective resolution of 750 x 240 pixels, and it is capable of recording up to consecutive 10 exposures on the same image, with varying integration times and delays between each exposure. A pulse delay generator (SRS model DG535) was used to trigger the camera at varying delays from the laser light pulse.

6. Non-Cavitating Bubble Capture Predicted With the Particle Tracking Model

The one-way coupled particle-tracking model (PTM) was used to predict the trajectory and capture time for spherical bubble capture by a Gaussian vortex, $t_C^* = t_C u_C / r_C$. An implicit second order numerical scheme was used to integrate the radial and tangential components of equation 1 with a time-stepping procedure. The case of non-cavitating bubbles was first considered. Bubbles of varying sizes were released at varying radial positions away from the vortex axis, r_X, with an initial velocity equal to that of the fluid at the bubble center. A bubble

was considered captured when it intersected the annulus defined by 1/4 of the core radius, which approximately corresponds to the region of lowest core pressure. In these simulations, the bubble remained spherical, which is equivalent to **We** << 1.

For bubbles very far away from the vortex, we can assume that the bubble accelerations and lift forces are negligible and that there exists a balance between the pressure gradient induced force and the drag force on the bubble, $V_B \nabla P \approx F_D$. If we assume that the largest component of the bubble velocity is in the radial direction, $u_{B,r}$, the force balance far from the vortex axis becomes

$$\frac{-u_\theta{}^2(r)}{r} \rho_f \tfrac{4}{3}\pi R_O^3 \approx \tfrac{1}{2}\rho_f C_D \pi R_O^2 u_{B,r}^2 \tag{20}$$

where $u_\theta(r) \approx u_C r_C / \eta_2 r$, and $C_D \approx 12\nu_f / R_O u_{B,r}$. The bubble velocity then becomes

$$u_{B,r} \approx -\frac{2(u_C r_C R_O)^2}{9\eta_2^2 \nu_f} \frac{1}{r^3} \tag{21}$$

This expression can be integrated to yield the approximate capture time for bubbles far from the vortex core, $r_X / r_C >> 1$:

$$t_C^* \approx (u_C / r_C) \int_{r_X}^{0} \frac{1}{u_{B,r}(r)} dr = \frac{9\eta_2^2}{8\mathbf{Re}_C} \left(\frac{r_C}{R_O}\right)^2 \left(\frac{r_X}{r_C}\right)^4 \tag{22}$$

The predicted capture times are shown in **Figure 3** for both equation 22 and the results of the PTM. The approximate capture time under-predicts the capture time compared to that of the PTM, and the extent of the under-prediction increases with increasing bubble size. However, the relationship reveals the trends in capture time with r_X / r_C, r_C / R_O, and $\mathbf{Re}_C$. The pressure gradient induced force increases with R^3, while the drag force increases with R^2. Consequently, in regions of slow bubble acceleration, smaller bubble will take much longer to move toward the vortex center.

Once the bubbles come closer to the vortex axis, the lift and added mass forces contribute significantly to the bubble motion. **Figure 4a and 4b** shows the capture time for the case with $\mathbf{Re}_C = u_C r_C / \nu = 3 \times 10^4$, which is equivalent to the experimentally measured vortex. The solution is shown for the four proposed lift coefficients. The force on the bubble resulting from the local pressure gradient drives the bubble toward the vortex axis, while the drag, lift, and added mass forces act to retard the bubble motion.

Variation in lift coefficient leads to some change in the capture time, although the effect is secondary. We can scale the average bubble Reynolds number as

$$\mathbf{Re}_B \sim \frac{r_X}{t_C}\frac{R_O}{\nu_f} = \mathbf{Re}_C \frac{1}{t_C^*}\frac{R_O}{r_C}\frac{r_X}{r_C} \tag{23}$$

Here $r_X / r_C \sim 1$, $t_C^* \sim 10$, and $\mathbf{Re}_C \sim 10^4$. Then the bubble Reynolds number will be $\mathbf{Re}_B \sim 10(R_O / r_C)^{-1}$, and the bubble Reynolds number will decrease with increasing capture time and decreasing bubble size. The lift coefficients proposed by Saffman (equation 7) is valid for $\mathbf{Re}_B < 20$, and the largest bubbles approach this limit. The relationships proposed by Dandy and Dwyer (equation 8) and Sridar and Katz (equation 9) are valid for somewhat higher bubble Reynolds numbers, up to ~100. The highest $\mathbf{Re}_B$ will occur near the point of capture.

The highest levels of vorticity occur for $r / r_C < 2$, along with the highest bubbles slip velocities. The capture time when the bubble is within $r / r_C < 2$ is on the order of unity, making the relative velocity $\sim u_C$. The non-dimensional shear in the core, α_C, can then be scaled as

$$\alpha_C = \frac{|\omega_C| R_O}{|\mathbf{u} - \mathbf{u}_B|} \sim \frac{2u_C R_O}{r_C}\frac{1}{u_C} = \frac{2R_O}{r_C} \tag{24}$$

The highest local values of α_C occur within the vortex core, however. For the smallest bubbles considered here, $\alpha_C << 1$. For the largest bubbles considered here, $\alpha_C \sim 0.1$ to 1. The lift coefficients proposed by Auton (Equation 6) and Dandy and Dwyer (Equation 8) are for the case of $\alpha < 1$, making them less appropriate for the final portion of the capture process of larger bubbles. **Figure 5** shows the variation of the capture time with the vortex Reynolds number for the case of $r_C / R_O = 50$, using the lift coefficient of Auton (equation 6). As expected, the time for bubble capture increases with increasing fluid viscosity and decreases as $\sim 1/\mathbf{Re}_C$.

6. Direct Numerical Simulations of Non-Cavitating Bubble Capture

The particle-tracking model does not account for bubble deformation and bubble flow interaction that may occur during the final stages of collapse. It is expected that these effects would be the most important for relatively large bubbles as they near the vortex core. To examine this process, bubbles with $r_C / R_O \sim 10$ were computed using DNS for various Weber numbers and cavitation numbers. In these simulations, the effective vortex maximum tangential velocity and core size are $u_C = 5$ m/s and $r_C = 2.5$ mm, respectively. The length of the computational domain is 4 core radii, or 10 mm. The vortex Reynolds number $\mathbf{Re}_C$ = 250, which is about 50 times lower than the experimentally examined vortex. However, even at the lower Reynolds number, the amount of vortex diffusion during the computation was relatively small, with the core growing less than 5% over the duration of the computation. The kinematic viscosity and density of the gas phase were 1/10 that of the fluid. The initial bubble radius was varied as a proportion of the core radius, and the release position of the bubble was varied along the radius. Again, the bubble was given an initial velocity equal to the mean of the surrounding fluid. Bubbles were released at $y/L = 0.5$ and varying x/L, with the vortex axis at $x/L = y/L = 0.5$.

A grid resolution study was performed for the capture of a bubble with $r_C/R_O = 8$ and **We** = 0.13 for a non-cavitating bubble. The bubble was released at $r_X/r_C = 0.5$, a region of large flow gradients. Simulations with resolutions of 96^3, 128^3, 160^3 were compared, and bubble center position at non-dimensional time t^* = 1.77 were within 1% of the domain length. It was concluded that a resolution of 128^3 would be sufficient.

Figure 6a shows the trajectory of a non-cavitating bubble with $r_C/R_O = 8$ and **We** = 0.13 for $r_X/r_C = 1.0$, and **Figure 6b** shows the vorticity in the x-y plane. It is clear that the bubble locally modifies the flow, and a wake develops behind the bubble. **Figure 7** shows the trajectory of three bubbles released at r_X/r_C = 1.5, 1.0, and 0.5 along with the prediction of the PTM. Again, the bubble is considered captured when the bubble interface crosses the $r_C/4$. The capture times predicted with the DNS for the three bubbles are t^* = 4.61, 2.22, and 0.74. These are compared with t^* = 4.51, 2.74, and 0.85 for the PTM. Here, the density ratio and vortex properties of the DNS calculation were used in the PTM, and the lift coefficient of Auton was used. The low Weber number leads to relatively little bubble deformation, and the capture time are within 20% of those from the PTM. This variation is on the order of the changes in the PMT prediction that result from the use of the different lift coefficients.

Figure 8a and 8b show the effect of varying Weber number of the trajectory and capture time for two different release positions, r_X/r_C = 1.5 and 1.0. The time decreases with increasing Weber number, implying that increased bubble deformation leads to faster bubble capture. The capture times computed with the PTM and the DNS for r_X/r_C = 0.5 are similar. But the PTM under-predicts the capture times for the bubble released at r_X/r_C = 1.5, suggesting the accumulated effect of varying lift coefficient on the final capture time. **Figure 9a** and **9b** show the effect of varying bubble size on capture time, with the larger bubble with $r_C/R_O = 8$ being

captured faster that the bubble with $r_C/R_O = 12$ for **We** = 0.1. The PTM under-predicts the capture time for both cases, suggesting that the lift and drag coefficients of the PTM are too small when the bubble is close to cature, even though the lift coefficient used is the largest of the four considered. A third trajectory was calculated with an arbitrarily increased drag coefficient chosen to match the DNS trajectory. The increase in the drag coefficient was 1.5 times for $r_C/R_O = 8$ and 2 times $r_C/R_O = 12$.

7. The Capture of Cavitation Nuclei

The capture of potentially cavitating nuclei are now considered. As the gas bubbles experience reduced pressure, volume of the bubbles will increase isothermally. Bubbles far from the low-pressure region will grow quasi-statically and isothermally ($k = 1$), with the radius given by

$$p_V - p(r) + p_{GI}\left(\frac{R_O}{R(r)}\right)^3 - \frac{2\overline{\sigma}}{R_O}\frac{R_O}{R(r)} = 0 \qquad (25)$$

The radius of the bubble will grow quasi-statically until $p(r) \le p_V$. As the pressure is decreased further, the bubble can begin to grow rapidly. A stability analysis of equation 10 yields the critical radius $R_i(r)$ above which bubbles will grow explosively for a given liquid tension (see Brennen (1995) for a complete discussion):

$$R_i(r) \ge \frac{4\overline{\sigma}}{3(p_V - p(r))} \qquad (26)$$

Vaporous cavitation can occur when the pressure at the vortex axis is less than or equal to the vapor pressure, $p_C \le p_V$. From the relationship for the core pressure (equation 16) and our

definition of σ_∞(equation 19), this is equivalent to the condition $\sigma_\infty \le 2\eta_3/\eta_2^2 = \sigma_i = 3.40$, where σ_i is the cavitation inception index which is a property of the Gaussian vortex.

The static equilibrium radius can then be rewritten in terms of the cavitation and Weber numbers:

$$-\sigma_\infty + \left(\sigma_\infty + \frac{2}{\mathbf{We}}\right)\left(\frac{R_O}{R(r)}\right)^3 - \frac{2}{\mathbf{We}}\left(\frac{R_O}{R(r)}\right) + \frac{2f(r/r_C)}{\eta_2^2} = 0 \qquad (27)$$

And, this expression is valid for $p(r) \ge p_V$ or equivalently,

$$-\sigma_\infty - \frac{2f(r/r_C)}{\eta_2^2} > 0 \qquad (28)$$

The critical radius (equation 26) can also be reformulated in terms of the Weber and cavitation numbers:

$$\frac{R_i(r)}{R_O}\frac{\sigma_i \mathbf{We}}{4} = \left(\frac{1}{f(r/r_C)/\eta_3 - \sigma_\infty/\sigma_i}\right) \qquad (33)$$

Small bubbles are expected to move toward the vortex axis, quasi-statically changing volume until they reach a radial position, r_i, where $R_i(r_i) = R(r_i)$ when unstable bubble growth will occur.

Consequently, the parameters for nuclei capture are r_C, u_C, $\mathbf{Re}_C$, r_X, R_O, $\mathbf{We}$, and σ_∞. We will consider the bubble capture for the experimentally examined vortex, thus setting the first three parameters. The nuclei to be considered are r_C/R_O = 50, 200, 500, and 1000 corresponding to bubbles of 110, 28, 11, and 6 micron radii. This corresponds to $\mathbf{We}$ = 26, 6.5, 2.6, and 1.3 for air bubbles in clean water. We will consider freestream cavitation numbers ranging from σ_∞/σ_i = 1, 7/8, 3/4, 1/2, and 1/4. It should be noted that, in practice, it is difficult to sustain large tensions in the vortex core for steady line vortices. When the tension is sufficiently high, even the smallest nuclei will cavitate, and the vortex core will fill with an annulus of vapor.

Solutions for $R_i(r/r_c)$ and $R(r/r_c)$ were computed for the four conditions described above. The vertical dashed line is the radial position when the fluid pressure reaches the vapor pressure. **Figure 10** shows the case of $r_c/R_o = 50$, the largest bubbles. As the bubbles come closer to the core, the equilibrium radius changes by a factor of up to 3 times before inception. All of these bubbles are initially large enough to cavitate when they pass into the fluid below vapor pressure, even before the added volume increase as they approach the core. **Figure 11** shows the case $r_c/R_o = 200$, and **Figure 12** shows the case $r_c/R_o = 500$. The quasi-static radius change of these bubbles is even smaller, about 2 times. But, even with this increase, the nuclei are still barely big enough to cavitate. Once they pass into the region of tension, they will continue to grow and will then cavitate after reaching the core for the lowest cavitation numbers. Finally, for the case of $r_c/R_o = 1000$ in **Figure 13**, the bubbles change their radii the least as they approach the core, and these small bubbles will only cavitate when the core pressure is in strong tension and after the bubbles have grown quasi-statically.

The capture time of the cavitating nuclei will not differ significantly from that of the non-cavitating case for bubbles that originate far from the vortex. First, the capture criteria will differ, since the bubble can be considered captured once it begins to grow rapidly, and this can occur at a radius that is farther than $r_c/4$, the criteria chosen for the non-cavitating capture. Second, as the bubbles begin to grow quasi-statically, the rate of capture will increase. Third, as the bubbles begin to grow dynamically, the added mass term due to volume changes (equation 4) will retard the bubble's inward motion, but the relatively slow rate of the bubble volume change during the quasi-static growth of the bubble makes this term negligible up until the rapid bubble growth. All of these effects are relatively small, leading to a decrease in the capture time of $\Delta t_c^* \sim 1$ for the larger bubbles. Otherwise, the capture time for the smaller bubbles is not

substantially different between the cavitating and non-cavitating cases, especially for bubbles starting far from the vortex core.

Figure 14 shows the DNS solution for cavitating bubble volume changes during the last part of the bubble capture. The simulation is for a bubble with an initial r_C/R_O = 8, **We** =24, released at r_X/r_C = 0.6. The cavitation number is σ_∞ = 1.0 based on the pressure imposed at the computational boundary. Once the bubble begins to grow, it is pulled in toward the vortex axis and begins to deform. **Figure 15** shows the volume history of the bubble for σ_∞=1.0 and 2.0. Once a spherical bubble begins to grow rapidly, the asymptotic rate of radius growth is

$$\frac{dR}{dt} \approx \left(\frac{2}{3} \frac{(p_V - p_B}{\rho_f} \right)^{1/2} \tag{34}$$

Consequently, the volume should increase as

$$\frac{V(t)}{V_O} = \left(1 + \frac{t_G^*}{R_O} \frac{r_C}{u_C} \left(\frac{2}{3} \frac{(p_V - p_B}{\rho_f} \right)^{1/2} \right)^3 \tag{35}$$

Also plotted in figure 15 is the volume growth predicted by equation 35, where $t^* = t_G^* - t_O^*$ with the offset t_O^* = 0.18 and 0.45 for σ_∞=1.0 and 2.0, respectively. These offsets are necessary to account for the time when the computed bubble begins to grow rapidly. Once the computed bubble begins to grow, the growth rate is approximately that of the asymptotic value, although the growth rate increases once the bubble is large and captured by the vortex.

8. Experimental Observation of Bubble Capture and Growth

The capture of bubbles was examined experimentally for the vortex described in Section 4. The size of the bubble created varied with the laser power and the freestream cavitation number. However, it was not possible to precisely control the size of the bubble created with the

laser. **Figure 16a** and **16b** shows 8 images of a laser-induced bubble as it is captured by the vortex for σ_c = 3.0. The vortex centerline and core radius are marked, and the time duration between the images is 350 microseconds. The capture time as measured for multiple bubbles, and the results are shown in **Figure 17.** The estimated uncertainty in the capture time is **+/- 6%.** The experimentally determined capture times fall within the computed capture times given the variability of the initial bubble size. The bubbles under consideration can be considered cavitating nuclei, as their volume does grow as they enter the low-pressure region near the core. However, as discussed above, the non-cavitating PTM predicts the capture time with reasonable accuracy.

9. Conclusions

The particle-tracking model can successfully predict the capture time for small bubbles by a line vortex. For the small bubbles starting far from the vortex, variation in capture time with differing choices of the lift coefficient are relatively small. The accuracy of the PTM is reduced as the bubble moves to within the core radius, and the DNS solutions suggest that the PTM will under-predict the capture time in the final stages of collapse. The effect of bubble deformation and bubble vortex interactions will be important only at the final stages of bubble capture. The PTM will provide a usefully accurate estimate of the capture time using standard relationships for lift and drag on the spherical bubble, especially for the cases when the bubble starts far from the vortex axis. The non-cavitating PTM can be used when considering the capture of cavitation nuclei. The bubble volume changes very slowly until the final stages of bubble capture. Consequently, it is useful to separate the process into the non-cavitating capture of the nucleus and then the growth of the nucleus in the low-pressure core region. The growth of the nucleus

prior to cavitation inception is relatively small, but such bubble growth will lead to a somewhat faster capture as the bubble comes near the core.

10. Acknowledgements

This work was supported by the Office of Naval Research under contract N00014-99-1-0307 with Dr. Ki-Han Kim, technical monitor. The DNS computations were conducted with the computational resources of the Maui High Performance Computing Center.

11. References

Arndt, R. E. A., 2002, "Cavitation in Vortical Flows," *Ann. Rev. of Fluid Mech.*, **34**, 143-175

Auton, T.R., 1987, "The lift on a spherical body in a rotational flow," *J. Fluid Mech.*, **183**, 199-218.

Auton T.R., Hunt, J.C.R., and Prud'homme, M., 1988, "The force exerted on a body moving in an inviscid unsteady non-uniform rotational flow," *J. Fluid Mech.*, **183**, 241-257

Boulon,O., Callenaere, M., Franc, J.-P. , and Michel, J.-M. 1999, "An experimental insight into the effect of confinement on tip vortex cavitation of an elliptical hydrofoil," *J. Fluid Mech.*, **390**, 1- 24.

Brennen, C.E., 1995, Cavitation and bubble dynamics, Oxford University Press

Chahine, G.L, 1990, "Nonspherical bubble dynamics in a line vortex," *Proceedings of the ASME FED Cavition and multiphase flow forum,* Toronto, Furuya O. (ed), Kluwer Academic Publishers, **98,** 121-126.

Chahine, G.L, 1994, "Strong interactions bubble/bubble and bubble/flow," *Bubble Dynamics and Interface Phenomena,* J.R. Blake et al. (eds), 195-206.

Chahine, G. L. and C.-T. Hsiao, 2002, "Prediction of Vortex Cavitation Inception Using Coupled Spherical and Non-Spherical Models," Proc. 24th Symp. of Naval Hydrodynamics, Fukuoka, Japan, July 8-13, 2002

Dandy, D.S. and Dwyer, H.A., 1990, "A Sphere in Shear Flow at Finite Reynolds Number: Effect of Shear on Particle Lift, Drag, and Heat Transfer," *J. Fluid Mech.*, **216,** pp. 381-410.

Esmaeeli, A., and Tryggvason, G., 1998, "Direct Numerical Simulations of Bubbly Flows. Part 1. Low Reynolds Number Arrays," *J. Fluid Mech.*, **377**, pp. 313-345.

Esmaeeli, A., and Tryggvason, G., 1999, "Direct Numerical Simulations of Bubbly Flows. Part 1. Moderate Reynolds Number Arrays," *J. Fluid Mech.*, **385**, 325-358.

Haberman, W.L. and Morton, R.K., 1953, "An Experimental Investigation of the Drag and Shape of Air Bubbles Rising in Various Liquids," *DTMB Report No.* 802.

Hsiao, C.-T. and G.L. Chahine, 2001, "Numerical Simulation of Bubble Dynamics in a Vortex Flow Using Navier-Stokes Computations and Moving Chimera Grid Scheme," Proc. 4th Int. Symp. on Cavitation, California Institute of Technology, Pasedena, CA, June 20-23, 2001

Hsiao, C.T. and Pauley, L.L., 1997, "Numerical Study of the Tip Vortex Cavitation Interception using a Bubble Dynamics Model," *Proceedings of the ASME Meeting,* Paper FEDSM 97-3258.

Johnson, V.E. and Hsieh, T., 1966, "The Influence of the Trajectories of Gas Nuclei on Cavitation Inception," *Proc. of the Sixth Symp. on Naval Hydrodynamics*, 163-179.

Magnaudet, J. and Eames, I. 2000. "The Motion of High-Reynolds Number Bubbles in Inhomogeneous Flows", *Ann. Rev. Fluid Mech.*, **32**, 659-708.

Maxey, M.R. and Riley, J.J., 1983, "Equation of Motion for a Small Rigid Sphere in a Nonuniform Flow," *Physics of Fluids*, **26**, 883-889.

Saffman P.G., 1965, "The Lift on a Small Sphere in a slow Shear Flow," *J. Fluid Mech.*, **22,** pp. 385-400.

Sridhar, G. and Katz, J., 1999, "Effect of Entrained Bubbles on the Structure of Vortex Rings," *J. Fluid Mech.*, **397**, 171-202.

Unverdi, S.O. and Tryggvason, G., 1992, "A Front-Tracking Method for Viscous, Incompressible, Multi-Fluid Flows," *J. of Computational Physics*, **100**, 23-37.

Yu, P.-W., Ceccio, S. L., and Tryggvason, G., 1995, "The Collapse of a Cavitation Bubble in Shear Flows – A Numerical Study," *Physics of Fluids*, **7,** 11, 2608-2616

Figure Captions

Figure 1: (a) Schematic diagram of the bubble-vortex interaction experiment. A single laser pulse is used to create a cavitation bubble in the bulk of the fluid. Images of the bubble are captured with a multi-exposure digital camera, and the acoustic emission of the bubble is captured with a hydrophone; (b) photograph of the hydrofoil in the water tunnel test section with developed tip-vortex cavitation with U_∞ = 10 m/s, and σ_∞ = 1.4, with flow from left to right.

Figure 2: (a) The average vector map of the flow perpendicular to the vortex axis 90 mm downstream of the tailing edge for U_∞= 10 m/s; (b) the measured tangential velocity, $u_\theta(r)$, along with the velocity distribution for the Gaussian vortex with r_C = 5.6 mm and Γ_O = 0.290 m^2/s and the resulting calculated pressure depression, $p(r) - p_\infty$.

Figure 3: Bubble capture time, t^*, versus the release position, r_X / r_C, for varying bubble sizes, r_C / R_O computed with the PTM. Also shown is the solution for the approximate capture time from equation 22.

Figure 4a: Bubble capture time, $t*$, versus the release position, r_X / r_C, for varying bubble sizes, r_C / R_O, and the lift coefficient, cl, computed with the PTM.

Figure 4b: Same as figure 4a.

Figure 5: Bubble capture time, $t*$, versus the release position, r_X / r_C, for varying Renolds number, Re, computed with the PTM.

Figure 6: (a) The DNS simulation of a non-cavitating bubble being captures by a line vortex. r_c / R_0 = 8, We = 0.13 and released at r_x / r_c = 1. (b) The DNS simulation of the vorticity contours and the streamlines at t*=0.85 with the same conditions as in figure 6a.

Figure 7: The trajectory of a non-cavitating bubble for varying the release position, r_X / r_C, computed with the PTM and DNS. The capture time criterion is $0.25 * r_C$.

Figure 8a: The trajectory of a non-cavitating bubble for varying the Weber number, We, computed with the PTM and DNS. The capture time criterion is $0.25 * r_C$.

Figure 8b: Same as figure 8a

Figure 9a: The trajectory of a non-cavitating bubble computed with the PTM and DNS. Also is shown the trajectory of a non-cavitating bubble with an increase drag coefficient by 150%, $PMT*$. The capture time criterion is $0.25 * r_C$.

Figure 9b: The trajectory of a non-cavitating bubble computed with the PTM and DNS. Also is shown the trajectory of a non-cavitating bubble with an increase drag coefficient by 200%, PMT^*. The capture time criterion is $0.25 * r_C$.

Figure 10: The quasi-static growth of the bubble radius is plotted as a function of distance from the vortex axis for a bubble with an initial size $r_c / R_0 = 50$, We = 26 for varying vortex cavitation numbers (solid lines). Also plotted is the solution of equation 33, which yields the critical radius for rapid bubble growth as a function of r_x / r_c for varying cavitation numbers. The vertical dotted lines occur when $p(r) = p_v$ for a given σ_∞. The pressure field is that of the experimental vortex.

Figure 11: Same as Figure 10 but with $r_c / R_0 = 200$, We = 6.5.

Figure 12: Same as Figure 10 but with $r_c / R_0 = 500$, We = 2.6.

Figure 13: Same as Figure 10 but with $r_c / R_0 = 1000$, We = 1.3.

Figure 14: The DNS simulation of a cavitating bubble being captures by a line vortex. $r_c / R_0 =$ 8, We = 24, $\sigma_\infty = 1.0$. The bubble was initially in equilibrium and released at $r_x / r_c = 1$.

Figure 15: The rate of volume growth for cavitating bubbles captured by a line vortex from the DNS simulation for varying We and σ_∞. $r_c / R_0 = 4$, and the bubble is initially in equilibrium and released at $r_x / r_c = 1$. Also plotted is the offset asymptotic volume growth of a cavitating spherical bubble given by equation 35.

Figure 16a: 8 images of a laser-induced bubble as it is captured by the vortex for cavitation number, σ_∞=3.0. The release position of the bubble, r_x / r_c=1. The delay between each image is 350 microseconds. The capture time, t^*=1.25. The bubble size, r_c / R_0=6.

Figure 16a: Same as Figure 16a but with. The capture time, t^*=0.9. The bubble size, r_c / R_0=10.

Figure 17: Bubble capture time, t^*, versus the release position, r_X / r_C, for varying bubble sizes, r_C / R_O, and the lift coefficient, cl, computed with the PTM. Also shown is the experimental data for varying the release position, r_X / r_C.

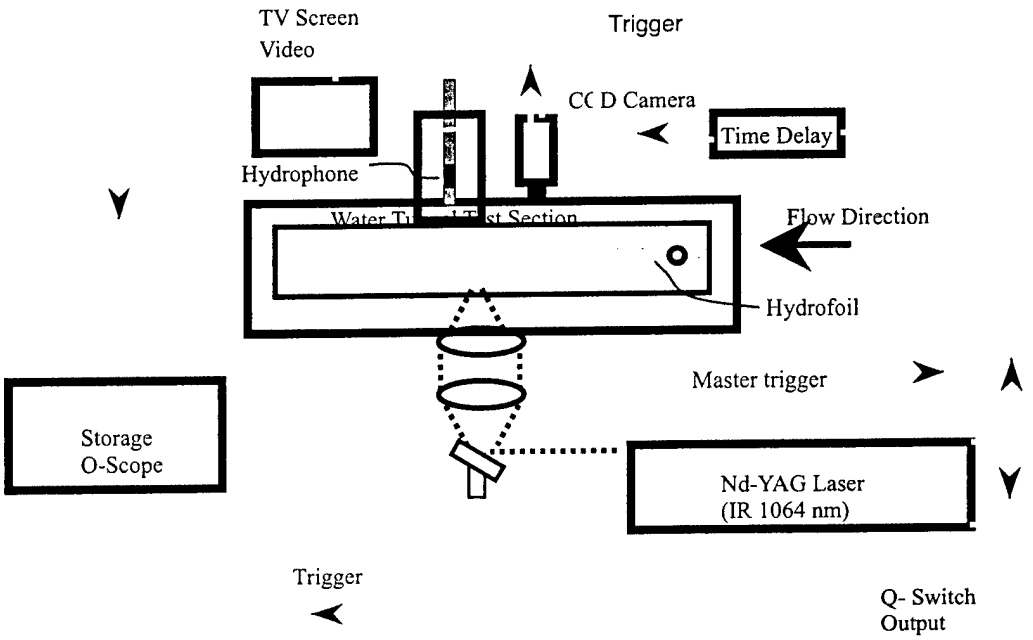

(a)

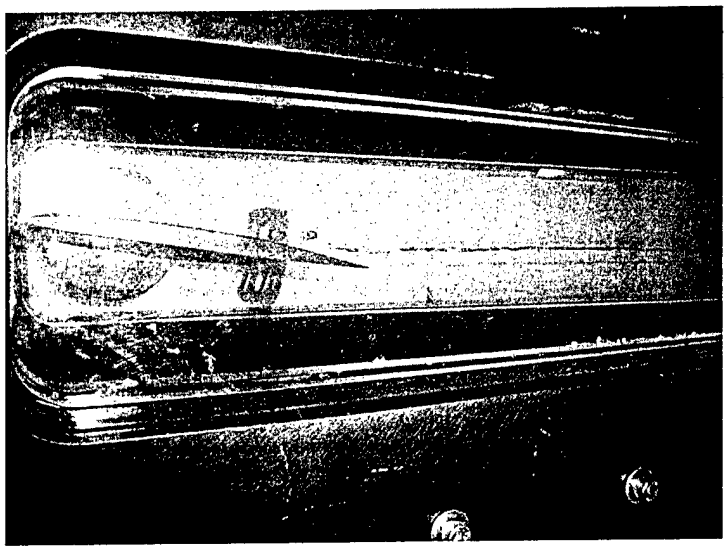

Figure 1: (a) Schematic diagram of the bubble-vortex interaction experiment. A single laser pulse is used to create a cavitation bubble in the bulk of the fluid. Images of the bubble are captured with a multi-exposure digital camera, and the acoustic emission of the bubble is captured with a hydrophone; (b) photograph of the hydrofoil in the water tunnel test section with developed tip-vortex cavitation with U_∞ = 10 m/s, and σ_∞ = 1.4, with flow from left to right.

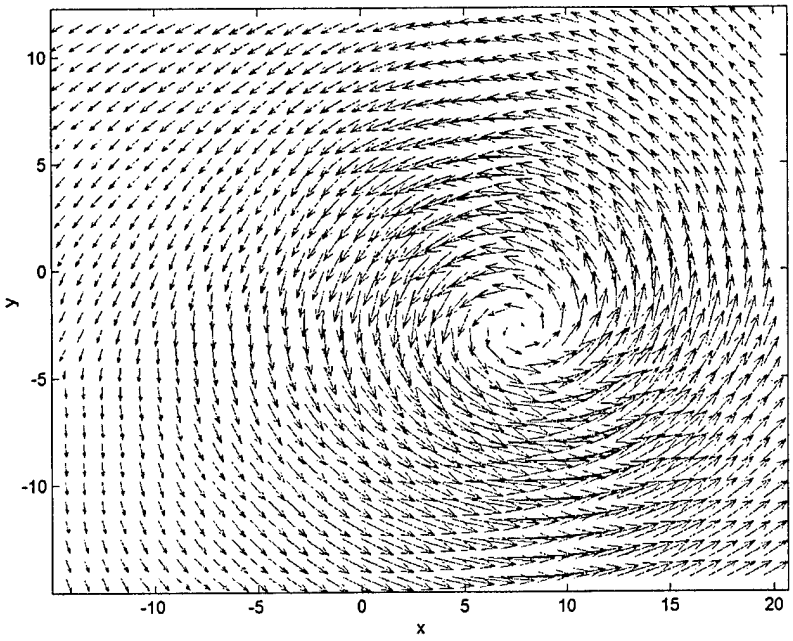

(a)

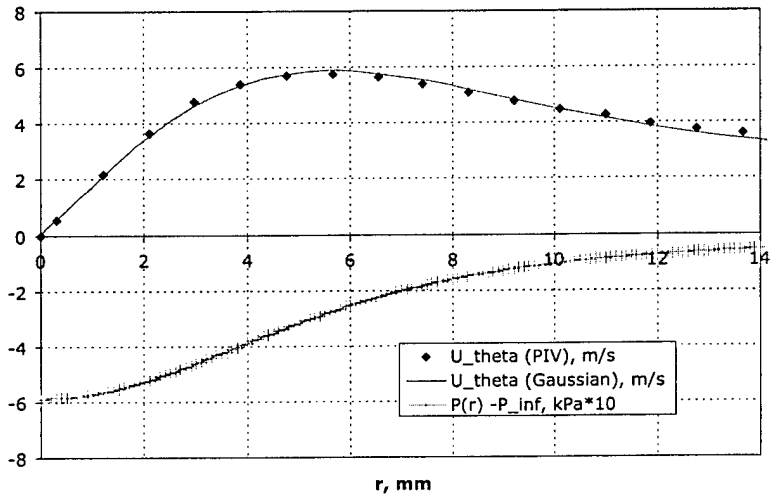

(b)

Figure 2: (a) The average vector map of the flow perpendicular to the vortex axis 90 mm downstream of the tailing edge for U_∞= 10 m/s; (b) the measured tangential velocity, $u_\theta(r)$, along with the velocity distribution for the Gaussian vortex with r_C = 5.6 mm and Γ_O = 0.290 m^2/s and the resulting calculated pressure depression, $p(r) - p_\infty$.

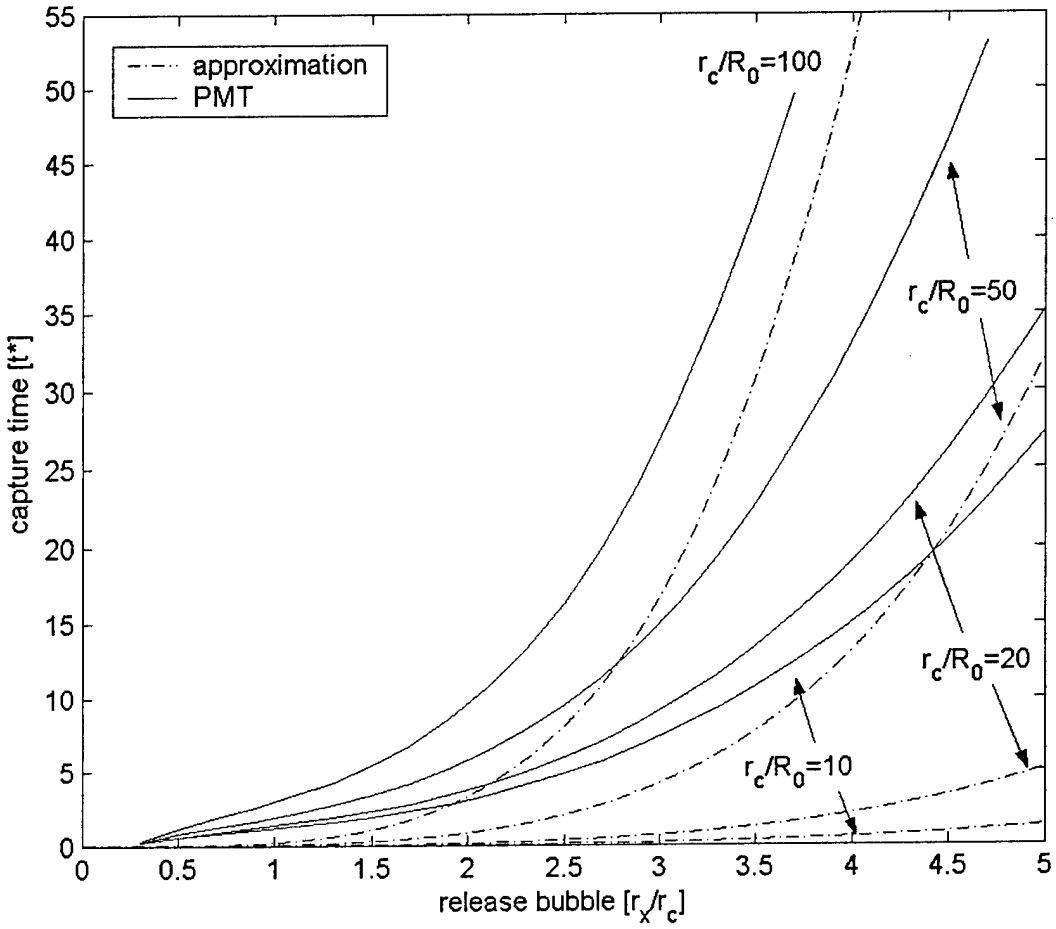

Figure 3: Bubble capture time, t^*, versus the release position, r_X / r_C, for varying bubble sizes, r_C / R_O computed with the PTM. Also shown is the solution for the approximate capture time from equation 22.

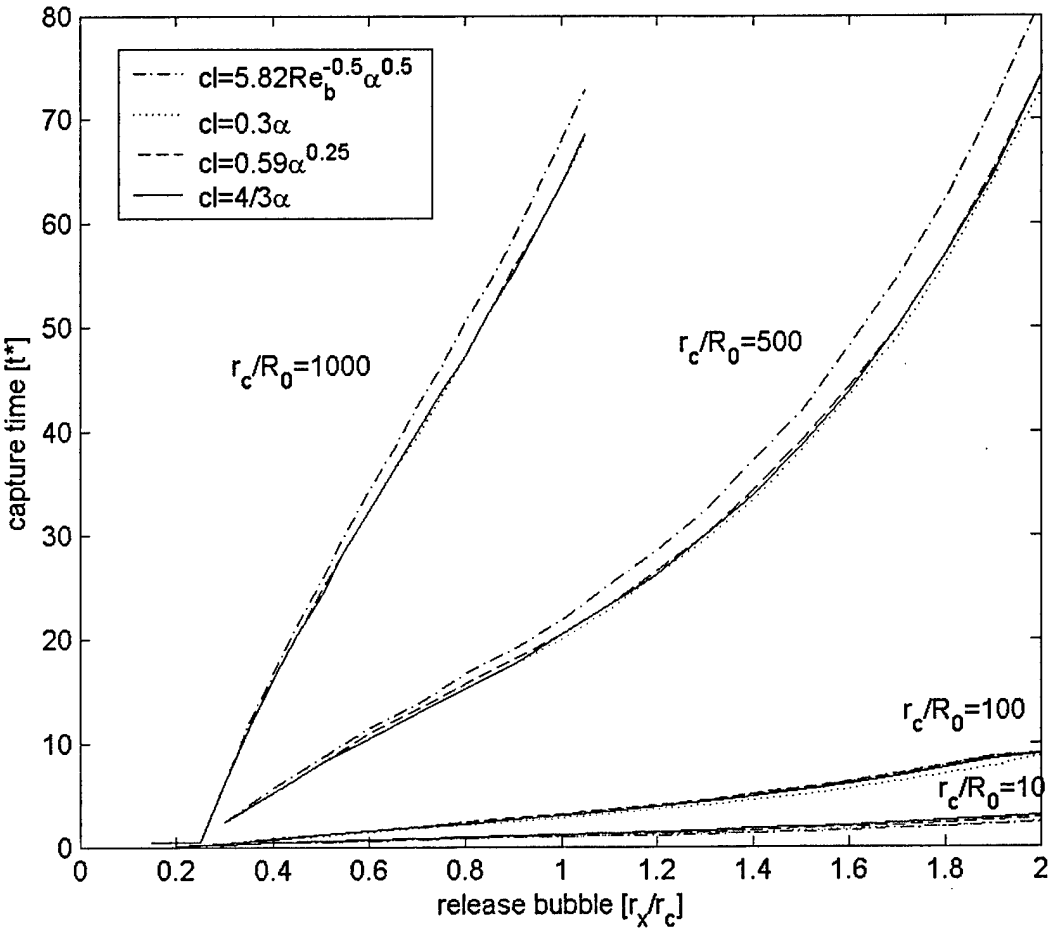

Figure 4a: Bubble capture time, t^*, versus the release position, r_X / r_C, for varying bubble sizes, r_C / R_O, and the lift coefficient, cl, computed with the PTM.

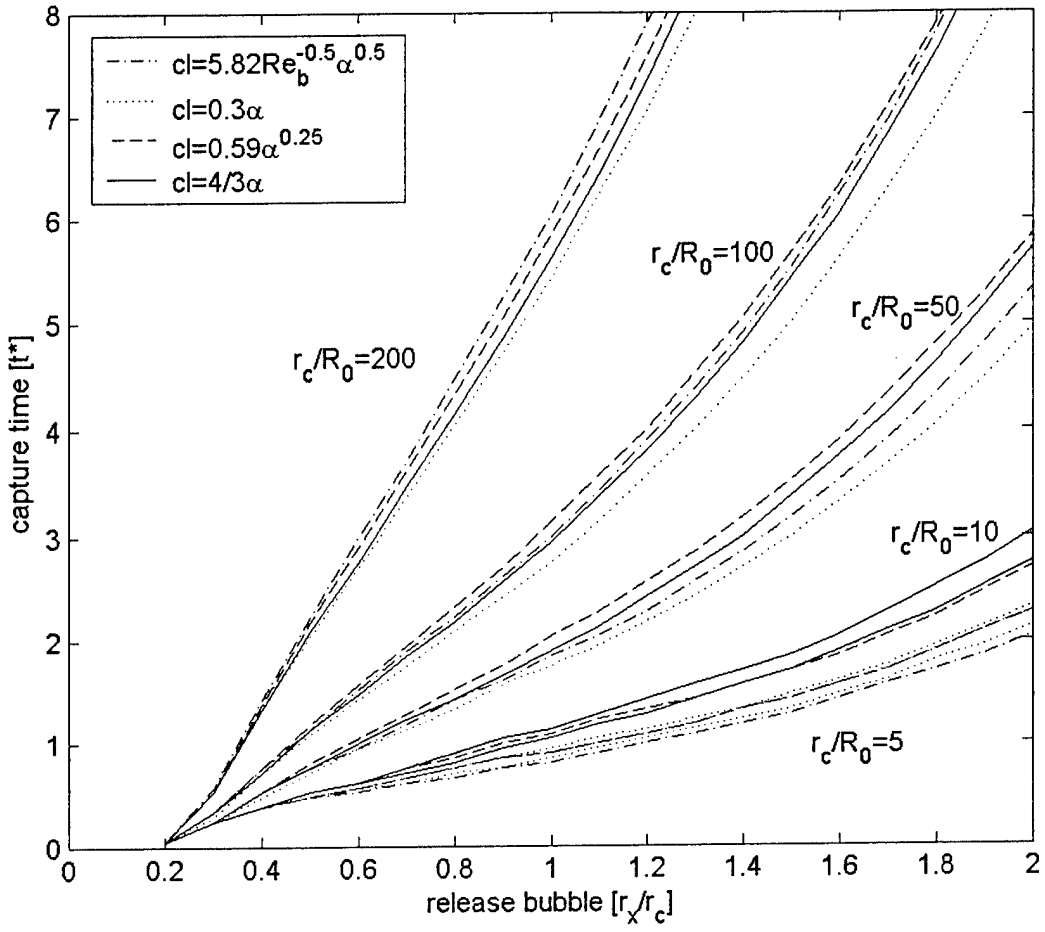

Figure 4b: Same as figure 4a.

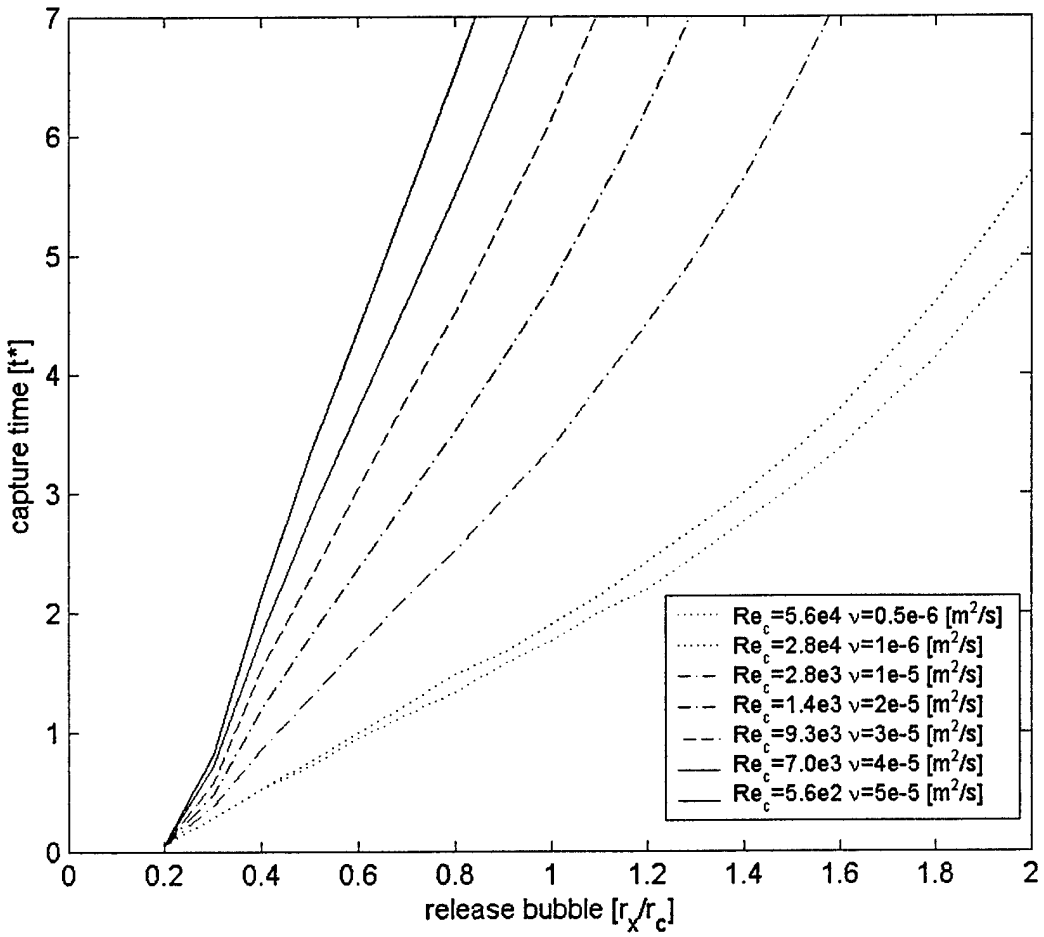

Figure 5: Bubble capture time, t^*, versus the release position, r_X / r_C, for varying Renolds number, Re, computed with the PTM.

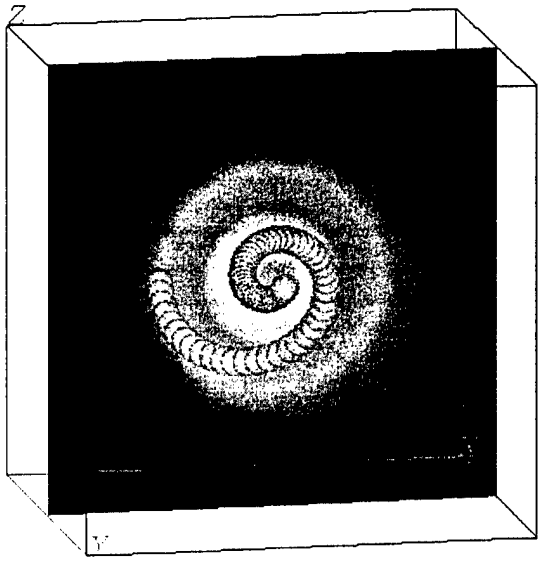

(a)

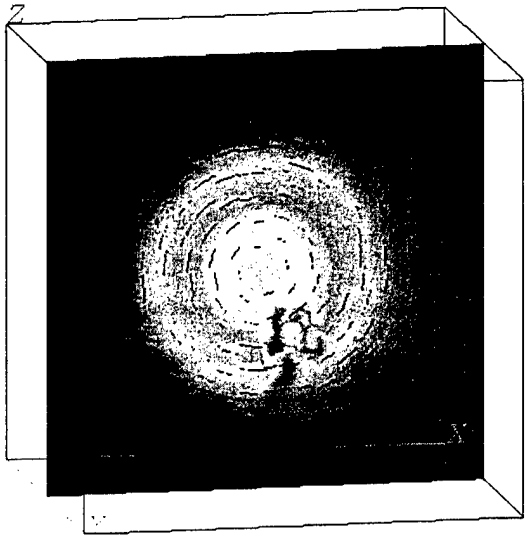

(b)

Figure 6: (a) The DNS simulation of a non-cavitating bubble being captures by a line vortex. $r_c / R_0 = 8$, We = 0.13 and released at $r_x / r_c = 1$. (b) The DNS simulation of the vorticity contours and the streamlines at t*=0.85 with the same conditions as in figure 6a.

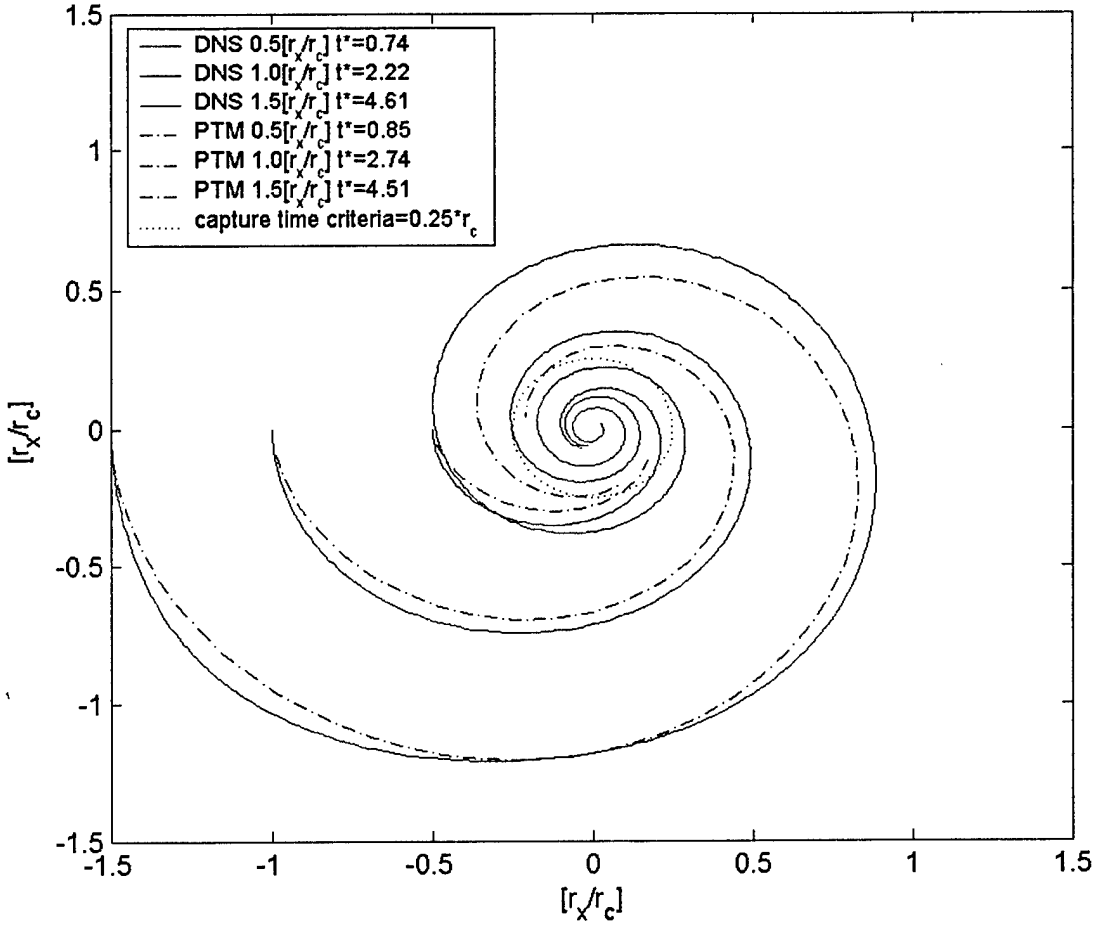

Figure 7: The trajectory of a non-cavitating bubble for varying the release position, r_X / r_C, computed with the PTM and DNS. The capture time criterion is $0.25 * r_C$.

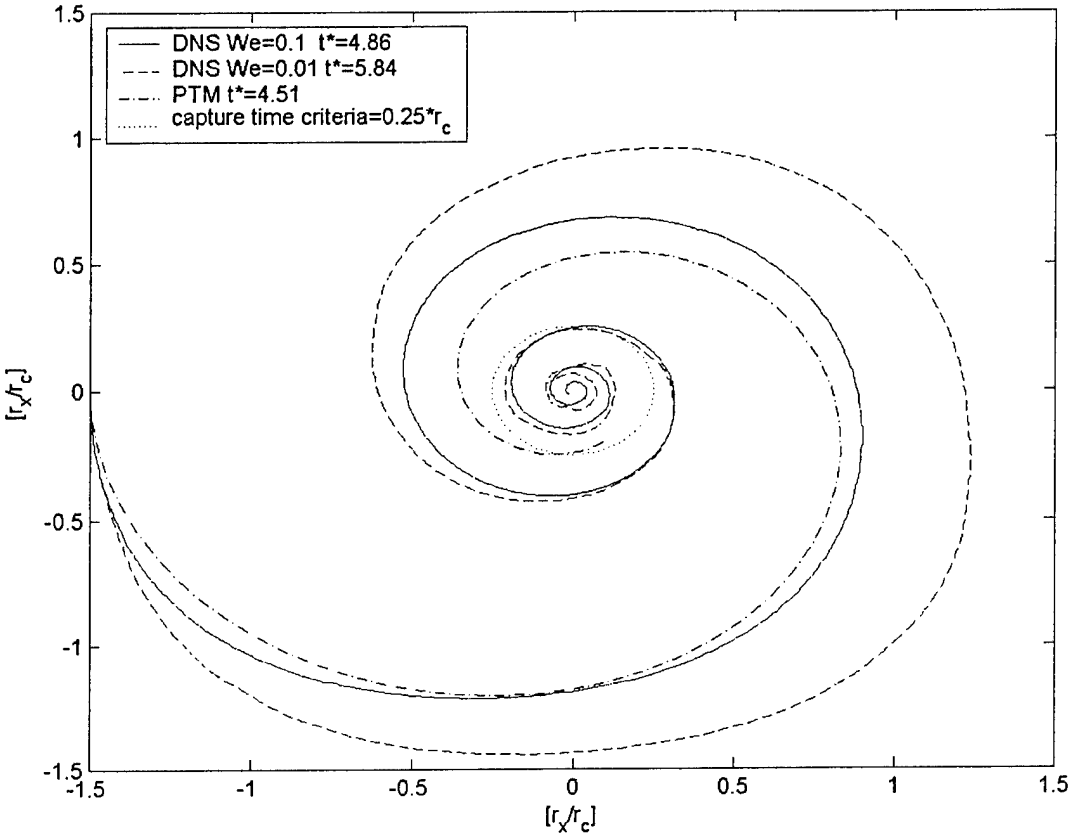

Figure 8a: The trajectory of a non-cavitating bubble for varying the Weber number, We, computed with the PTM and DNS. The capture time criterion is $0.25 * r_C$.

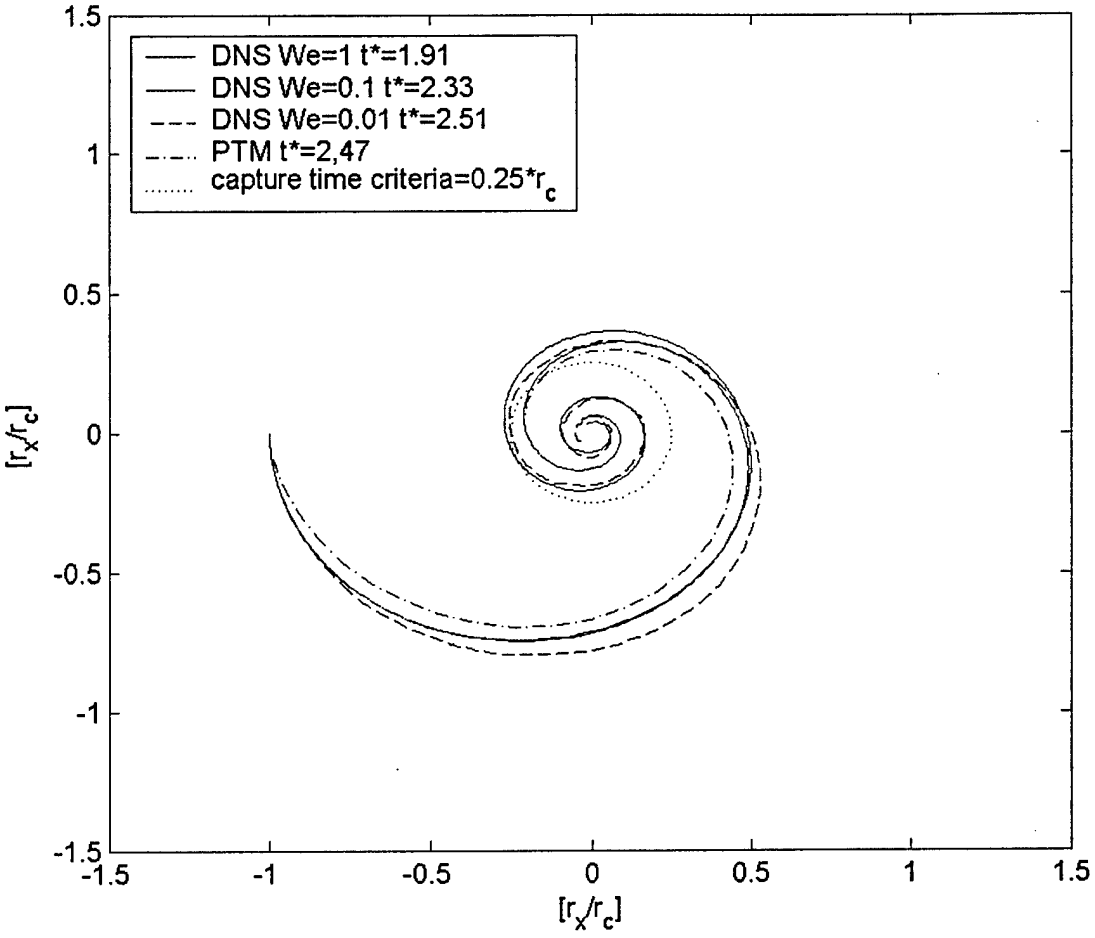

Figure 8b: Same as figure 8a

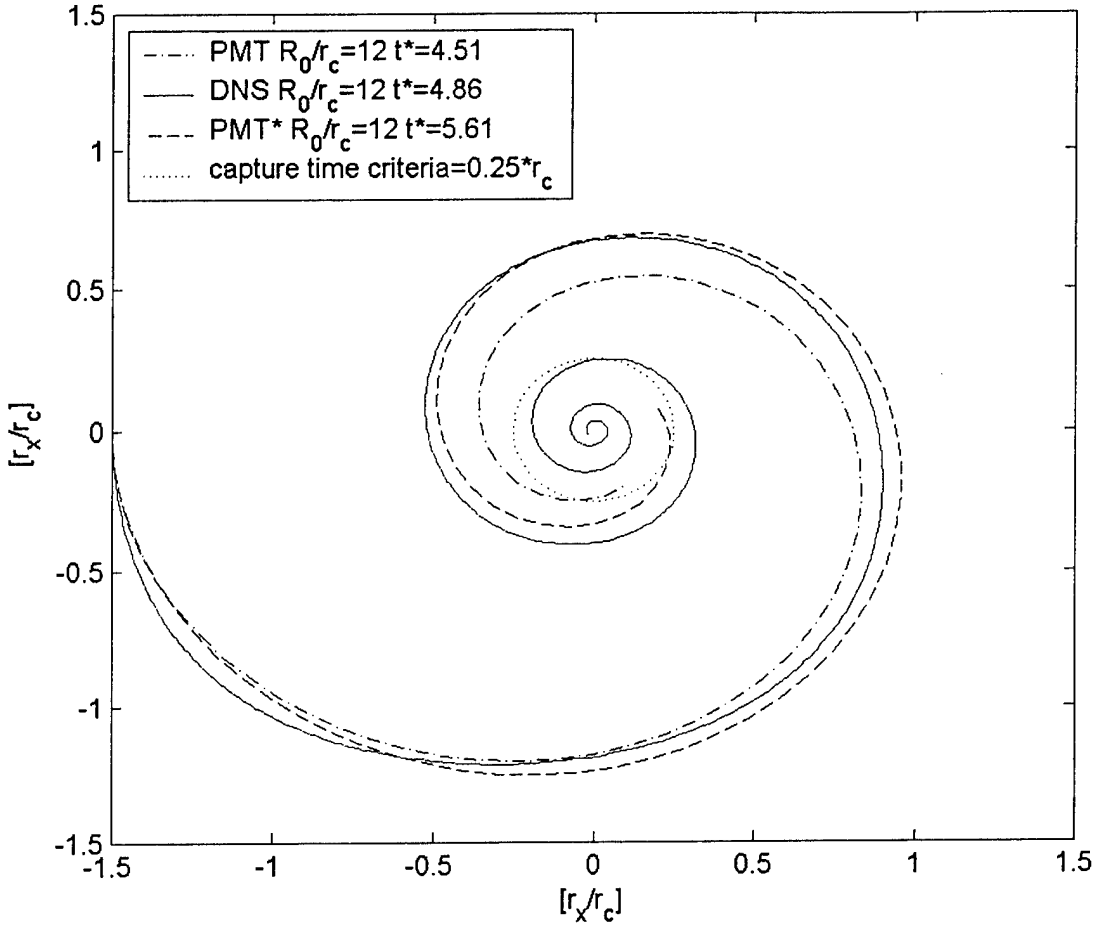

Figure 9a: The trajectory of a non-cavitating bubble computed with the PTM and DNS. Also is shown the trajectory of a non-cavitating bubble with an increase drag coefficient by 150%, $PMT*$. The capture time criterion is $0.25*r_c$.

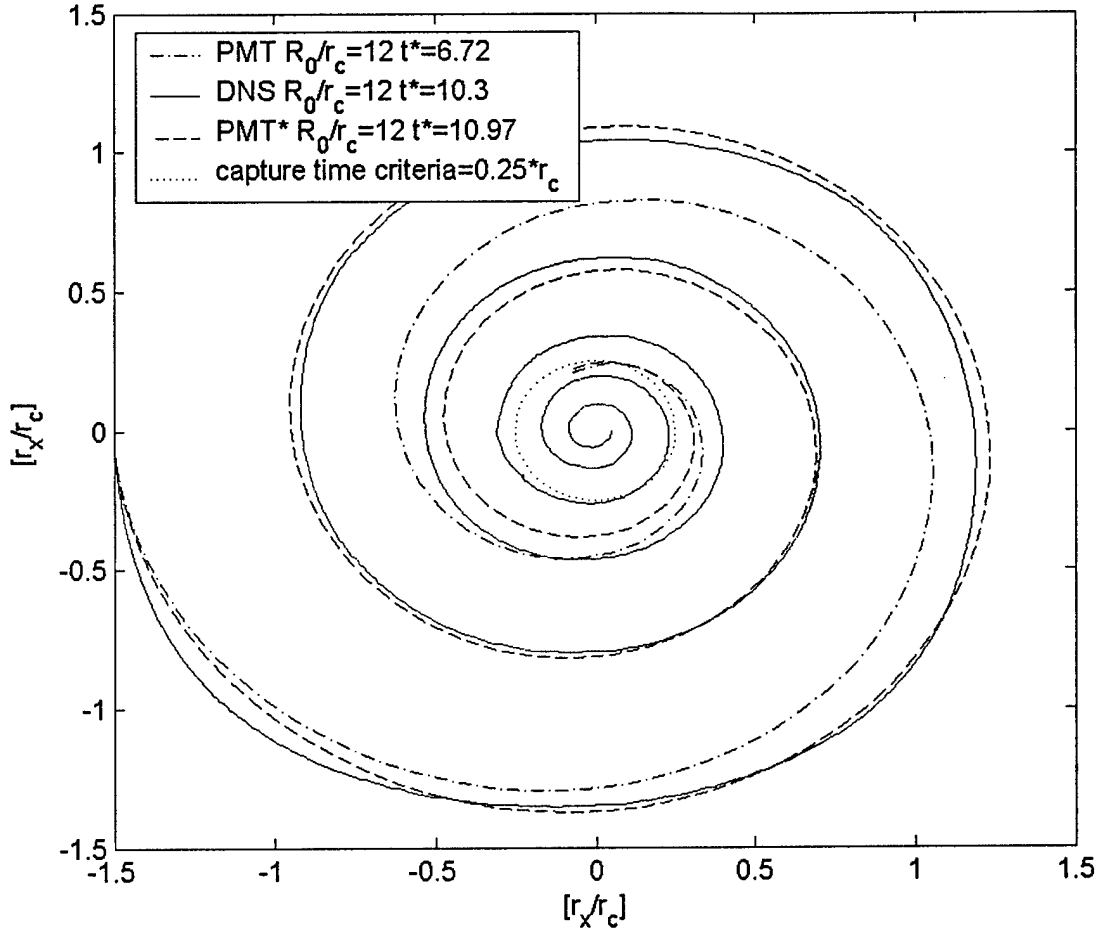

Figure 9b: The trajectory of a non-cavitating bubble computed with the PTM and DNS. Also is shown the trajectory of a non-cavitating bubble with an increase drag coefficient by 200%, $PMT*$. The capture time criterion is $0.25 * r_C$.

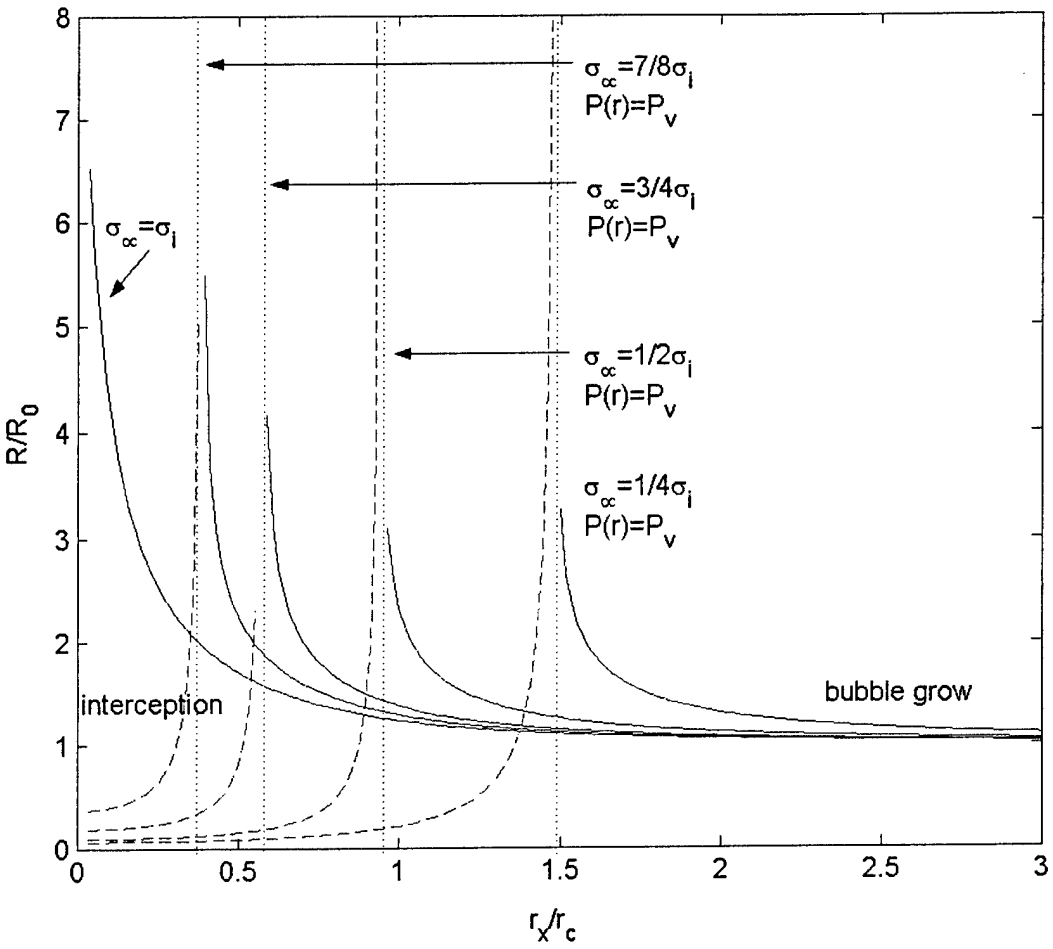

Figure 10: The quasi-static growth of the bubble radius is plotted as a function of distance from the vortex axis for a bubble with an initial size $r_c / R_0 = 50$, We = 26 for varying vortex cavitation numbers (solid lines). Also plotted is the solution of equation 33, which yields the critical radius for rapid bubble growth as a function of r_x / r_c for varying cavitation numbers. The vertical dotted lines occur when $p(r) = p_v$ for a given σ_∞. The pressure field is that of the experimental vortex.

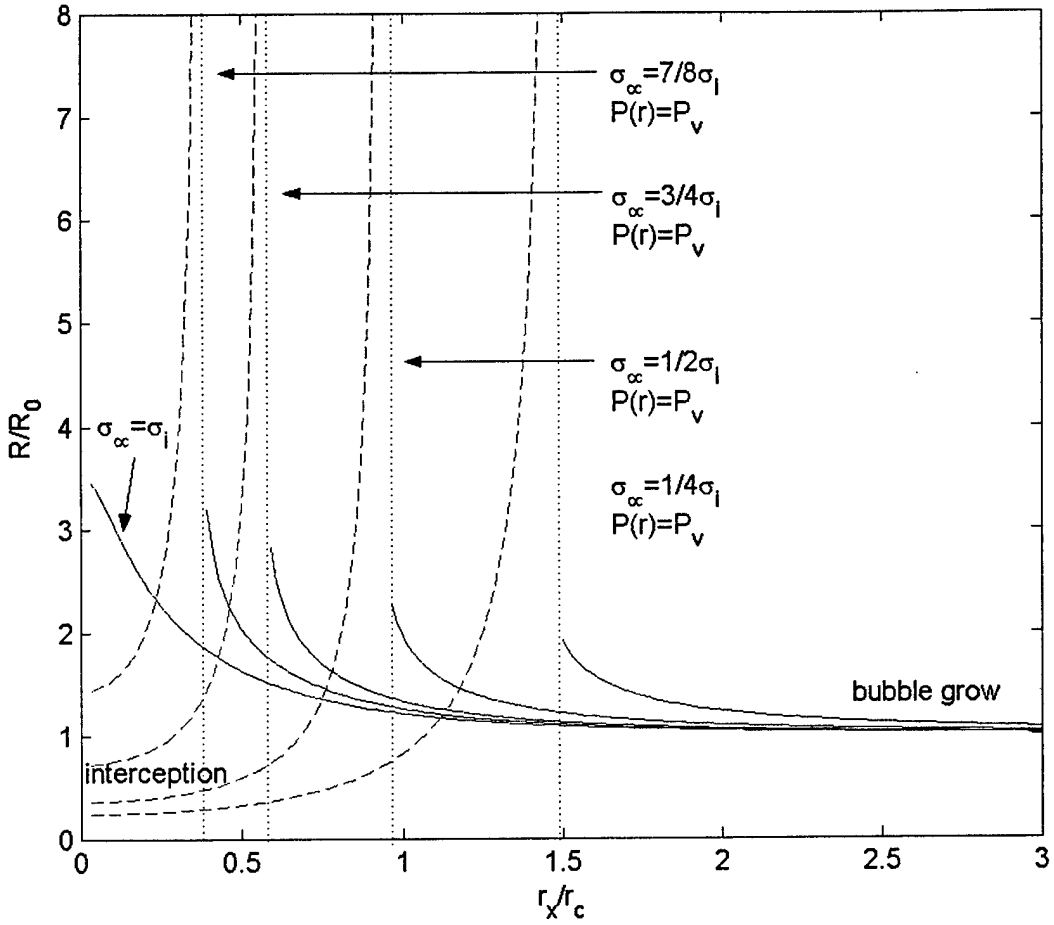

Figure 11: Same as Figure 10 but with $r_c / R_0 = 200$, We = 6.5.

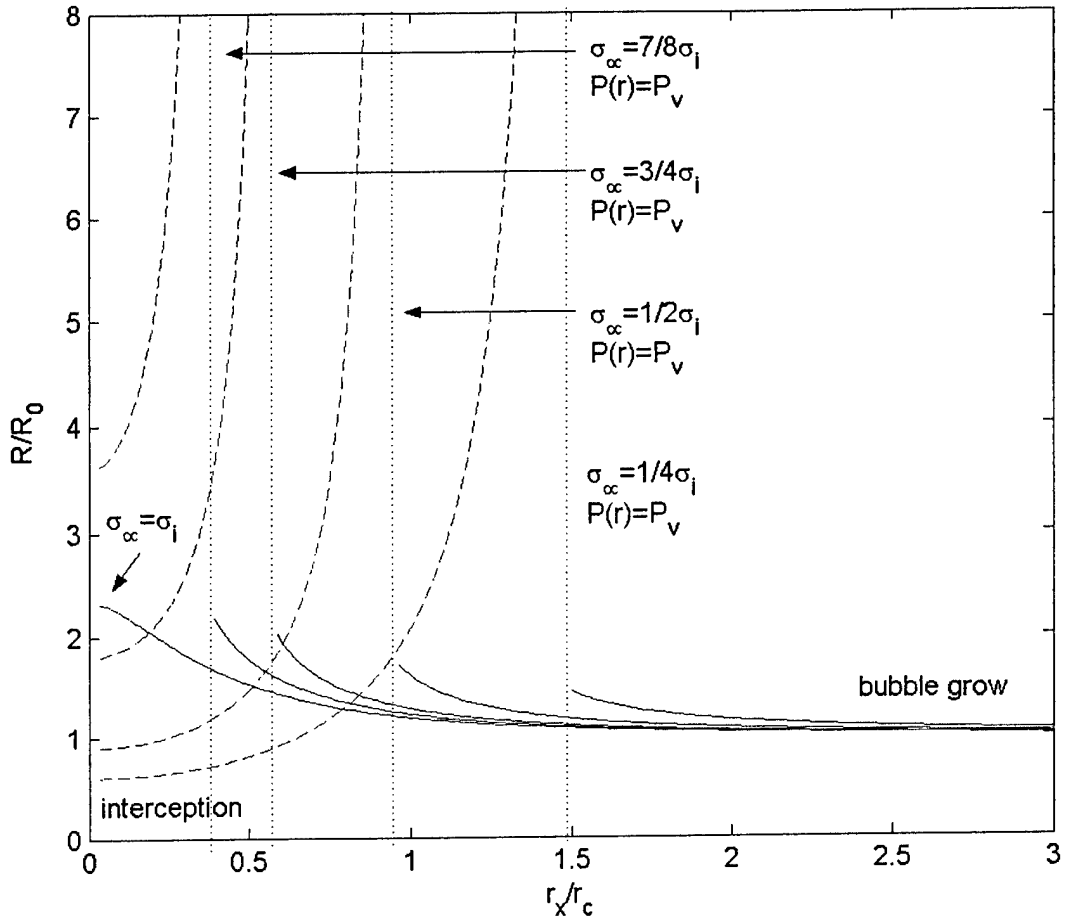

Figure 12: Same as Figure 10 but with $r_c / R_0 = 500$, We = 2.6.

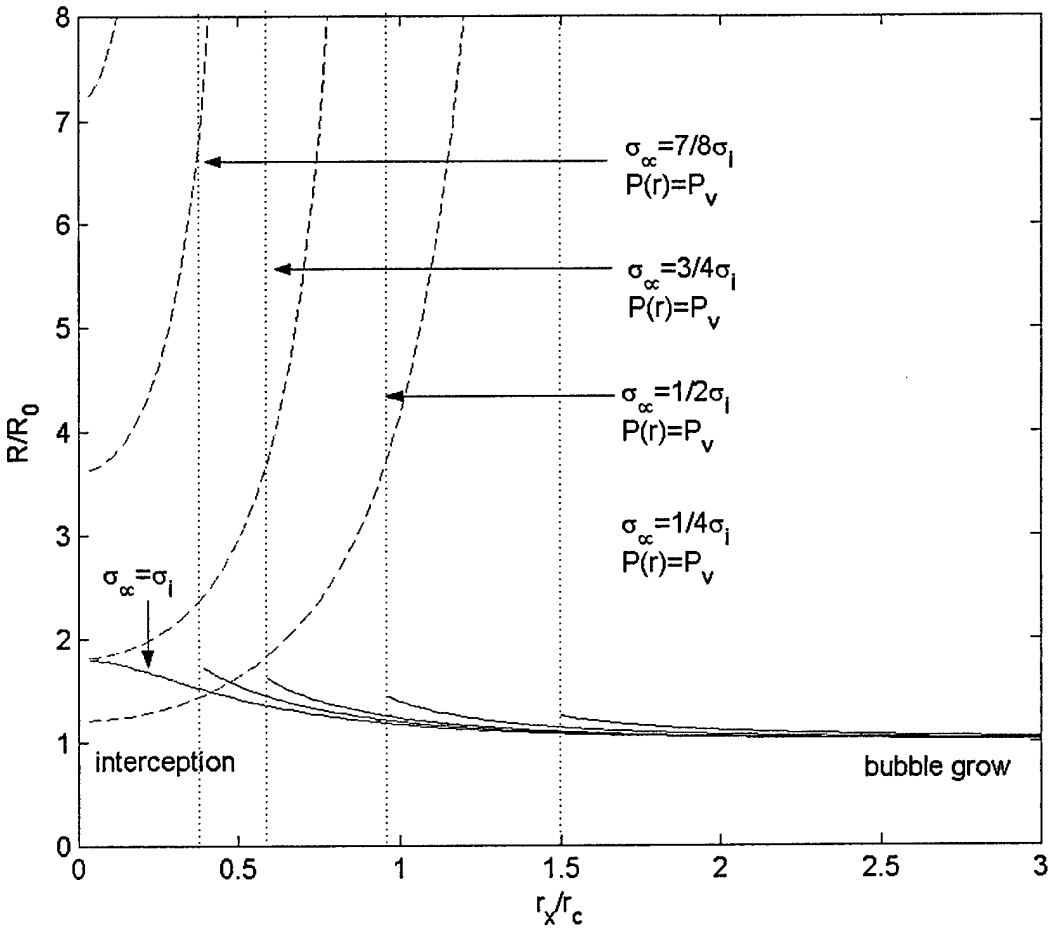

Figure 13: Same as Figure 10 but with $r_c / R_0 = 1000$, We = 1.3.

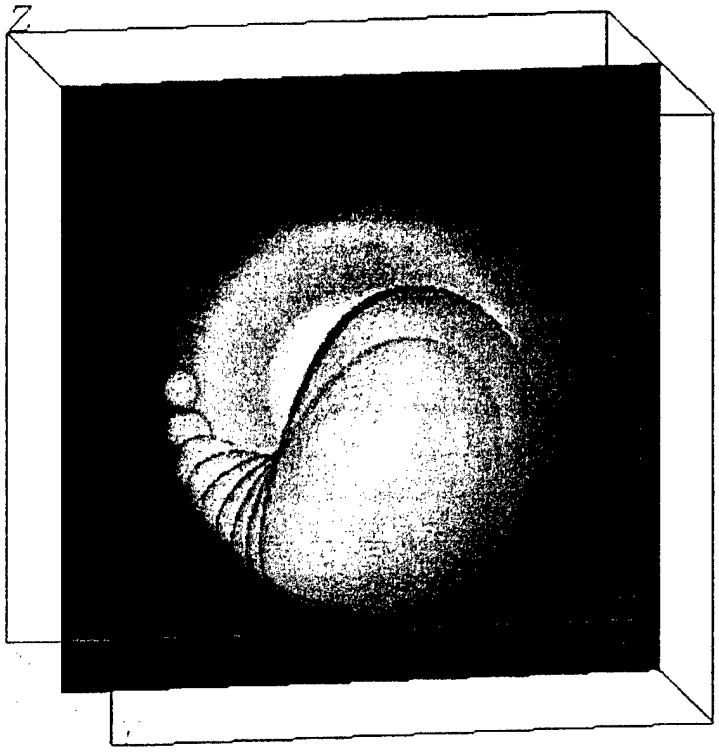

Figure 14: The DNS simulation of a cavitating bubble being captures by a line vortex. $r_c / R_0 =$ 8, We = 24, $\sigma_\infty = 1.0$. The bubble was initially in equilibrium and released at $r_x / r_c = 1$.

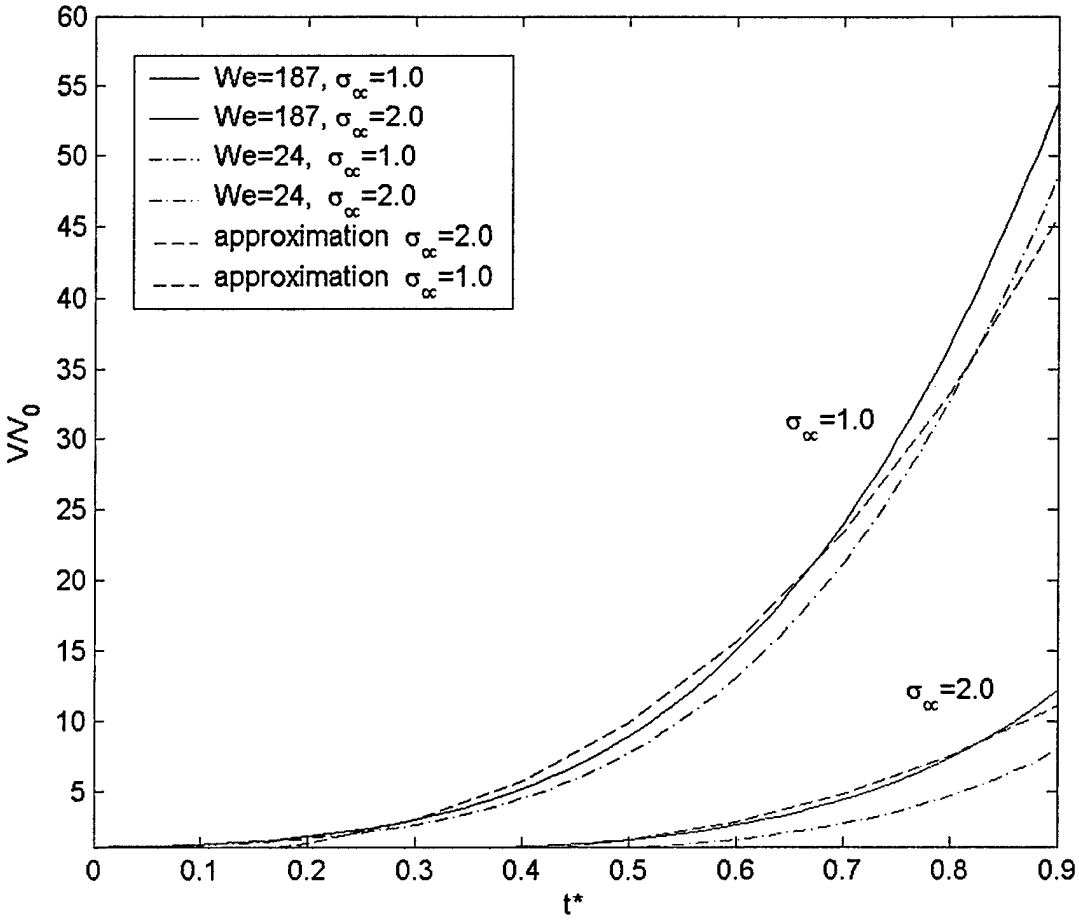

Figure 15: The rate of volume growth for cavitating bubbles captured by a line vortex from the DNS simulation for varying We and σ_∞. $r_c / R_0 = 4$, and the bubble is initially in equilibrium and released at $r_x / r_c = 1$. Also plotted is the offset asymptotic volume growth of a cavitating spherical bubble given by equation 35.

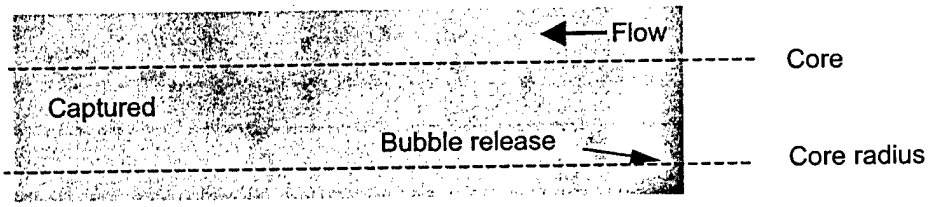

Figure 16a: 8 images of a laser-induced bubble as it is captured by the vortex for cavitation number, σ_c=3.0. The release position of the bubble, r_x / r_c=1. The delay between each image is 350 microseconds. The capture time, t^*=1.25. The bubble size, r_c / R_0=6.

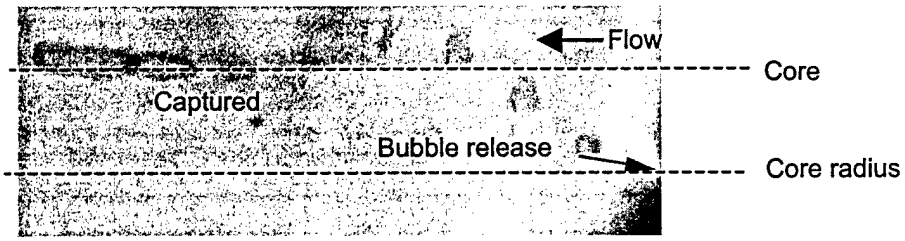

Figure 16b: Same as Figure 16a but with. The capture time, t^*=0.9. The bubble size, r_c / R_0=10.

.

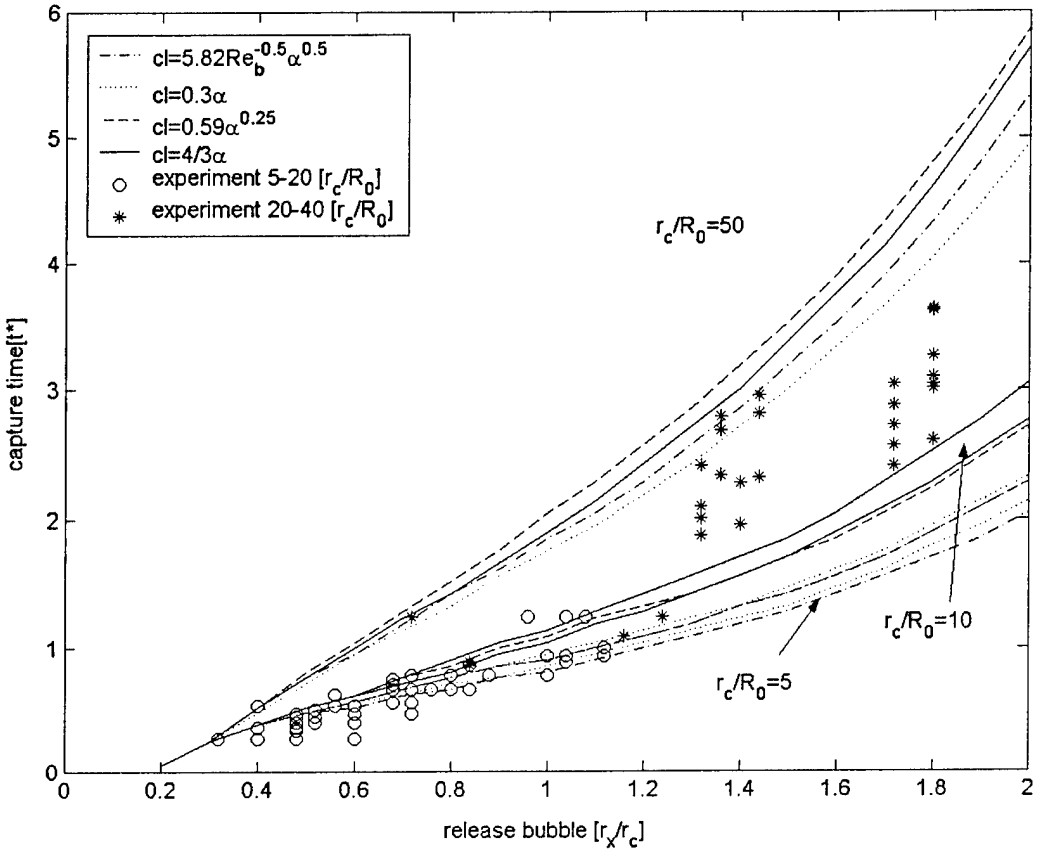

Figure 17: Bubble capture time, t^*, versus the release position, r_X / r_C, for varying bubble sizes, r_C / R_O, and the lift coefficient, cl, computed with the PTM. Also shown is the experimental data for varying the release position, r_X / r_C.